Durham E-Theses

Imaging polarimetry of pre- and post- main sequence objects

Rolph, C.D.

Imaging Polarimetry of Pre- and Post-Main Sequence Objects.

C.D.Rolph B.Sc.

A thesis submitted to the University of Durham
for the degree of Doctor of Philosophy.

Department of Physics

September 1990.

Abstract

In the first part of this thesis an automated polarimeter is described, and details are given of a dedicated CCD camera system based on a personal computer. The quality of the data produced by these instruments is demonstrated by the results presented in the succeeding chapters.

Polarimetric observations of nebulae associated with two pre-MS objects, HH83/Re17 and GL2591, and two post-MS objects, IRAS 07131-0147 and OH 231.8+4.2, are presented and discussed with reference to previous observations. In each case the location of the exciting source is determined and a simple model is described which explains the observed characteristics of the system.

Both HH83/Re17 and GL2591 are shown to be illuminated by nearby IRAS sources which have no optical counterparts. The nebula associated with HH83/Re17 is caused by the reflection of radiation off the insides of the walls of a cavity excavated in the dark cloud by outflows from the IRS, and is crossed by a narrow unpolarised jet seen in emission-line radiation. The nebula associated with GL2591 is illuminated at optical wavelengths by both the IRS and a second, visible, source, and is composed of material ejected by the IRS in a discrete period of mass loss.

IRAS 07131-0147 and OH 231.8+4.2 are shown to be stars which have evolved off the AGB and which will soon become the central stars of planetary nebulae. The protoplanetary nebulae which have formed as a result of the action of the fast stellar wind on the extended RGE around each star are bipolar and axially symmetric. The fast wind is shown to have ceased in the case of IRAS 07131-0147, but that related to OH 231.8+4.2 is still carrying material away from the star in a highly collimated fashion, producing narrow dusty filaments along the axes of the cavities. High levels of polarisation are measured in both nebulae, which indicates that the scattering particles are much smaller than those in the ISM.

A brief comparison of the pre- and post-MS nebulae shows that the two phases of stellar evolution are linked by a number of observationally similar characteristics, and it is thought that similar processes may occur at opposite ends of the evolutionary track. Most notably, circumstellar discs appear to be common at various stages in the stellar life-cycle.

Contents

List of Figures

Preface

The contents of this thesis describe some of the work carried out by the author between 1987 and 1990, under the supervision of Dr. S.M. Scarrott. Although the author was not involved in the design and development of the automated polarimeter it was felt necessary to include a thorough description of it here since it has not been documented elsewhere, and also because it is complementary to the chapter on the CCD camera system with which the author was concerned, giving a more complete picture of the instrumental setup.

The remainder of the work presented here is wholly that of the author, who was present when all the observations were made. Some of the results of chapters 3, 5 and 6 have been published in papers listed in appendix B, but in all cases the data have been re-analysed by the author for this work.

None of the material contained within this thesis has been previously submitted for a degree in this or any other university.

Chapter 1

The automated polarimeter

The Durham Imaging Polarimeter was designed to measure the optical linear polarisation of extended astronomical objects. This chapter gives an account of the automated polarimeter, the latest model of the instrument which is currently being used by the Durham polarimetry group. Included are details of its mechanical construction, an outline of the procedures involved in its operation, and a brief description of the software used to control the instrument. Although the principles of the optical design have been described elsewhere they are summarised here for completeness.

1.1   Historical background

The original design of the Durham polarimeter is well documented and is described in detail by Pallister (1976), Axon (1977), and Warren-Smith (1979). Although the philosophy that lies behind the design of the optical arrangement has changed little from that of the first prototype, which was based on work by Öhman (1939), minor changes have been made in the mechanical construction and in the type and quality of optics employed in the instrument. Scarrott *et al.* (1983) detail the construction and use of the polarimeter with an electronographic camera as the image recording device, whilst Draper (1988) describes the recent conversion to charge-coupled devices (CCDs) as imaging systems, and outlines the use of a

1

superachromatic half wave plate which allows the polarimeter to operate in the spectral range from 350 to 1000nm. The software used to reduce the polarimetric data is an extended set of the programmes developed by Dr. Rodney Warren-Smith, as described in his thesis (1979).

All previous models of the polarimeter involved an observer who would have to work in the telescope dome with the instrument, changing the half wave plate position, the filter etc., and, in the electronographic era, changing the film and operating the McMullan camera as well. With the advent of CCD camera systems as astronomical detectors, and the evidence of their quality and usefulness when used with the Durham polarimeter (Draper 1988), it became evident that the next logical step in polarimeter design would be to make the instrument remotely controlled by computer, so that the observer could work in the relative comfort of the telescope control room, operating both the polarimeter and the CCD camera system with ease from two computer keyboards. This step has recently been made, and the observer now has control over five polarimeter functions which will be described fully in turn. These are all based on the same principle; a stepper motor moves a component via a system of bevel gears or worms, and the position is sensed using a pair of slotted infrared optoswitches.

1.2   Optical design philosophy

The Durham polarimeter is an imaging device which employs a Wollaston prism to split the incident beam of light into two orthogonally polarised beams diverging at a nominal angle of 1°. Thus two images of any field are produced on the detector for each integration. Because of the small divergence of the prism the pair of images would normally overlap, and careful analysis would be required to separate them. The Durham polarimeter, however, has a series of occluding bars (the grid assembly) which lie in the focal plane of the telescope; these are spaced such that the pair of images produced by the prism interleave neatly on the detector with no overlaps. In this way the brightness of any point in the field can be measured

simultaneously in two orthogonal polarisation states.

In order to fully analyse the incident light polarimetrically at least one further measurement must be made at a third position angle; this could be done by rotating the prism, the whole instrument, or alternatively by rotating the plane of polarisation of the incident radiation. The Durham polarimeter adopts the third approach, using a half wave plate to rotate the plane of polarisation by 45° before it is analysed by the prism. In this way two exposures produce four intensity images, measured at position angles separated by 45°. In practice a total of four exposures are made with the half wave plate rotated by 22.5° each time. This enables any polarisation dependence of the instrument, due to differential losses in the optics or to a polarisation sensitive detector, to be removed easily, since the object is imaged twice in each of the four polarisation states. Furthermore, the images of the object fall on the same areas of the detector whenever an exposure is made, so the duplicity of the images causes any flat-fielding errors to cancel out.

This method offers the advantage that, since the field covered is relatively large (40mm square in the focal plane of the telescope), the sky is sampled at the same time as the object unless the object happens to be highly extended, filling the field of view. This is important because it allows the sky to be interpolated over the object and then subtracted, automatically taking into account any changes in its transparency or polarisation state. Conditions need not therefore be photometric when using this technique.

Figure 1.1 illustrates schematically the arrangement of the polarimeter's optical elements, and shows how two images are formed on the detector for every object in the focal plane of the telescope. Also illustrated are the five moving components which will be described in detail in section 1.4

1.3 Mechanical construction

The polarimeter is constructed within a framework of 38mm square aluminium struts which provide the rigidity required to carry the CCD in its dewar, the
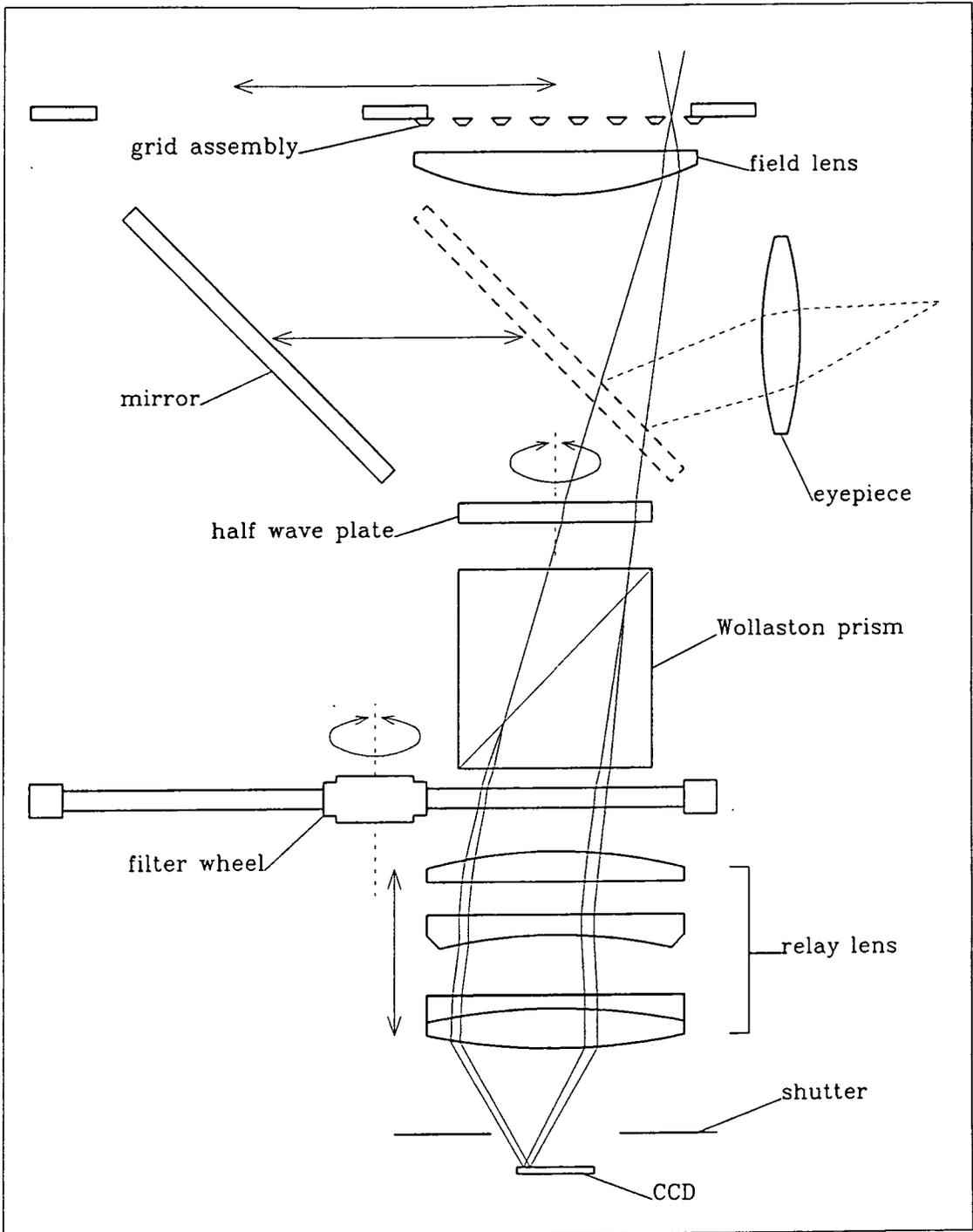
Figure 1.1: The optical layout of the polarimeter, showing the five components which can be operated remotely, and the method by which an image is split into two orthogonally polarised elements by the Wollaston prism.

polarimeter optics, and a rack of electronics on the side of the instrument without flexing. The front and back plates are of 18mm aluminium; between these and lying parallel with them are 11.5mm aluminium platforms carrying the optical components. These platforms are mounted on 16mm diameter silver steel bearings running along the length of the instrument so that they can be moved to facilitate easy access to the optics for cleaning etc. Accurately machined spacers on the bearings ensure that the platforms carrying the optical components can always be returned to the same positions. The polarimeter is enclosed by sides made of 3mm aluminium plate to provide light-tightness; one of these is hinged for access and also carries the viewing eyepiece to be used with the grid viewing mirror (section 1.4.3). All the internal components are painted matt black to minimise reflections.

The photograph in figure 1.2 shows the internal construction of the polarimeter; the platforms carrying the optical components can be clearly seen mounted on the silver steel bearings.

1.4   Optical components

1.4.1   The grid assembly

The principle of using a set of grids to mask off part of the telescope's focal plane is an important aspect of the design of the Durham polarimeter, but the details of construction of the grid assembly have changed slightly as the instrument has evolved from a simple optical bench in a wooden case to become a more complex apparatus controlled by computer. The present grid assembly is made up of six grids which are accurately machined from perspex and sprayed matt black. It has been found that the dispersion of the Wollaston prism varies slightly across the field, so to minimise the overlaps of the image pairs on the detector, and thereby maximise the efficiency of the polarimeter, the grids have been made with widths that vary accordingly from 3.35mm to 3.60mm. The widths of the seven

Figure 1.2: The Durham Imaging Polarimeter. The optical and mechanical components are closely packed inside a light-tight case; the grid assembly runs in the dovetail slot on the right of the picture, and the relay lens is to the extreme left.

rectangular apertures which the grids define increase proportionally from 3.40 to 3.80mm.

The grids rest in a carrier which is constrained to run in a dovetail groove in the inside front face of the polarimeter, such that it can be moved in a direction perpendicular to the grids themselves. The carrier is propelled along the groove by a stepper motor, via a threaded rod which is geared such that the setting accuracy is less than 0.02mm. The carrier actually has two 60mm apertures, and a range of travel of 90mm suffices to ensure that either of these can be placed concentric with the polarimeter's optical axis. The grid assembly is permanently mounted in one of these apertures, and the other aperture can be used, for example, in direct imaging, when the prism is removed and no focal plane mask is required.

Warren-Smith (1979) and Scarrott *et al.* (1983) describe how a left-right transformation is determined from pairs of images of grid spots, a set of artificial stars arranged around the edge of the field of view. The left-right transformation is applied to the left-hand image of each polarimetric data frame in order to accurately align it with its corresponding right-hand partner. The ability of the automated polarimeter to place a clear aperture in the telescope's focal plane enables the left-right transformation to be determined from real star positions, rendering the grid spots redundant, since any exposure of a rich star field will contain all the stars in the field of view, doubly imaged, with none being lost behind occluding bars. The left-right transformation of any particular star is dependent upon its position in the field, due to the dispersion of the Wollaston prism varying across the field, and it has been found that measuring the transformation of about half a dozen bright stars spread across the field of view is fully sufficient to determine a six-parameter transformation representing a shift of origin, a rotation, a magnification and a shear. It is more satisfactory to use a real star field rather than grid spots to determine the left-right transformation because the transformation can then be measured in the centre of the field where the object under investigation would be placed, and not just around the edge of the field at the grid spot positions.

The second aperture on the grid carrier can also accept a special set of grids made for a specific object. An example of this would be an object which is close to several bright stars, when a special grid assembly with only a single small rectangular aperture might be used so that the bright stars are masked off and long exposures can be made without fear of saturation. In addition a plate with an array of 0.1mm diameter holes has been made for the second aperture—uniform illumination of this plate provides a field of artificial stars which can be used for focussing the polarimeter.

Scarrott *et al.* describe how the grids are displaced laterally by one half of a grid width to expose the previously hidden part of the field and give full coverage of extended objects. Although there is no reason in principle why this could not be done with the automated polarimeter, it would in fact mean that the image would fall in a different place on the CCD, thus requiring flat fields for each grid position. Furthermore the divergence of the prism would not be optimally suited to a second grid position, so larger overlaps and gaps would be produced between the interlaced pair of images on the detector. Modern telescope technology, however, now permits most telescopes to point to great accuracy ($\sim 1''$), so, rather than moving the grid assembly, the telescope itself can be moved between each set of four exposures to obtain a complete set of polarisation measurements over an extended object. The telescope position is usually adjusted so that the image moves by two thirds of the average grid width. Thus three positions of the telescope give full coverage of any field, with overlaps of one third of a grid width between each set of four exposures, allowing them to be accurately normalised to each other.

Often it is found that there are very few stars in the same field of view as the object under investigation. If the object is sufficiently large to warrant exposures of several fields offset by 2/3 of a grid width then the number of stars common to two or more fields, which can be used to align the data, is likely to be very low. To overcome this problem the clear aperture can be used to make an exposure of the whole field which will include all the stars. This can then be used as a reference

image to which the polarimetry images can be aligned.

1.4.2 The field lens

Due to the small size of the half wave plate (25mm diameter) a lens is required between it and the grid assembly to confine the light beam so that it can pass unvignetted through the instrument. A planar convex lens with a focal length of 220mm is used for this purpose, and is mounted on a platform immediately below the grids. The lens is easily removable for cleaning; this is important because it lies very close to the telescope's focal plane and the image of any dust on it would be focussed on the detector.

1.4.3 The grid viewing mirror

A plane, front-silvered mirror was included in the original polarimeter design so that the light passing through the grid assembly could be diverted to an eyepiece mounted on the side of the polarimeter by flipping it into the light path. The automated polarimeter has a similar mirror fixed at 45° to the polarimeter axis and running on linear bearings so that it can be inserted between the field lens and the half wave plate. It is driven along a threaded bar to the required position by a stepper motor; the setting accuracy is not important but is in fact of the order of 0.1mm.

The grid viewing mirror is useful as it allows the telescope to be focussed on a bright star by means of a knife-edge test, using the edge of one of the grid bars as the knife-edge and setting the eyepiece out of focus so that it gives an image of the primary mirror. It can also be used to check that the grids are aligned with a North-South line by ensuring that a star runs up and down the edge of a grid when the telescope is nodded in declination. Although in principle the mirror and eyepiece could be used for object finding, the speed with which the CCD can be exposed and read out means that it is generally more efficient and reliable to make a test exposure than to try to spot faint nebulae by eye.

1.4.4 The half wave plate

The superachromatic half wave plate is used to rotate the plane of polarisation of the incoming light by an angle 2θ, where θ is the angle between the half wave plate's fast axis and the E-vector of the incident radiation. Rotating the half wave plate through four positions suffices to unambiguously determine the linear polarisation of the incident light and compensate for any polarisation dependence in the detector. The four positions are labelled 0, 15, 14 and 13 for historical reasons and are separated by 22.5°so that the plane of polarisation can be rotated in discrete steps of 45°. A 60:1 gear ratio between the stepper motor and the half wave plate guarantees a setting accuracy of $< 0.1°$.

In earlier models of the polarimeter the fast axis of the half wave plate was carefully aligned so that it was parallel with the grids, but Draper (1988) shows that for the superachromatic half wave plate the position angle of the axis changes with wavelength. It was therefore necessary to introduce a parameter in the reduction software which allowed for this change. This now means that the position of the axis need not be known when the half wave plate is installed in the polarimeter, but can be found later by observing calibration objects in each waveband which show good centrosymmetric polarisation patterns due to scattering from a central source.

1.4.5 The Wollaston prism

The Wollaston prism is made of a pair of optically contacted quartz wedges with mutually perpendicular optic axes. It is securely mounted in a holder close to the half wave plate such that its divergence plane is perpendicular to the grid direction.

1.4.6 The filter wheel

Between the Wollaston prism and the relay lens is a wheel that can be rotated to bring any one of eight 50mm apertures into the light path. Five of these

apertures have B, V, R, I and Z filters fitted so these can be used to define the optical bandpass of the instrument. The empty apertures can be used to make observations without a filter, in which case the bandpass is defined by the spectral response of the detector, or they can be fitted with special filters for specific objects—narrow band filters to look at an object in emission lines, for example.

The tolerance of the stepper motor driving the filter wheel allows it to be set to an accuracy of 0.1°, which is adequate since the filters are large when compared with the size of the image that is passed by the prism.

1.4.7 The relay lens

The relay lens is necessary to re-image the telescope's focal plane onto the detector. It is a 50mm f/1.2 camera lens, coated to reduce reflections and mounted on the back plate of the polarimeter. A stepper motor turns the outside of the lens housing bringing the image plane to within 0.05mm of the surface of the detector. The combination of field lens and relay lens gives a demagnification factor of 4.05 resulting in a significant decrease in the integration times required when observing extended objects, and the size of the grid assembly is such that its image fits neatly on the CCD. When the polarimeter is used on a large telescope in good seeing conditions the CCD pixel size is typically one third of the diameter of the seeing disc.

1.5 Encoders for position sensing

It has already been stated that each of the five moving optical components of the polarimeter is driven into place using a stepper motor. These motors are 4 phase, 7.5° stepper motors running with a 24 Volt power supply, which is housed with the motor control cards in an electronics rack mounted on the side of the polarimeter. The accuracy to which the components can be set is determined by the tolerance of the motors themselves, quoted as ±5%, and also by the backlash which is inevitably present in the worms and gears. Since the backlash can only be

A	B	Position
0	0	between reference positions
1	0	reference position
0	1	zero position
1	1	outside permitted range

Table 1.1: A truth table for the output of the optoswitches showing how they indicate the positions of the polarimeter's moving components.

estimated it would be unsatisfactory to infer from the number of steps moved by a motor the position of the component itself; instead a positional encoder system has been incorporated into the polarimeter design which permits the actual positions of the components to be known at all times.

The encoder system employs, for each component, a black-painted aluminium strip which passes between the LEDs and detectors of a pair of slotted infrared optoswitches. The optoswitches are fixed to the platform on which the component is mounted, whilst the aluminium strip is attached directly (i.e. with no intermediate gearing) to the component itself. This ensures that the position of the component is accurately reflected by the position of the strip with respect to the optoswitches.

The aluminium strip has a hole and a series of slots cut in it, and the optoswitches are mounted in such a way that one of them (A) can only detect the slots and the other (B) can only detect the hole. The slots mark a set of regularly spaced reference positions between the two extremes of the permitted range of travel, which are marked by the ends of the aluminium strip. The hole defines a reference position from which all other positions are measured. The arrangement of optoswitches with respect to the aluminium strip is shown in figure 1.3, and the actual mechanical construction of the half wave plate mechanism is shown in figure 1.4. The information which can be deduced from the outputs of the optoswitches is summarised in table 1.1.
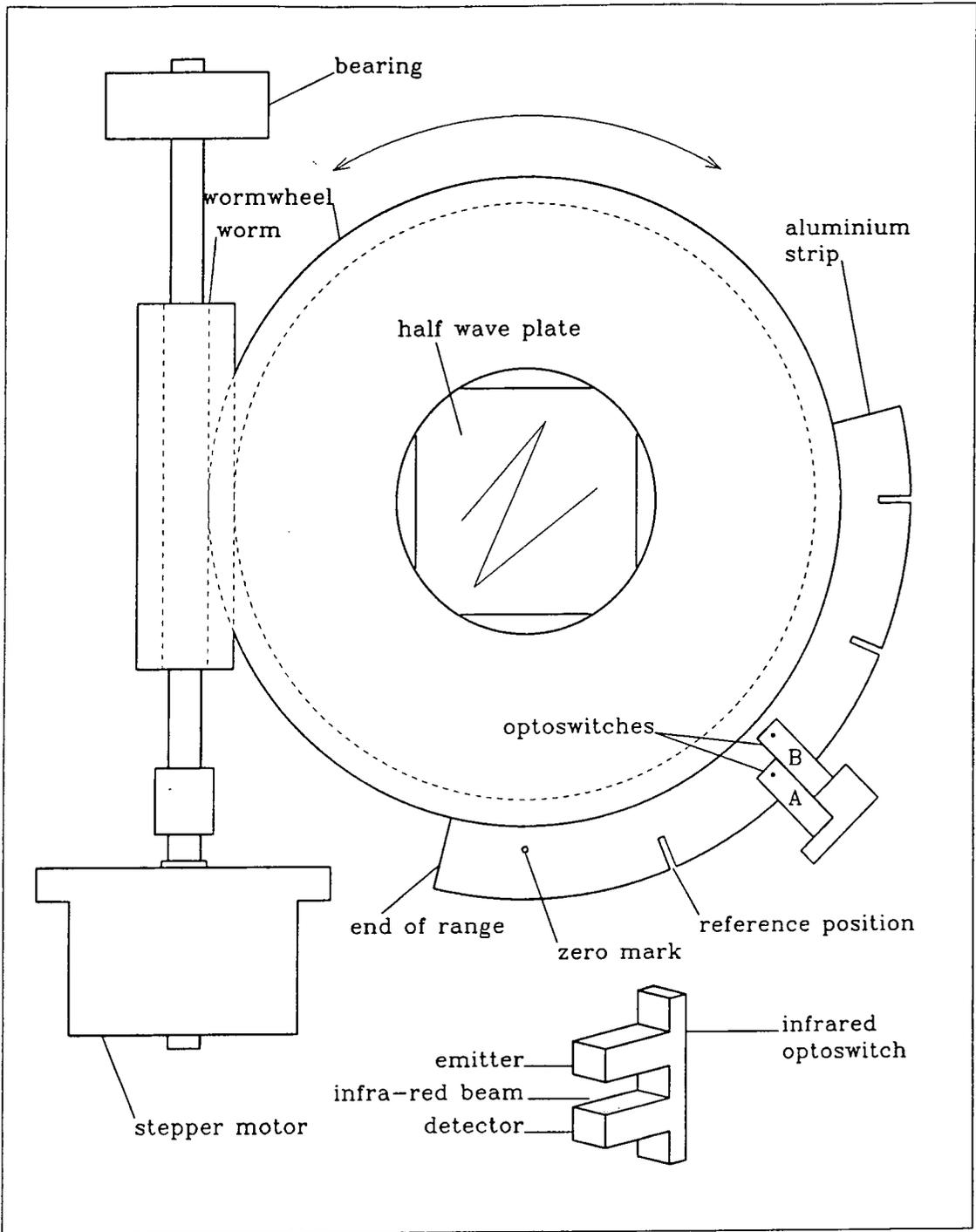
Figure 1.3: The encoder system, showing the infrared optoswitches and their positions with respect to the aluminium strip. A slotted infrared optoswitch is illustrated at the bottom of the diagram.
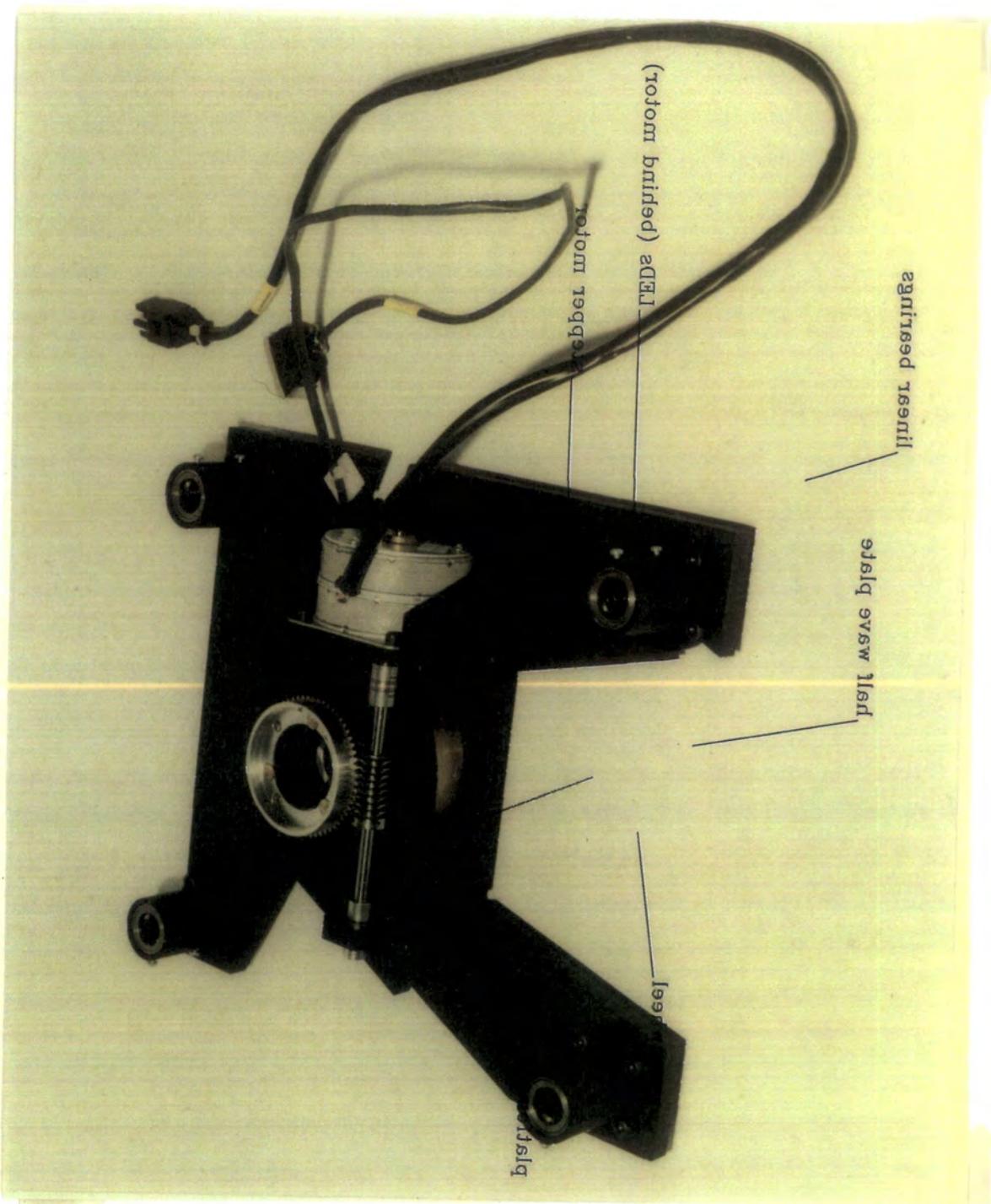
Figure 1.4: The half wave plate mechanism. The stepper motor and worm drive are clearly visible.

Using this arrangement it is possible to move the components to any position within the permitted range, by counting from the zero position past the short slots, until the one closest to the desired position is reached. Since the number of steps between the slots is known, an interpolation procedure can then be used to bring the component to the required place. The short slots mark the reference positions exactly, and a simple "hunting" procedure carried out each time one of these is encountered is sufficient to centre the optoswitch on the slot and eliminate entirely any errors introduced as a result of backlash.

1.6 The Apple & associated hardware

An Apple II personal computer is used to coordinate the control of the LEDs and stepper motors, and to carry out interpolation and checking procedures. It communicates with the polarimeter via an I/O card installed in one of the expansion slots. The TTL outputs (0-5V) from this card are stepped up by line drivers so that they can be sent down a relatively long cable to the polarimeter where line receivers convert them to TTL again. The line receivers are mounted with the motor control cards in the electronics rack on the side of the polarimeter, and allow remote operation of the polarimeter from a distance of up to ~ 100m.

A 30-way ribbon cable links the Apple with the polarimeter. This carries 3 lines to each stepper motor control card ("enable", "step" and "direction"), an "enable" line for the LEDs, 10 return lines from the 5 pairs of infrared detectors, and a return line to indicate LED failure. The drive cards for the stepper motors are identical and interchangeable, as are the motors themselves, so if a vital motor such as that moving the half wave plate fails it can easily be replaced by another that controls a less well used function (usually the grid viewing mirror).

The Apple is responsible for switching on the LEDs prior to moving a component, checking that all the LEDs are on, moving a motor by the appropriate number of steps to bring a component to the required position, then turning off the LEDs again before an exposure is made. A sophisticated suite of programmes,

written in Pascal by Dr. Rodney Warren-Smith, has been designed to carry out these apparently simple procedures. The programmes are automatically loaded from the floppy disc which is used to boot the computer, and provide a friendly interface for the observer.

1.7 Software for polarimeter control

The Pascal routines run by the Apple give the observer full control over the polarimeter and contain certain safety precautions to prevent anything untoward happening. The programmes are necessarily complex and will not be discussed in detail here; instead a short summary illustrating the capabilities of the system is given.

The most obvious routines that an observer needs are those which actually move the components to a specified position. Simple mnemonics allow the user to issue commands to do this in a straightforward manner, either being prompted for the new position or typing it on the command line. The half wave plate and mirror can only be set to specific positions marked by reference slots (0, 15, 14 or 13 for the half wave plate, and 0 (out) or 1 (in) for the mirror), whilst the other components can be set to any position within their particular permitted range—the programmes check that the required position conforms to these rules before activating any motors. Only one command can be issued at a time, and any operation which has been started will be completed before another is carried out.

If the requested position is acceptable the LEDs are switched on, and to check that they are all working the current through them is measured. The relevant motor is then activated and stepped in the correct direction to bring the component to the new position. The number of steps moved by the motor from the previous (known) position defines the position of the component at any time. The Apple continually monitors the outputs of the two optoswitches, decoding them to keep a check on the position of the aluminium strip, and whenever one of the short

reference slots is encountered the "hunting" procedure is implemented.

The hunting routine reverses the direction of a motor, taking the short slot past the optoswitch and continuing sufficiently far to take up any backlash, the outputs of the optoswitches indicating each edge of the slot as it passes. The motor's direction is reversed again and the process is repeated. An interpolation algorithm then uses the difference in the measured positions of the slot edges to calculate the amount of backlash introduced as a result of the changes in direction, and determines the position of the centre of the slot. The motor brings the component to this position, which is a known reference position, and the positional information which is held by the Apple can be updated accordingly. The motor can then drive the encoder to the desired position, repeating the hunting process if further reference slots are encountered.

Since the position of a component is always known the occurrence of the reference positions can be predicted. If the actual position of a reference slot is at odds with the predicted position then an error message is reported. This might be the case if, for instance, a component had been moved by hand during some maintenance work, in which case the Apple's record of its position would not have been updated.

Software routines are used to gently accelerate the motors from rest to a maximum speed of 100 steps per second, which appears to be an efficient speed causing minimal vibrations. As a reference position is approached the speed is reduced to give a more accurate measurement of the slot position, and when the desired position is reached the motor is gradually decelerated to rest.

A reset facility exists to enable the observer to bring a component back to the zero position, as defined by the hole in the aluminium strip. When the hole is reached the hunting process is used to bring the LED's beam concentric with it, so the position as recorded by the Apple can be reset to zero. A verification procedure makes use of this process to check that a component is the expected number of steps away from the zero position. The operator can verify a component's position

at any time, but verification will be automatically carried out at regular intervals defined by the user (usually every fourth time a component is moved).

If, as a result of some malfunction or forced movement of the component, the position of the optoswitches moves beyond the end of one of the encoder strips, the output from both of them will be high and the motor will be disabled immediately to prevent possible damage. No further operations with this particular component will be possible until the operator uses a recover command to enable the motor again, followed by a reset to return the component to the zero mark and regain positional information. This action protects the components from being driven beyond their physical range of travel, which might be damaging, and also serves to alert the user to a possible problem (for example the hole marking the zero position has got blocked and is not being detected).

It is useful when developing a system such as this to be able to repeat a procedure many times in order to analyse its performance. With this in mind a routine has been written to exercise a component; that is, to repeatedly move it to new positions. The Apple requests a component to be moved to a random position within the allowed range, then moves it to that position, verifying by returning to the zero mark after every four moves.

Conversely, it is sometimes useful to be able to prevent a component from being moved, and this can be done with a software locking procedure which will not allow any further movement until an unlock command is received. This does not lock the components mechanically, so they could be moved by manually turning the gears in the polarimeter, but it does prevent accidental or unwanted movements, caused by unauthorised interference with the Apple keyboard.

Finally, a help command enables the inexperienced observer to obtain a summary of the command mnemonics and their meanings—this is listed on the screen of the Apple's monitor.

1.8   Use of the polarimeter

The automated polarimeter has been in use since the beginning of 1988, and has proved to be reliable and simple to use—the abundance of papers which are based on observations made with the instrument bear out this fact. All the data presented in this work were obtained using the automated polarimeter.

Chapter 2

The CCD camera system

For almost a decade the detector used in conjunction with the Durham Imaging
Polarimeter was an electronographic camera, developed at the RGO by Dr. D.
McMullan (McMullan *et al.*, 1972). This combination of instruments was highly
successful, but the electronographic camera was ultimately replaced in 1984 by
a charge-coupled device (CCD), which is easier to use and has few of the draw-
backs associated with the electronographic camera. The advantages of CCDs over
electronographic film, with particular application to the Durham Polarimeter, are
discussed in detail by Draper (1988), who also gives a thorough quantitative com-
parison of the two detectors.

This chapter describes the hardware which is currently used to control the
CCD, and the software which is used when observing. Attempts to enhance the
blue response of the CCD are also discussed.

2.1 CCDs and their spectral response

The spectral response of the electronographic camera is compared with .that of a
GEC P8603 CCD (as used with the Durham polarimeter) in figure 2.1. Whilst the
CCD is far more sensitive at wavelengths longer than ~ 500nm it is immediately
apparent that the efficiency of the electronographic camera is much higher in the
blue region of the spectrum. Since many reflection nebulae are characteristically
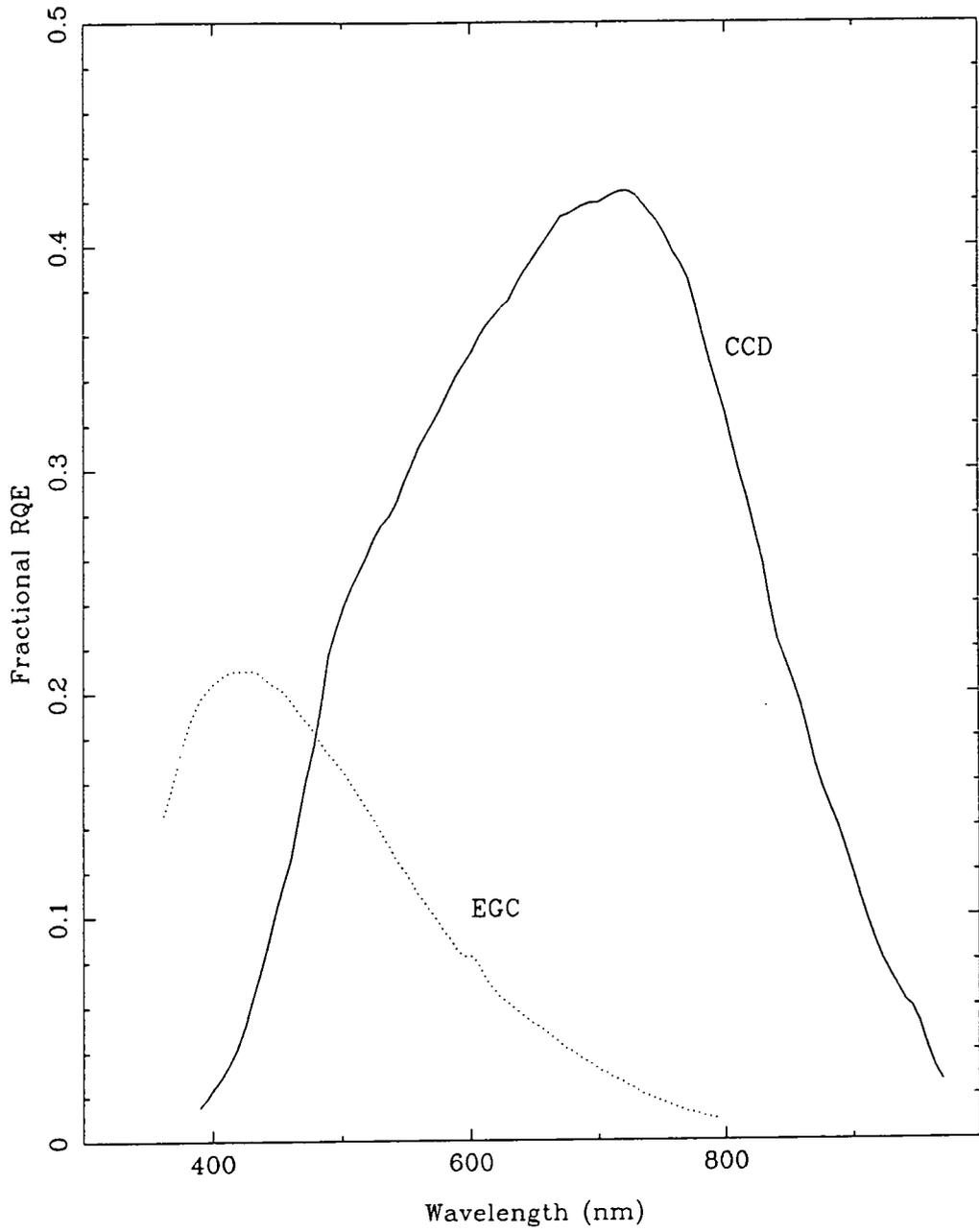
Figure 2.1: The spectral responses of an electronographic camera and a GEC CCD.

blue in colour, due to the higher rates of scattering at shorter wavelengths, this is a notable disadvantage when CCDs are used to for making images of these objects, but it is one which has been recognised and consequently investigated in order to overcome it.

Before looking at possible ways of improving the response of CCDs to short wavelength radiation (300–500 nm) it is first necessary to understand the principles behind the construction and operation of a CCD, since it is the physical structure of the CCD that determines its characteristic spectral response (charge handling and transfer will omitted here since it has little relevance in this context; for a discussion see Beynon and Lamb, 1980).

2.1.1 Buried channel CCDs

Most CCDs currently in use in imaging applications are of the buried channel type, with a structure similar to that shown in figure 2.2. A lightly doped semiconductor substrate (p-type in this example) is overlaid with a thin layer of epitaxial semiconductor more heavily doped with majority carriers of the opposite charge (i.e. n-type). On top of this is a layer of semiconductor oxide, which acts as an insulator between the substrate and the polysilicon electrodes to which the clock voltages are applied in order to transfer charge across the chip.

At the p-n junction between the two types of doped semiconductor a depletion region forms. The application of a reverse bias, V_B, to the top layer of semiconductor causes this region to widen, and also introduces a similar region beneath each of the electrodes (which are held at ground potential, V_G). If a high enough voltage is applied the field-induced depletion regions will meet, forming a plane, parallel to the surface of the device, where the potential reaches a maximum value. A potential well is therefore formed in the substrate beneath each electrode; these wells comprise the so-called "buried channel" after which the device is named.

A photon incident upon the CCD passes through the polysilicon electrodes and the insulating oxide into the doped silicon below. Eventually it will be absorbed
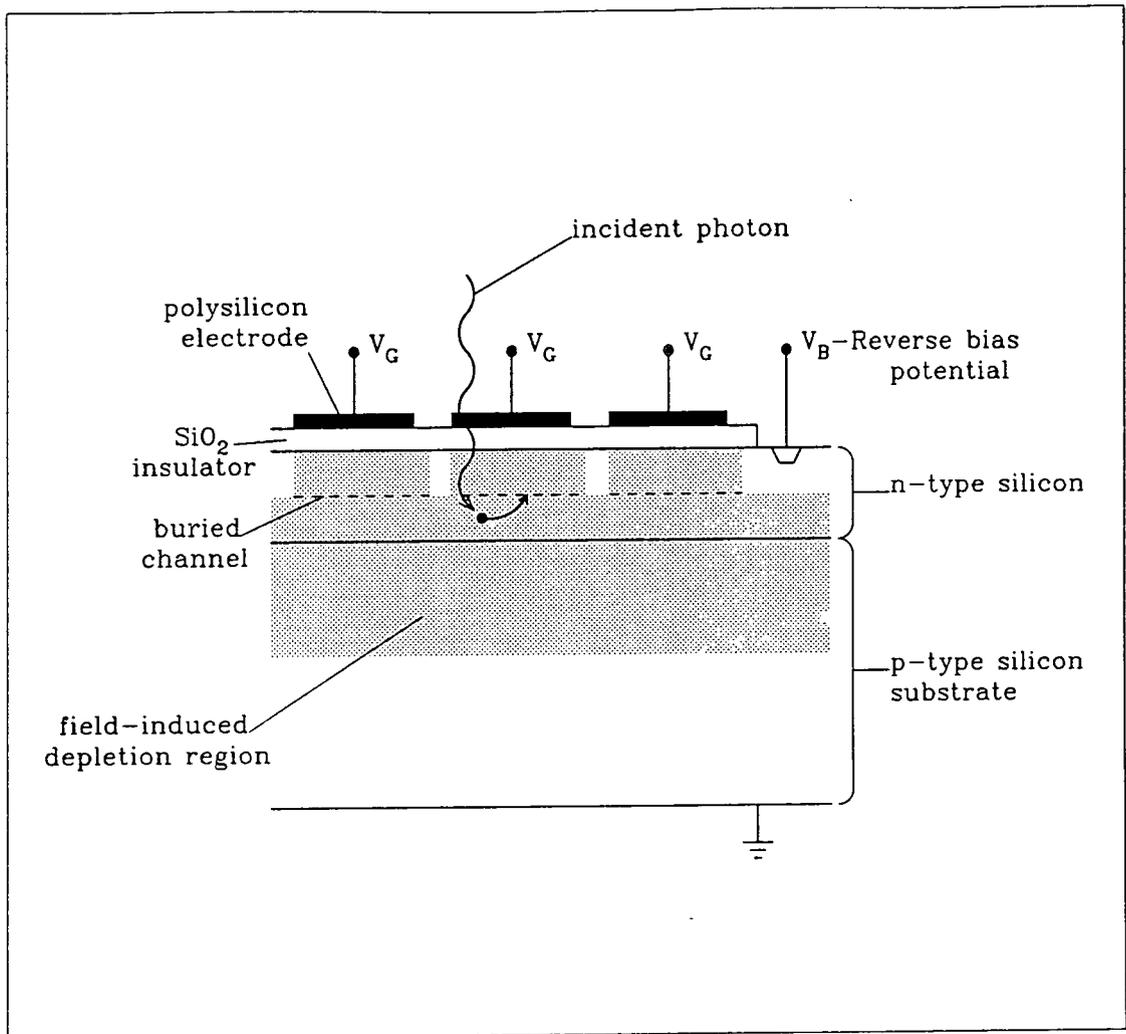
Figure 2.2: Schematic cross-section of a typical thick, buried channel CCD. An incident photon is shown releasing an electron, which moves into the nearest potential well.

by the silicon lattice, forming an electron-hole pair and releasing a majority charge carrier into the conduction band. The newly-released carrier will be attracted to the nearest potential well where it will be held, and hence charge builds up proportionally beneath each electrode according to the intensity of radiation incident upon it. The array of pixels which make up a CCD image corresponds to the array of electrodes on the surface of the chip, each pixel being composed of three clocking electrodes in the case of a three phase device.

The spectral response of such a device is basically that of the doped silicon which absorbs the incident light, modified by the absorption spectrum of the polysilicon electrodes through which a photon must pass before it can be detected. The polysilicon electrodes are virtually opaque to radiation with a wavelength of less than ~ 400nm, and become increasingly transparent at longer wavelengths. Since the response of the silicon substrate is lower in the blue than in the red region of the spectrum this effect is particularly undesirable and causes the observed low efficiency at short wavelengths evident in figure 2.1. In order to minimise this inefficiency it is therefore necessary to reduce the number of photons that are absorbed by the polysilicon electrodes.

2.1.2   Thinned CCDs

The first and most obvious way of increasing the sensitivity of the chip in the U and B wavebands is simply to illuminate it from the other side, i.e. through the substrate rather than through the electrodes. The substrate must then be made relatively thin to make sure that charge carriers released by the absorption of photons close to the surface can reach the potential wells in the buried channel under the electrodes with minimal degradation. If the chip is made too thin, however, the longer wavelength photons ($\lambda \gtrsim 800$nm) will pass straight through without being absorbed at all, so a compromise must be struck. A thickness of $\sim 10\mu$ is generally accepted to be satisfactory in the 300–900nm waveband (compared with $\sim 100\mu$ for a typical front-illuminated CCD).

Although RCA do produce such thinned, back-illuminated chips, it has been found that their thinness introduces new problems; thin chips are not rigid enough to maintain a perfectly flat surface, and are more fragile than conventional thick chips. In addition multiple reflection and interference in the thin substrate layer causes fringes, in much the same way as Newton's rings are produced by a thin layer of air between two pieces of glass. This problem is worsened by the fact that the surface of the substrate cannot be manufactured to within one wavelength accuracy.

It might be thought that the fringes caused by thinning a CCD could be removed by careful flat-fielding, but this is not necessarily the case. The most noticeable fringes are caused by bright monochromatic radiation, such as emission lines in the sky spectrum, and if an object in the field of view also has bright emission lines then it too will cause fringing effects, but at a different place on the chip. The night sky fringes could possibly be removed if flat fields are made on the dark sky rather than on twilight sky (which will show the same emission lines but with different amplitudes) or a screen inside the telescope dome (which will show no emission lines), but the object fringes cannot be removed by simple flat-fielding techniques. The problem will be worse when observing bright nebulae which may be seen wholly or partly in emission-line radiation than when observing galaxies.

2.1.3   Coated CCDs

A more subtle way of increasing the sensitivity of a CCD at short wavelengths is to effectively convert the wavelength of the incident photons, changing it to one for which the response of the silicon is higher. This can be done using a laser dye which absorbs photons of one particular wavelength, then fluoresces proportionally at another, longer, wavelength. In practice CCDs are coated with a thin layer (3–4 microns) of an acrylic plastic which has been doped with series of laser dyes, each of which causes a wavelength shift of about 100nm. In this way blue photons incident upon the coating cause it to fluoresce in the red waveband—the region

where the chip is most sensitive. The only drawback with this method seems to be a deterioration of the quality of the coating with time, particularly if the CCD undergoes many cooling and warming cycles, but since the coating can easily be dissolved off and replaced this is not a major problem.

In figure 2.3 the spectral response of a GEC P8603 chip coated in this manner is compared with that of a similar uncoated chip—the effect of the coating can be clearly seen as an increase in sensitivity below 480nm. The response of the coated chip across the rest of the spectrum is slightly better than that of the uncoated device. This may simply be because the CCD itself is more efficient than the uncoated one across most of the optical spectrum, but the important point of note is that the coating does not seem to have an adverse effect on the sensitivity at wavelengths longer than 500nm. Since the layer of fluorescent dye is thin it causes no significant loss of resolution in the U and B bands even though the fluorescent radiation is emitted isotropically (Cullam *et al.*, 1985).

2.2   The Durham CCD

After the original CCD had been used successfully with the Durham polarimeter on several occasions a second GEC P8603 chip was acquired. This was coated with fluorescent dye by Sebastien Deiries using the technique developed at ESO, so that the curves shown in figure 2.3 represent the responses of the original uncoated CCD and its coated successor.

As well as being more sensitive, particularly in the U and B wavebands, the new chip was found to be superior to its predecessor in that the readout noise, which can be measured by making unexposed readouts of the CCD, is slightly lower (7-9 electrons per pixel, compared with ~ 11). The cosmetic quality of the new CCD is also better than that of the old one; to date no bad pixels have been found on the coated CCD, whereas the original device has three bad columns and several isolated dead pixels. The dark current of the new chip is very low (no current measurable in 60 minutes at 110K), and the linearity is good, making this
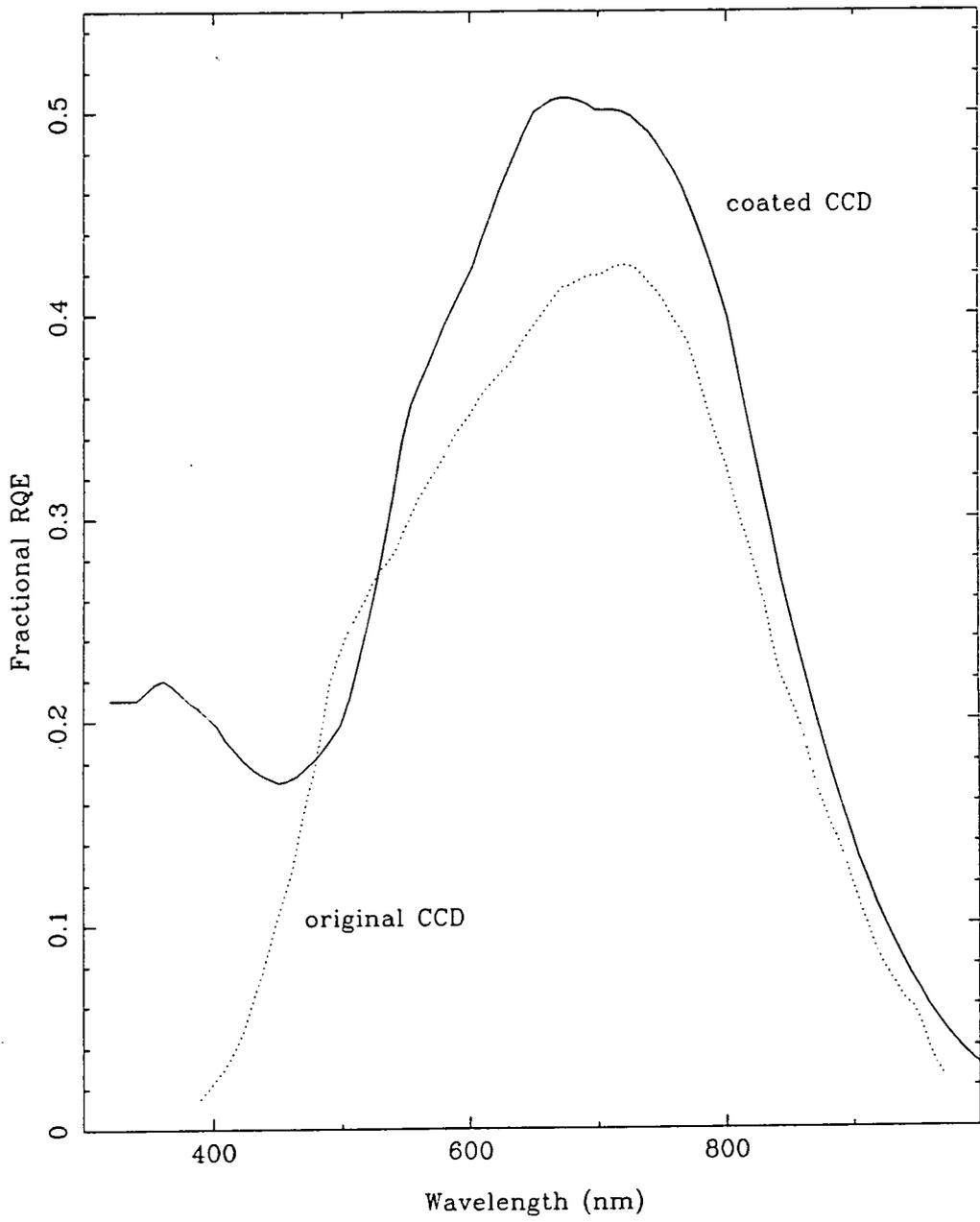
Figure 2.3: Graph comparing the responses of an uncoated and a coated GEC CCD.

device an excellent detector for use with the Durham polarimeter.

2.3 Associated hardware

2.3.1 The dewar and shutter assembly

In order to reduce the number of charge carriers that might be freed by thermal energy in the semiconductor lattice (the dark current) the CCD has to be cooled to a temperature of $\sim 130K$. This is done by mounting it on a copper block in an evacuated chamber, connected to a reservoir of liquid nitrogen by a copper braid. This arrangement is held in a dewar containing strategically placed temperature sensors for remote monitoring, with a window on the front face to allow light to reach the CCD. The vacuum prevents the formation of condensation on the chip, and insulates both the CCD and the nitrogen reservoir from the warming effects of the ambient air.

Mounted on the front face of the dewar over the window is an electronic shutter which is used to prevent light reaching the CCD, except at specific times when exposures are to be made. In the original polarimeter design the shutter was incorporated in the polarimeter itself (Scarrott et al., 1983) between the prism and relay lens. The fact that the shutter assembly is now mounted directly on the dewar means that the dewar can be safely removed from the polarimeter without fear of the CCD being saturated by bright incident radiation. There is, however, a disadvantage of having the shutter mounted in this position, in that the assembly encloses the window completely and acts as a trap to moisture, which can lead to condensation forming on the outside of the window. This undesirable effect has now been overcome by incorporating in the polarimeter design a device which feeds dry nitrogen into the cavity between the dewar and polarimeter; during an exposure when the shutter is open the nitrogen flushes through the shutter assembly, removing any unwanted moisture.

2.3.2   The PC and peripherals

Riding on the side of the polarimeter with the polarimeter electronics rack is another rack of electronics which contains the power supply and drivers for the CCD and shutter. This provides the clock and bias voltages for the CCD, monitors the chip temperature, converts the analogue CCD output to a digital format, operates the electronic shutter, and communicates with the controlling computer via a single coaxial cable and an interface unit.

Initially the coated CCD was controlled by a Data General Nova 4/C computer and its associated hardware, running the DORADO suite of programmes as described by Draper (1988). As far as the collection of data was concerned this arrangement was perfectly adequate, but the excessive weight of the Nova, external Winchester disc drive, frame store, and tape unit, proved costly and caused handling problems whenever the equipment had to be moved. In view of this a new, more portable, system was developed, and this has now been used successfully at various observatories around the world for almost two years.

The new system is based on an Elonex PC286S-100 machine—a 16-bit personal computer compatible with the IBM PC-AT. This is used for both CCD control and image display, and contains an integral 80Mbyte hard disc on which data can be stored. In addition to this, data can be stored on floppy discs, half-inch magnetic tape, or data cartridges, depending on which type of archive device is available or preferred. Operation of the PC is very straightforward for the observer, who communicates with it using a graphics tablet and a conventional keyboard. Information on the current status of the instruments is presented on a VDU with EGA capabilities, whilst images are displayed on a multisync monitor. The hardware used for both CCD and polarimeter control is shown schematically in figure 2.4.
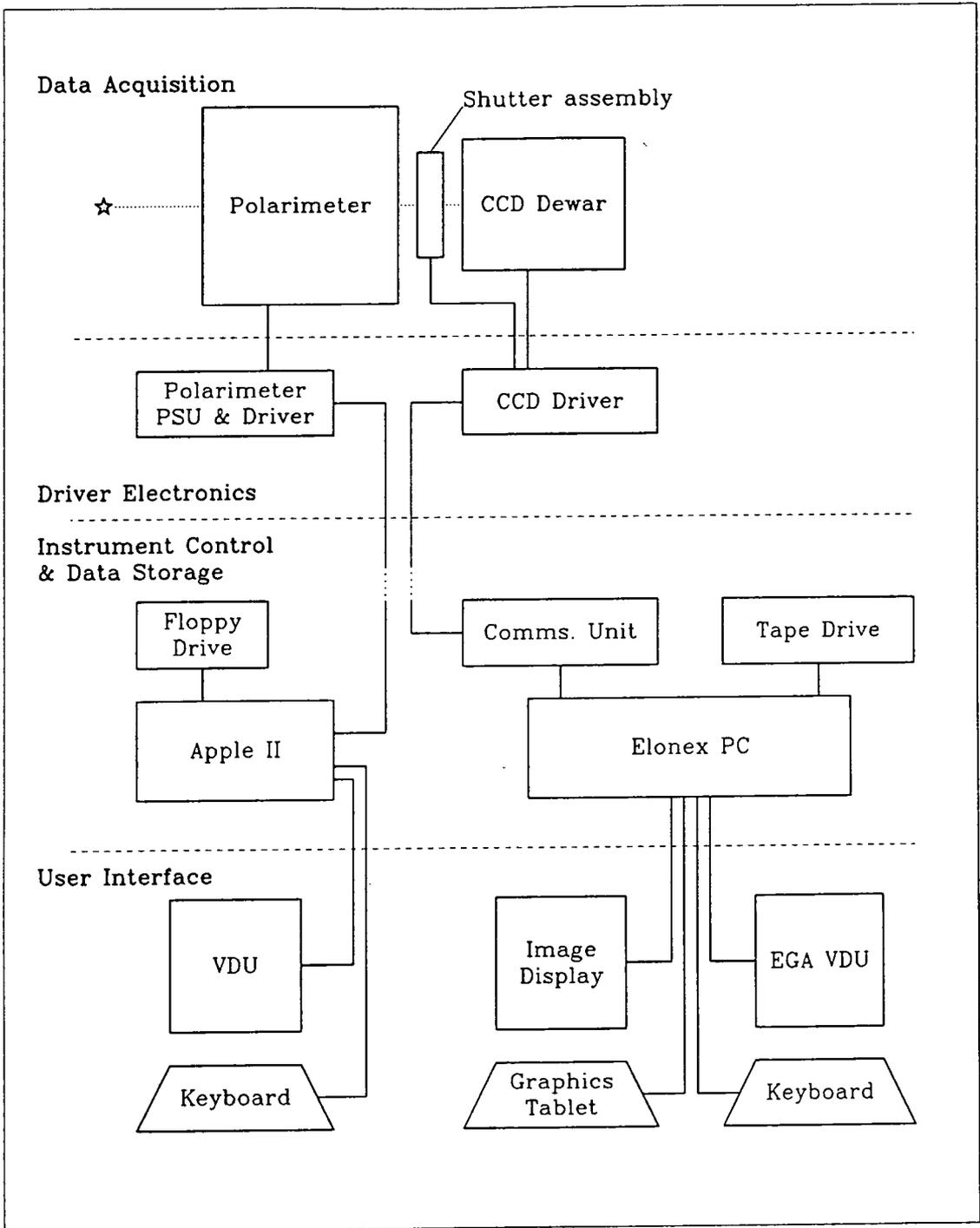
Figure 2.4: Schematic diagram showing the hardware used for both polarimeter and CCD camera control.

2.4 Software

The software used for image display and CCD control is a commercially available package called Imager (produced by the Cambridge company, Astromed), which has been adapted by the author to suit the needs of observers working with the Durham polarimeter. Only a brief summary of how the system operates will be given here; for a more explicit description see appendix A, which is taken from the user manual written to aid observers.

The software is based upon Draper's DORADO, and is commonly known as DUPCAT (Durham University PC-AT) for want of a better acronym. It runs under the Unix operating system, and consists of a set of macros, each of which performs a particular function or series of functions by executing Imager programmes and/or Unix shell scripts. The programmes are all written in the C programming language, but are supplied in a fully compiled and executable form so that an observer with no knowledge of Unix or C can use them easily.

The DUPCAT macros give the user complete control over the CCD and enable him to perform relatively complex operations with ease. Unfortunately it is only possible to monitor the chip temperature via a display on the rack of controlling electronics, which is necessarily mounted on the telescope next to the dewar, so occasional trips must be made to the observing floor to check that the dewar still contains sufficient liquid nitrogen to keep the CCD cool. Apart from this the programmes allow the CCD camera system to be operated completely remotely, so the observer can locate himself at a convenient distance from the telescope. Ideally both the Elonex and the Apple would be situated in the telescope control room in order to minimise the number of people required and to maximise the efficiency of the observing run.

One great advantage that the DUPCAT system has is that macros can be selected by the observer using a mouse and graphics tablet. The tablet is a digitising device which reads the absolute position of the mouse on its surface; each macro

is assigned to an area of the tablet (approximately 2.5cm square) and is executed simply by choosing the relevant region of the tablet with the mouse. Occasionally the keyboard is also needed—to input numerical information such as the exposure time, for example. The user can therefore treat the PC as a "black box"; an interface between him and the CCD whose details need not be known or understood, yet which gives him full control over the CCD camera system.

The prime aim of the software is to enable the observer to make relatively long exposures of objects in the simplest manner possible. The macros have been designed in such a way that each one, once selected, performs and completes a specific task and leaves the system in a state ready to receive the next command (usually from the graphics tablet). There are of course instances when the user inevitably has to be prompted for some value (the name of an object, for example), but these are kept to a minimum—this makes for more comfortable observing.

For documentation purposes, and also for an aesthetically pleasing and ergonomic layout on the graphics tablet, the macros have been divided into three groups: those that are primarily concerned with controlling the CCD and collecting and storing data, those that are related to the way in which the image is displayed, and miscellaneous macros which serve other purposes.

2.4.1   CCD control

Although making an exposure only involves opening and closing the shutter at specified times and then reading out the CCD to a memory buffer, the macro used to do this is considerably more sophisticated. When exposures are made the resulting image is displayed on the multisync monitor, the name of the object and the exposure time are written to a database on the PC's hard disc, the image itself is automatically written to disc, and it is also written to tape if there is a tape drive on-line. The macro also carries out checks to make sure that the shutter is closed before and after exposures, and flushes the chip to free it of charge before an image is recorded. Exposures may be interrupted at any time in order to free

the graphics tablet for some purpose, perhaps to adjust the displayed data range, then the exposure can either be terminated immediately or allowed to finish after its allotted time. There is a macro which can be used when an exposure has been interrupted to see how much time the shutter is due to remain open for—this macro can also be used at any other time to find out whether the shutter is closed or not. The shutter can simply be opened and closed from the graphics tablet if required.

In addition to the macros used for making actual observations and storing data there are others which experience has shown to be necessary. For acquiring objects there are several macros which repeatedly expose the CCD and read out part or all of it, with an optional zoom facility which expands the image to fill the screen of the multisync monitor. These speed up the object-finding process since exposures of the field of view can be made continually as the telescope slews across the sky. There is also a macro which can be used when focussing the telescope; it makes a series of exposures without reading out the chip until the last one has been made. The focus and position of the telescope are changed slightly between each exposure so that the resulting frame contains a set of images made at different foci, which can readily be compared with each other. Test exposures can be made to check that the proposed exposure time is of the right order and that the required object is in the field of view and not hidden behind one of the occluding bars of the grid assembly. These will not automatically be saved, but can be stored on disc and/or tape if the observer so desires.

During the day when the CCD is not being used a simple macro continually flushes and reads it out—this ensures that it is always in a charge-free state and ready for observations to be made.

2.4.2   Image display

All aspects of image display are covered by the macros available to the observer, who can use the graphics tablet to choose to display any frame which exists on the

hard disc, or which can be read off a tape. Images are scaled, either using a fast autoscaling algorithm, or according to a preferred range which is typed into the keyboard, then displayed with either a grey or colour lookup table. The contrast and brightness of a displayed image can be changed using the graphics tablet and there are two macros which provide pan and zoom facilities. The image can be transposed if required, and subtracted from a laterally shifted copy of itself to give a mock relief image, ideal for looking at fine details which are highlighted by this process.

There is a slight problem in using the graphics tablet to control the image display in this way, inasmuch as the display cannot be altered while another process is running (while an exposure is being made, for example) unless that process is halted. In practice this has not been found to be a great disadvantage, since the macros have been designed to give the observer as much freedom as possible, giving him the opportunity to change the display range between exposures if he so desires.

2.4.3   Miscellaneous macros

There is also a selection of miscellaneous macros which do not fit conveniently into either of the two categories described above. Included among these are programmes to dump frames to tape or floppy disc and to read them back again, which might be useful if, for some reason, the automatic tape-dumping process after each exposure were to fail or if tapes were not available during the night. In this case images can be stored on the hard disc until the end of the night, when they can be copied to the archiving device and cleared from the disc, freeing space for the next night's data. An initialisation procedure is required to skip over the frames on a partially used tape and prepare it for receiving new data, and there is also a macro that will rewind a full tape back to the beginning.

It is often useful to be able to look at the actual pixel values of a region of an image, and this can be done using one of two profiling macros, which plot a

histogram of the pixel values along a line between a pair of interactively defined points.

It is of course necessary to keep a check on the amount of available space on the hard disc, and to delete frames when the disc fills up. Macros have been written to enable both of these operations to be carried out using the graphics tablet, which avoids the tedium of typing complex and barely comprehensible commands into the keyboard and which is therefore more convenient for the observer with no knowledge of Unix. If the macros defined on the graphics tablet are found to be inadequate for some particular task there is a macro which will switch the control to the keyboard so that the confident user can type in his own string of commands, or define a new macro. A similar macro exists to exit from the Imager software altogether and return to the Unix Bourne shell.

2.5 The first use of the DUPCAT system

The DUPCAT system was used with the automated polarimeter for the first time in January 1989. The hardware proved to be straightforward to set up, and the suite of macros was easy to use. No major problems were encountered; data acquisition and image display were accomplished rapidly and with the minimum of fuss. Observations were made of several objects, including the Re10 and Re17 nebulosities, HH120 in the cometary globule CG30, the nebula around the OH 231.8+4.2 maser source, and the disc around β-pictoris. Of these only the observations of HH83/Re17 and OH 231.8+4.2are included in this work (see chapters 3 and 6). To date a total of four papers (Rolph *et al.* 1990, Scarrott, Gledhill, Rolph & Wolstencroft 1990, Scarrott, Rolph & Wolstencroft 1990, Eaton *et al.* 1990) have been published as a result of the initial observing run in January 1989; these are merely the first of a large number of papers produced as a direct result of observations made using the automated polarimeter with the Elonex PC running the DUPCAT software, and bear testimony to the ability of the system to produce good quality polarimetric data.

2.6   What the future holds

The current system is satisfactory as it stands, but rapid developments in computer hardware permit us to dream of projects that may not be as far removed from reality as we once thought. In line with massive increases in computer power and storage potential the Durham polarimeter continues to evolve, and now that the automated polarimeter has proved its worth a second is being designed. Lessons learnt during the construction of the first instrument will be applied as the new one is built, in order to improve upon the present model wherever possible.

It is envisaged that, as well as controlling the CCD, the Elonex PC will also replace the Apple and control the new polarimeter, with commands being issued from the graphics tablet to both instruments. From there it would be a relatively trivial step to write programmes which would make whole sequences of exposures, reading out the CCD and moving the half wave plate between each one. The observer would then be free to operate the telescope or reduce data whilst the observations are being made.

The recent acquisition of a VAXstation 3100 with a 450 Mbyte hard disc will allow preliminary data reduction to be carried out at the observing site, with CCD images being transferred from the PC to the VAXstation as soon as the CCD is read out. Thus it will be possible to judge the quality of the incoming data and adjust exposure times or focus positions accordingly, in order to optimise the use of the polarimeter and telescope under any particular conditions and so to reach their full potential. It might also be useful to have the PC running as a slave to the VAXstation which would issue commands to make a sequence of exposures; the DECwindows software would allow this to be done in one window on the VAXstation's monitor, whilst another could be used for data reduction, and possibly a third for image display.

In principle it should also be possible under Unix to run the tape-dumping process when the PC's processor is inactive, i.e. while an exposure is being made.

At the moment about 20 seconds are wasted after each exposure while the frame is written to tape. This time can amount to over half an hour per night, so if it could be eliminated the total time available for observing could be significantly increased.

Chapter 3

HH83/Re17

HH83 (also known as Re17; Reipurth 1985) is a nebulous object located at the western edge of the L1641 dark cloud in Orion. Associated with the object are several characteristics of star formation; nebulosity, emission line jet, bow shocks, and an IR source (IRS). In this chapter an optical polarisation map of the HH83/Re17 nebulosity is presented, and from it the location of the source of excitation is derived. The geometry of the system is also discussed. These results demonstrate the ability of the automated polarimeter and DUPCAT CCD camera system to produce good quality polarisation maps.

3.1 Previous studies of HH83/Re17

Whilst it has been established that Herbig-Haro (HH) objects are indicators of very recent star formation their morphology and excitation conditions vary greatly, making the construction of simple models quite difficult (see the review by Schwartz, 1983). In an effort to determine the general properties of HH objects, Reipurth (1985) conducted a survey of the L1630 and L1641 dark clouds and discovered 41 small nebulae, at least 14 of which have proved to be HH objects (Reipurth 1989). One of these nebulae, HH83/Re17 has a highly collimated jet, 32″ long and perpendicular to the major axis of an elliptical nebula which is thought to be seen by reflection. An IRS was found on the axis of the jet, close to the nebu-

losity; its position is in agreement with that of a far-infrared (i.e. maximum flux is measured at 100μ) IRAS source which is assumed to be the illuminator and exciting source of the system. Wouterloot *et al.* (1988) detected emission from the (1,1) ammonia transition at this position; this is an indicator of dense molecular cores. Reipurth (1989) compared an optical image of the HH83/Re17 region with the ^{13}CO map of L1461 made by Bally *et al.* (1987), and showed that HH83/Re17 is associated with a $15M_\odot$ molecular cloud clump, despite being outside the main body of the dark cloud. Bally (1989) reports the discovery of a large-scale CO disc associated with HH83/Re17; the axis of rotation of the molecular disc is aligned with the optical jet.

Further investigations by Reipurth led to the discovery of bow shocks colinear with the jet on either side of the source, $150''$ and $250''$ away from it. Long slit spectroscopy demonstrated an increase of radial velocity along the jet, and a change in the excitation conditions, with the SII/Hα ratio steadily increasing with distance from the source. The termination of the jet at one of the bow shocks is seen purely in Hα emission and has a much lower velocity than the rest of the jet, which is indicative of significant braking. Although several theories, including magnetic collimation and acceleration, geometrical effects, and explosive ejections of material, have been proposed to explain these features of the jet (see Reipurth, 1989), none of them allows an unambiguous observational test and it is currently not possible to rule any of them out.

The nebulosity is thought to be seen by reflection but there is no obvious optical illuminator on the axis of the jet; optical polarimetry of the nebula, however, allows the exciting source to be identified.

3.2   Observational details

Observations of HH83/Re17 were made at the f/15 focus of the 3.9m AAT. The Durham Imaging Polarimeter was used in conjunction with the Elonex PC-AT and the DUPCAT software to make three sets of four exposures, each of 300s duration.

No filter was used so that the observations covered the waveband 400-1000nm, with peak response at 675nm. The image scale corresponded to 0.32 arcsec pixel^{-1}, and the atmospheric seeing was ~ 1.5 arcseconds. Data reduction was carried out according to the procedures described by Draper (1988) and Warren-Smith (1979).

3.3 Results

Figure 3.1 shows greyscale intensity images of the HH83/Re17 nebulosity. Structure can be seen in the nebula at high brightness levels, and at lower levels the highly collimated jet is clearly visible. A cross marks the position of the 2μ source found by Reipurth; at the wavelengths studied here no source can be seen. The field studied here is not sufficiently large to include the bow shocks discovered by Reipurth.

In figure 3.2 intensity contour and linear polarisation maps of the HH83/Re17 nebulosity are shown. The majority of the nebula is polarised to a fairly high degree ($\gtrsim 20\%$); the polarisation vectors are arranged in a centrosymmetric pattern suggesting that it is a reflection nebula. No polarisation is measured along the jet.

3.4 Discussion

3.4.1 The illuminating source

The centrosymmetric pattern of polarisation vectors over the nebula is typical of simple reflection nebulae, and can be used to identify the position of the illuminating source, since this will be at the centre of the circular pattern. The pattern locates the source outside the visible nebula at the position $\alpha = 05^h 31^m 06\overset{s}{.}44 \pm 0\overset{s}{.}2$, $\delta = -06°31'48'' \pm 3''$ (1950). This position is marked on figure 3.2 and is coincident, within errors, with the 2μ source found by Reipurth and the far infrared source IRAS 05311-0631. Clearly the optical illuminator and the two IR sources are one and the same object.

By fitting a black body curve to the observed IR spectrum Reipurth estimates
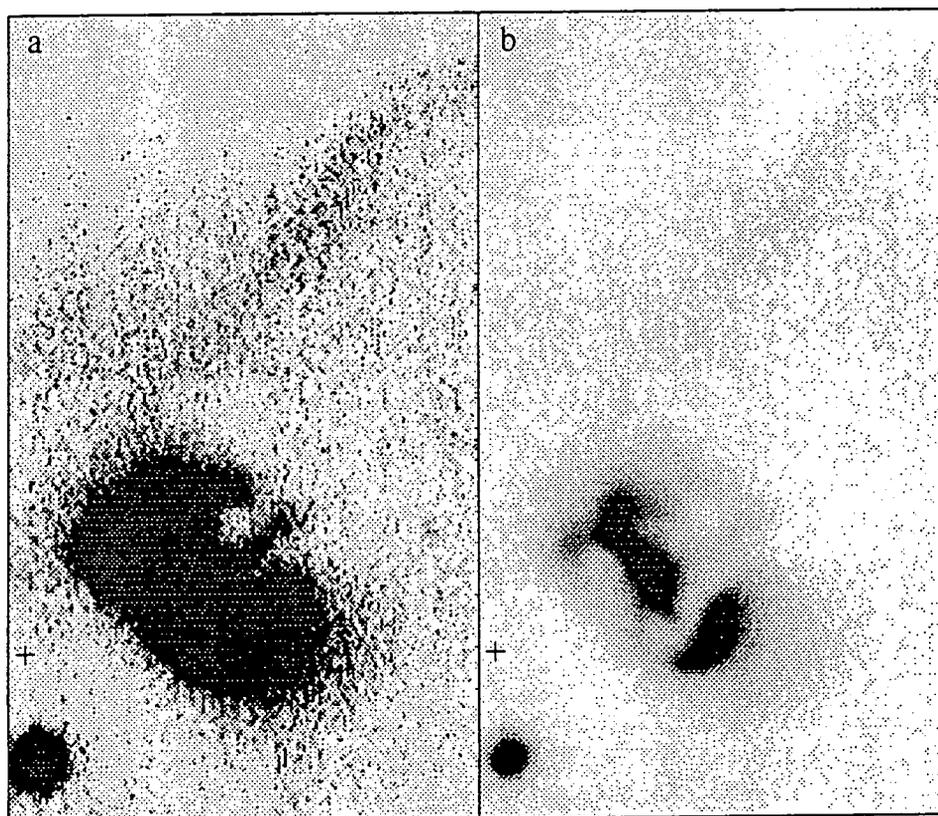
Figure 3.1: Greyscale intensity images of the HH83/Re17 nebulosity showing the structures at low (a) and high (b) brightness levels. The position of the nearby IRS is shown.
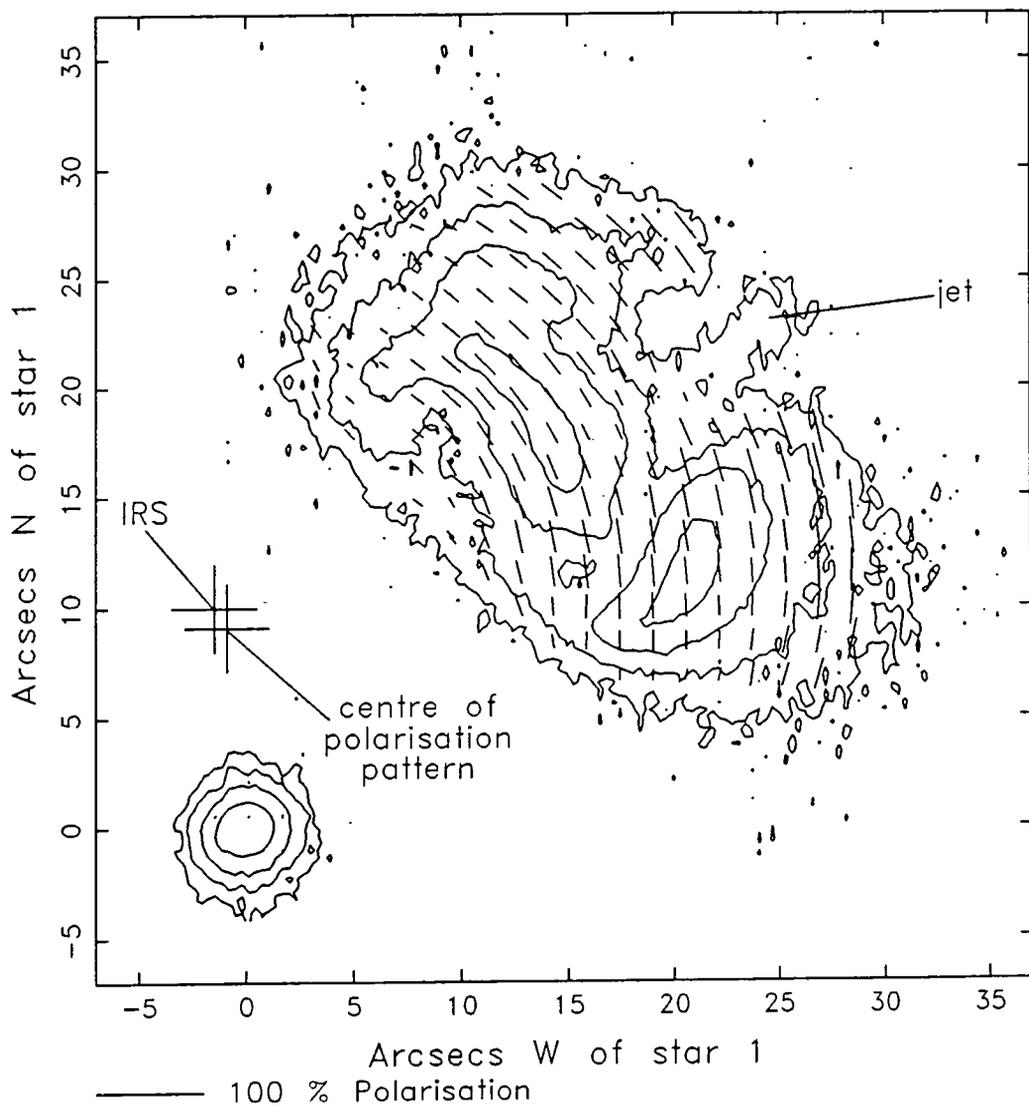
Figure 3.2: Intensity contour and polarisation maps of the HH83/Re17 nebulosity. The position of the nearby IRS is shown and the centre of the polarisation pattern is indicated.

the luminosity of this source to be $9.5L_\odot$ at a distance of 460pc. The source is not seen at optical wavelengths and must be obscured from direct view, but is able to illuminate nearby material to produce the visible reflection nebula.

3.4.2   The collimated jet

Although the jet is seen in the broad band intensity image of figure 3.1 no polarisation is measured along its length. This is dramatically demonstrated by figure 3.3 which shows a greyscale polarised intensity image of the nebulosity; unpolarised features such as field stars and the jet are notably absent. This is confirmation that the radiation from the jet is not scattered from the IRS but originates within the jet itself, as expected for an emission line feature.

Reipurth identifies ten knots in the jet; of these only the brightest three (D, F and G) can be seen in the images of figure 3.1. In the broad waveband studied here the sky is probably far brighter than the knots of the jet which emit radiation only in narrow spectral lines.

3.4.3   The reflection nebula

The intensity contour map of figure 3.2 shows that the luminous structure of the HH83/Re17 nebula is fairly complex, with a series of arcs and knots. In contrast, the polarisation map in the same figure shows that there is little variation in the level of polarisation over the nebula, with the exception of the jet region. This suggests that the observed structure is predominantly due to illumination effects.

Figure 3.1 shows that there is a wisp of faint nebulosity extending to the NW of the bright elliptical reflection nebula. Aperture polarimetry along this streak shows that it is polarised by $\sim 20\%$, at a PA that is consistent with illumination by an optically obscured source at the position of the IRS.
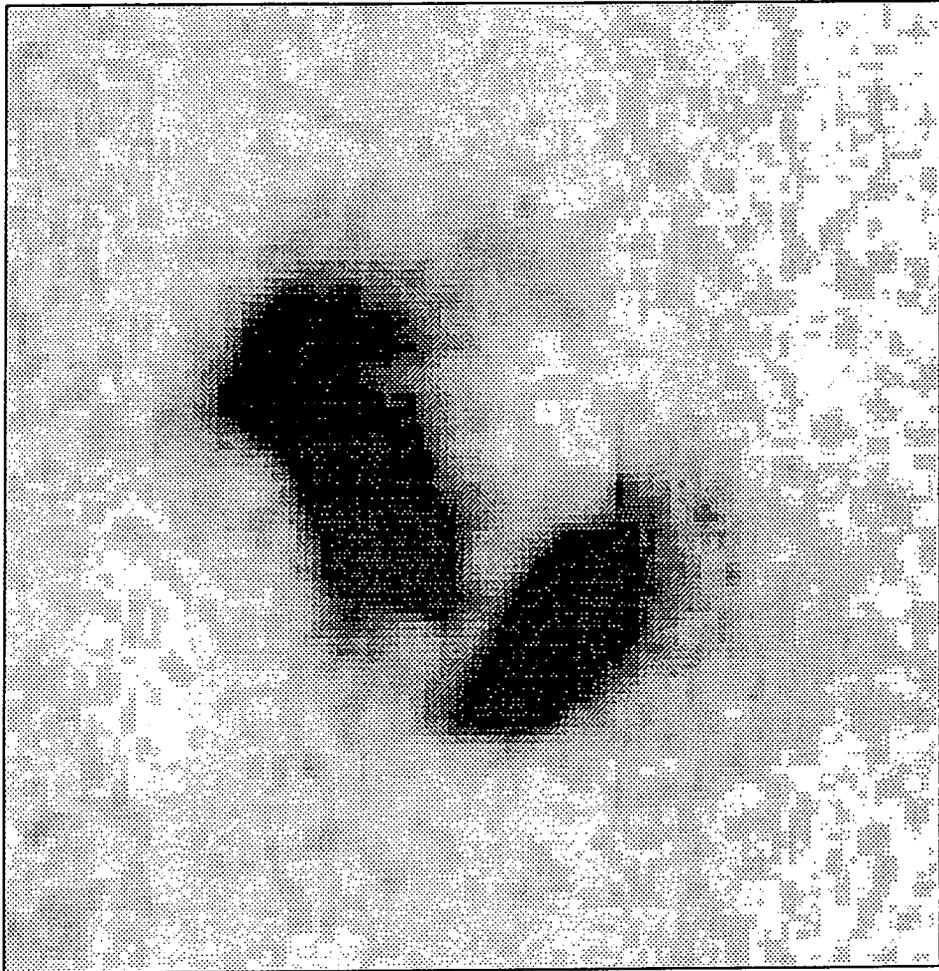
Figure 3.3: Greyscale polarised intensity image of the HH83/Re17 nebulosity. Note the absence of unpolarised features, such as field stars and the jet, which must therefore be seen in emission.

3.4.4   The geometry of the HH83/Re17 system.

From the data presented here it is clear that the nebula is illuminated by an embedded source which cannot be seen directly at optical wavelengths. A well collimated jet, seen by shock-excited emission and consequently unpolarised, emanates from the source. Reipurth (1989) invokes a geometry for HH83/Re17 similar to that of HH34 (Reipurth *et al.* 1986), in which outflow activity from a young stellar object (YSO)—the IRS in this case—creates a cavity in the dark cloud in which it is embedded. Radiation and matter escapes through the cavity to beyond the densest part of the cloud. In the case of HH83/Re17 the YSO is deeply embedded in a molecular cloud clump which prevents it from being observed at optical wavelengths, and it has created a cavity which extends towards us and to the NW of the source. The inner part of the cavity can be seen by light reflected off dust grains on its surface; this is the bright polarised elliptical nebula which is seen in our images. The fainter streak of nebulosity extending further to the NW defines the edge of the outer part of the cavity. No nebulosity is seen close to the position of the YSO implying that here the cavity is obscured by overlying dark cloud material. The apparent clumpy and knotted nature of the brighter nebulosity is due to uneven illumination of the cavity walls, which may themselves have density irregularities.

The elliptical shape of the brightest region of the nebula allows an estimate of the inclination to the line of sight to be made, if we assume that the nebula represents a circular hole in the material surrounding the YSO. The eccentricity of the ellipse defined by the nebula is ~ 0.8, which indicates that the inclination of the axis of the cavity to the plane of the sky is 45–55°. Hence we can see part of the inside of the cavity wall with the jet running in front of it, along the axis of the cavity. The inclination is not sufficient to allow us to see the YSO at the end of the cavity, which is evidence that the opening angle of the cavity is less than 90–110°.

The jet of material ejected by the YSO cools as it travels, until it encounters

the end of the cavity where braking occurs as it interacts with the surrounding cloud material. The velocity of the jet is sufficiently high to cause a shock in the ambient gas, and a crescent of emission is seen—the bow shock detected by Reipurth (1989).

The presence of a counterjet can be inferred from the discovery of a bow shock to the SE of the IRS and colinear with the optical jet (Reipurth 1989), and we might also suppose that a cavity similar to that seen to the NW of the IRS also exists on the other side of it. This second cavity cannot be seen as it is more deeply embedded in the molecular cloud clump, and is also obscured by the same material that hides the YSO from direct view.

The implication of a narrow and well defined jet is that a collimating mechanism operates close to the IRS. One possible mechanism is a small-scale circumstellar disc which only allows matter and radiation to escape along the direction of its axis. Such discs are characteristic of the class of objects with similar geometries to HH83/Re17 (see for example Scarrott *et al.* 1985, Draper *et al.* 1985, Gledhill *et al.* 1986), and whilst there is no direct evidence as yet for a disc in the HH83/Re17 system circumstantial evidence suggests that it is probable. The IR polarisation of the source would therefore be expected to be parallel to the plane of the disc— perpendicular to the jet's propagation axis.

The axis of the HH83/Re17 system (PA=130°) differs from the field direction in the L1641 dark cloud (Vrba *et al.*, 1988) by 20°. It has been suggested (Heyer *et al.* 1987) that the importance of the cloud's magnetic field in determining the orientation of collimated YSO outflows is dependent upon the local ionisation of gas within the cloud, which in turn depends upon the background cosmic ray ionisation flux and/or X-ray emission from any nearby T-Tauri stars. We might therefore infer that in the vicinity of HH83/Re17 the cloud is poorly ionised. There is, however, a large dispersion in the measurements of the field direction made by Vrba *et al.* ($\sigma = 33°$), and, in addition, the measurements were made over an area well inside the L1641 dark cloud; it has already been noted that HH83/Re17

lies outside the main body of the cloud and is associated with a compact clump of molecular material. The magnetic field direction within this clump may be estimated in a speculative fashion by assuming that the clump contracted along the field lines; its minor axis then defines the local magnetic direction. The PA of the minor axis of the clump is 130°—identical to the HH83/Re17 jet direction— so it seems likely that the outflow is parallel to the local magnetic field, which therefore seems to play a major part in protostellar collapse.

3.5 Conclusions

The data presented in this chapter clearly demonstrate the ability of the automated Durham Imaging Polarimeter to measure the polarisation of extended astronomical objects. It has been shown that the HH83/Re17 nebulosity is a reflection nebula illuminated by a source only seen directly at IR and longer wavelengths. The optical illuminator is coincident with an IRAS source (IRAS 05311-0631) which is also assumed to be responsible for producing the jet that is seen crossing the nebula. The jet is seen in emission lines characteristic of HH objects and is unpolarised. It terminates in a bow shock at the end of a cavity in the cloud clump in which it is located, which the young IRS has excavated during the course of energetic outflow activity. The reflection nebula is caused by the reflection of light off the inside of the cavity.

HH83/Re17 seems to share the morphology of other outflow objects with emission line jets, such as HH34, L1551/IRS5 and Haro 6-5. On the basis of these observations we might expect further investigations to reveal the presence of a small-scale circumstellar disc whose plane is perpendicular to the jet propagation axis, and evidence for molecular outflow centred on the IRS.

Chapter 4

GL2591

GL2591 is a luminous compact IRS in a highly obscured region in Cygnus. Within
the vicinity of the source several of the characteristic features of energetic star for-
mation are seen—the protostellar source itself, a bipolar molecular outflow, possi-
ble HH objects, and a nearby knotted and compact optical/IR nebula. Extensive
studies of the region have, however, served to confuse rather than clarify our un-
derstanding of the system; it has been suggested that multiple star formation has
occurred in the region, and that some of the observed phenomena are not related
to the IRS at all.

This chapter investigates the optical nebula using imaging polarimetry as a
probe to see if the IRS is the illuminator of the visible nebulosity. The data are
compared with those of other investigators and an attempt is made to interpret
the polarimetric results in a manner that is consistent with the other observations.

4.1 Summary of previous studies of the GL2591 region

GL2591 was first described by Merrill & Soifer (1974). They obtained an IR
spectrum with clearly defined absorption features, similar to that of the Becklin-
Neugebauer point source in Orion, which led them to predict that the object might
be an H_2O maser source. They ruled out the model of Penston $et\,al.$ (1971) for

similar objects, whereby a supergiant of spectral type F or G is obscured by a dense envelope of dust, and proposed that the dust shell hides either a protostar, a high luminosity star with infrared excess, or a highly evolved object.

Kleinmann and Lebofsky (1975) reported the discovery of a small patch of optical nebulosity slightly to the west of the IRS. On the basis of its red colour and its proximity in the plane of the sky to GL2591 they assumed it to be a reflection nebula, illuminated by the IRS which is obscured from direct view at optical wavelengths. Wendker and Baars (1974) found a faint HII region which they identified with the IRS, and White *et al.* (1975) discovered H_2O maser emission in the same area. These discoveries fuelled theories that the object might represent an evolutionary stage between protostar and compact HII region.

Such theories were rejected, however, when Wynn-Williams *et al.* (1977) found that the HII region and the IRS are two distinct objects, separated by 7″. They proposed that the region contains other newly formed stars, which might be revealed by further study at other wavelengths—a hypothesis supported by Campbell (1984) who found at least four radio sources in the region, none of which is coincident with the IRS or H_2O maser.

Lada *et al.* (1984) showed that the IRS and maser source are spatially separated; they observed a high velocity bipolar CO outflow centred on the IRS and suggested that the maser is a part of the blueshifted outflow. These CO observations were compared with infrared polarimetry by Sato *et al.* (1985) who inferred that the IRS is at the centre of an optically thick disc or torus of dust, and that any observed polarisation of the source itself is due to scattering by this nonspherical envelope. Hodapp (1984) cited the same model as an explanation for the 2.2μ polarisation which he measured at the position of the IRS.

Further observations in the infrared by Forrest and Shure (1986) revealed the presence of a loop or bubble of material, situated with the IRS on its eastern edge. They suggested that this loop is a spherical shell, defining a cavity whose edges are seen by radiation reflected from the IRS—a model supported by the IR

polarisation measurements made by Burns *et al.* (1989), who also suggested that the IRS is surrounded by a dusty disc or torus. Further direct evidence for a circumstellar disc is seen in the data of Yamashita *et al.* (1987).

Hodapp and Yamashita *et al.* measured the 2.2μ polarisation of the nebula, and concluded that it is illuminated by the IRS. A similar conclusion was reached by Lenzen (1987) who mapped the nebula at 1μ, in contrast to the claim of Rolph and Scarrott (1988) who suggested that in the optical waveband a second, previously unseen, source illuminates the nebula. On the basis of J, H and K polarimetry Minchin *et al.* (1990) suggested that in these wavebands the nebula is illuminated by the IRS, but they rejected the spherical shell model of Forrest and Shure in favour of a model involving curved slabs of material, at one time ejected by and now illuminated by the compact protostellar IR source.

4.2 Optical polarimetry of the GL2591 nebula

4.2.1 Observational details

Observations of GL2591 were made in March 1988 using the 2.4m Isaac Newton Telescope on La Palma. The Durham Imaging Polarimeter was used with the coated GEC CCD at the f/15 Cassegrain focus. No filter was used, so that the observations covered a wavelength range from 300 to 1000nm, with peak response at 675nm. The object is, however, very red, so the effective bandpass will be longward of the peak response. 16 frames, totalling 54 minutes of exposure time, were taken in conditions where the seeing was typically $\sim 1''$. The effective seeing of the combined data is $\sim 1.5''$. In addition to these polarimetric images the polarimeter was used in direct imaging mode (i.e. with the Wollaston prism and grid assembly removed from the light path) to make three 300 second exposures in each of the I and R filters.

During the data reduction process the spatially variable background was interpolated over the nebula and subtracted from it in order to remove any contami-

nation from the extensive IC1318 nebulosity, against which GL2591 is seen.

4.2.2   The basic results

Greyscale intensity images of the optical nebulosity are shown in figures 4.1–4.3.

The position of the IRS is marked by a cross—the source itself is not seen directly in any of the wavebands studied here. The nebulosity has two distinct components, both of which appear to have an arc-like shape at low brightness levels, but at higher brightness levels the eastern component is resolved into three knots of intensity. There is also evidence of faint streaks of nebulosity which lie to the west of the IRS and which appear to run in radial lines from it, to a distance of $\sim 50''$.

In figure 4.4 intensity contour and linear polarisation maps of the nebula are shown. The contour map clearly shows the two components of nebulosity and the sharply defined dark area between them. The polarisation map shows relatively low levels of polarisation ($\lesssim 10\%$) and a complicated pattern of vector orientations. The western region of nebulosity shows a roughly circular polarisation pattern which has its centre in the obscured lane, but the eastern component has a more complex pattern with no obvious centre.

4.2.3   Effects of the ISM

GL2591 is in the Galactic plane ($l = 79°$, $b = 1°$) at a distance of 1–3 kpc, and might therefore be expected to show the effects of polarisation caused by selective extinction by aligned dust grains within the intervening ISM, in addition to polarisation intrinsic to the nebula itself and its dark cloud. The polarisation measurements of stars by Mathewson and Ford (1970) have a random pattern of orientations in the direction of and at the distance of GL2591. A more detailed study of the orientations of polarisation of stars in the region of GL2591 led Dyck and Lonsdale (1979) to conclude that the orientation of the Galactic magnetic field is poorly defined in this direction. Synthesised aperture polarimetry on the field
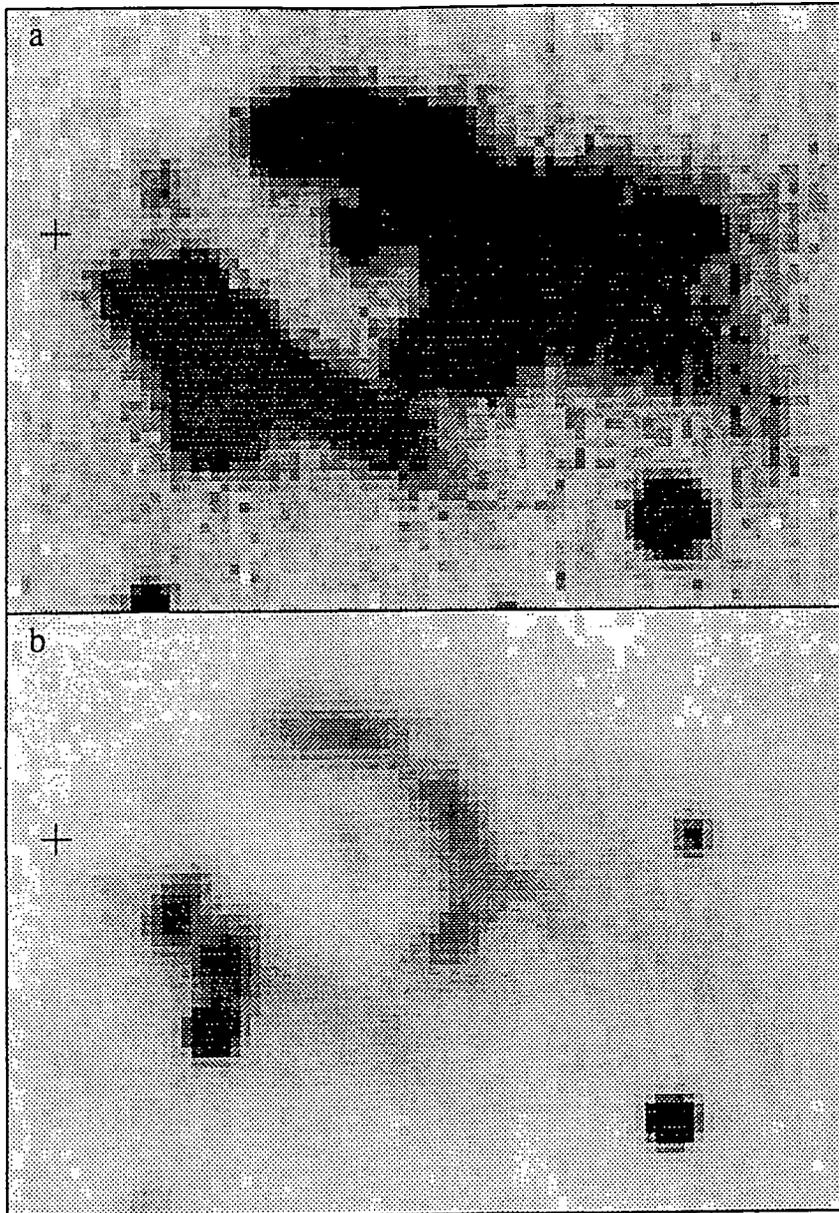
Figure 4.1: Greyscale intensity images of the optical nebulosity close to GL2591 (no filter) displaying the structures at low (a) and high (b) brightness levels. The position of the IR source is indicated.
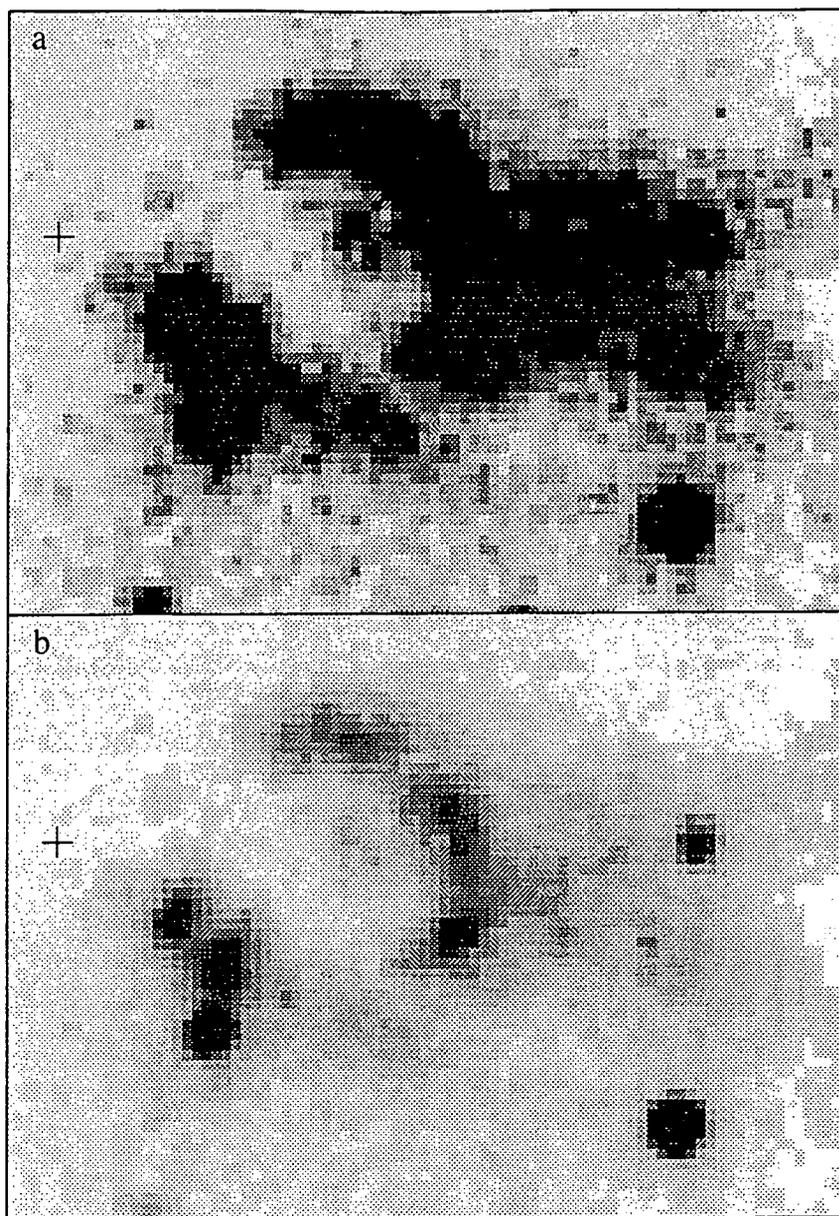
Figure 4.2: Greyscale intensity images of the optical nebulosity close to GL2591 in the R waveband displaying the structures at low (a) and high (b) brightness levels. The position of the IR source is indicated.
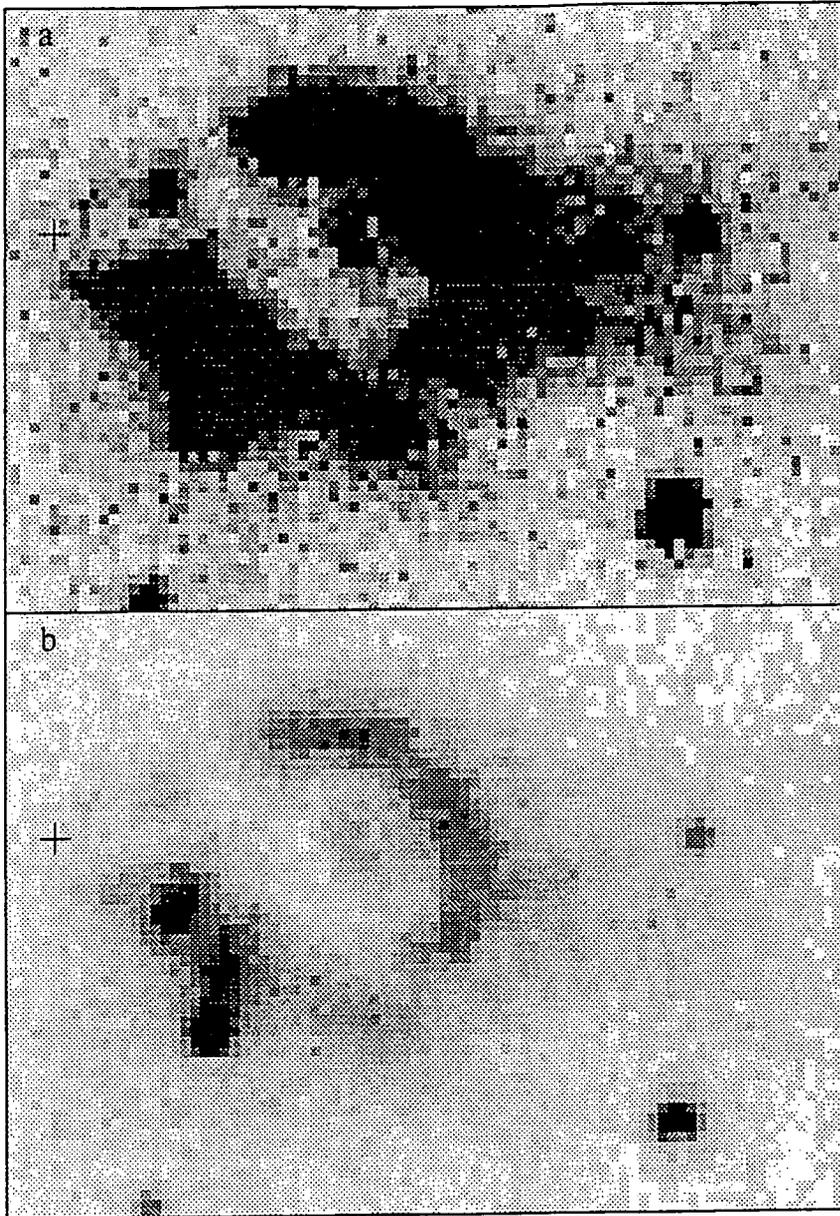
Figure 4.3: Greyscale intensity images of the optical nebulosity close to GL2591 in the I waveband displaying the structures at low (a) and high (b) brightness levels. The position of the IR source is indicated.
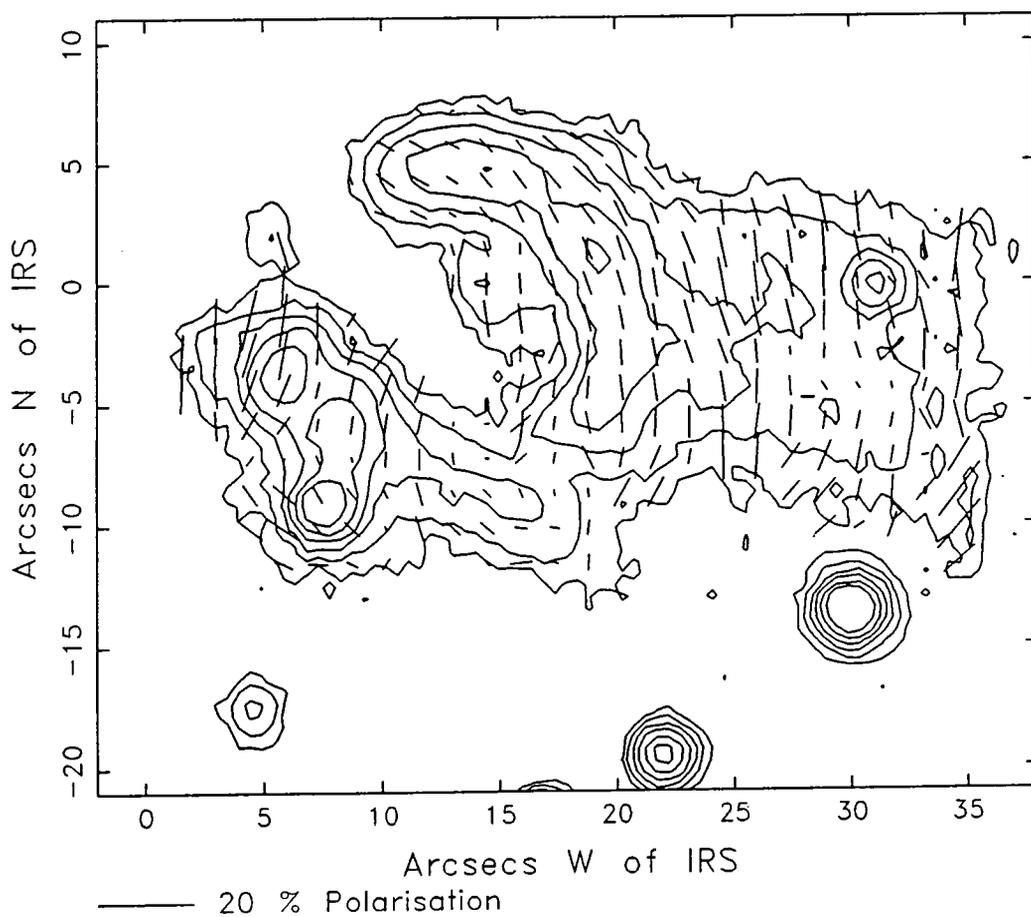
Figure 4.4: Intensity contour and linear polarisation maps of the GL2591 nebulosity. No filter was used for these measurements. The origin of the coordinate system is the position of GL2591 IRS.

stars in our images shows no preferred position angle, and confirms the result of Dyck and Lonsdale. Furthermore, the subtraction of a small amount ($\sim 2\%$) of polarisation at a position angle parallel with the Galactic plane—an estimate of the likely polarisation induced by interstellar absorption—makes little difference to the polarisation map, particularly in the bright arcuate lobes. It therefore seems reasonable to assume that the effect of interstellar extinction on the measured polarisation is negligible.

4.2.4 Extinction within the dark cloud

Although the possibility of polarisation induced by dichroic extinction by aligned grains in the ISM has been eliminated, it cannot simply be assumed that all of the polarisation measured at optical wavelengths is intrinsic to the nebula and is caused by scattering of light from a source which is apparently obscured from direct view. The GL2591 complex resides in a molecular cloud which causes high levels of extinction, (~ 30 visual magnitudes, Hough *et al.* 1989) and which is also capable of causing polarisation effects that might alter the pattern of vector orientations as measured by an observer outside the cloud. Chaisson and Vrba (1978) demonstrated that dense molecular clouds associated with HII regions are able to support strong ($\lesssim 10\mu G$) uniform magnetic fields which may have been "frozen" into into the clouds when they collapsed. If this is the case then the fields would be able to align nonspherical dust grains which would have a polarising effect on light passing through any part of the cloud.

It is therefore necessary to examine the data for evidence of polarisation due to a magnetic field within the cloud in which the system is found, and to remove such effects in order to look at the polarisation intrinsic to the nebula. Dyck and Lonsdale (1979) made the assumption that the position angle of the IR polarisation of sources within molecular clouds is an indication of the field direction, but this is not necessarily the case for GL2591; Heckert and Zeilik (1981) showed that sources with a bipolar molecular outflow tend to have IR polarisations perpendicular to the

probable field direction. They attributed this polarisation to a scattering process in a nonspherical dust cloud around the source as proposed by Elsässer and Staude (1978), and it is now known that in the case of GL2591 the IRS is surrounded by a dense large-scale disc or torus of material (Yamashita *et al.*, 1987). A smaller circumstellar disc, as required by Elsässer and Staude's model, cannot therefore be ruled out.

A test for the effects of extinction within the cloud would be to measure the polarisation of any stars embedded in it. In the direction of Gl2591 there is a star-like feature within the dark cloud which shows considerable polarisation. The star is situated 7.5″ west and 9″ south of the IRS, and is clearly resolved in the intensity contour map of figure 4.4 and the greyscale images of figures 4.1–4.3, on the southern edge of the eastern arc of nebulosity. Although it might be argued that this is a foreground star and not related to the GL2591 system at all, the polarisation data suggest otherwise. The polarisation measured within a 6″ aperture centred on the star is 3.9 ± 1.0 per cent at PA$= 40 \pm 7°$—much higher than is measured for any other star in the field. Figure 4.5 shows a greyscale polarised intensity image of the GL2591 region in which the star to the SW of the IRS can be clearly seen, in contrast to the unpolarised foreground stars which are notably absent. This supports the idea that the polarising mechanism is local to the star, and implies that the star is embedded in the nearer edge of the molecular cloud. The orientation of the polarisation of this feature is parallel to the Galactic plane—the preferred direction for a magnetic field "frozen" into a condensing molecular cloud—and provides further circumstantial evidence that the object is a relatively blue star embedded in the cloud and polarised by extinction within the cloud itself.

It does not seem unreasonable, from the evidence presented here, to adopt the hypothesis that the nebula is seen through a part of the dark cloud, and that extinction within the cloud is responsible for some of the measured polarisation. The level of polarisation induced by the cloud can be estimated from that measured at the position of the star embedded within it—if we assume that this value is
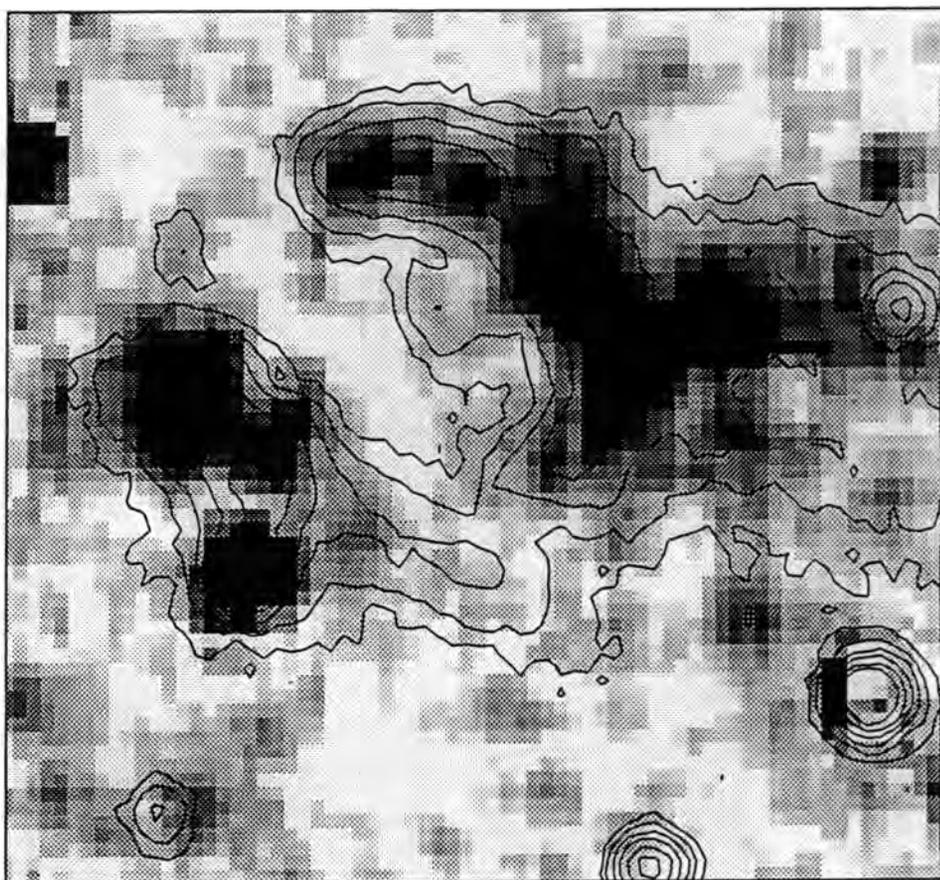
Figure 4.5: Greyscale polarised intensity image of the GL2591 nebula, overlaid with an intensity contour map of the region. Note the absence of the unpolarised field stars.

constant over the relatively small spatial extent of the nebula then a "corrected" polarisation map such as that shown in figure 4.6 can be made. To produce this figure a polarisation of 4% at a PA of 40° has been subtracted from the measured polarisation, which has considerably simplified the pattern of vectors. The most straightforward interpretation of the corrected map is that GL2591 IRS is the major illuminator in the region, and that at least one other optical source is present as well—probably the bright star to the SW of the IRS. Two reflection processes are therefore occurring in the nebular region at optical wavelengths; in some areas (depending on the degree of illumination by the two sources) reflection from the star dominates, whilst in others reflection of light from the IRS is dominant. At NIR wavelengths the star is faint, and the whole of the nebula is likely to be seen by radiation reflected from the IRS.

4.2.5 Comparison with other polarisation measurements

Various other investigators have measured the polarisation of GL2591 and the surrounding region, most notably in the IR. Hodapp measured the linear polarisation at four positions in the nebula in the K waveband. Our data have been integrated to the same centres and aperture size (12″) for comparison, but significant polarisation was only measured in the aperture centred on the source itself. Here the polarisation was found to be 13.0 ± 4.5 per cent at PA= 176 ± 10°, which is in agreement with Hodapp's value of 10% at PA= 169°, and also with the results of Hough *et al.* who obtained a value of 8.13 ± 0.5 per cent at 170° in the J (1.3μ) waveband. The reason that no significant polarisation was measured in the other apertures is clear from figure 4.7, which shows the aperture positions in relation to the optical nebulosity; most of the apertures include a large area with little or no signal, so polarisation measurements are not possible. The aperture offset 20″ west of the IRS includes so much of the nebulosity that the polarisation varies across it, so that the integrated polarisation measurement is no higher than the measured errors. A 6 arcsecond aperture at this position yields 4.9 ± 1.4 per cent

Figure 4.6: A "corrected" map of the polarisation of the GL2591 nebula after the contribution of the dark cloud has been subtracted from the data. The vectors are now more nearly centrosymmetric about the IRS, which is at the origin of the coordinate system.
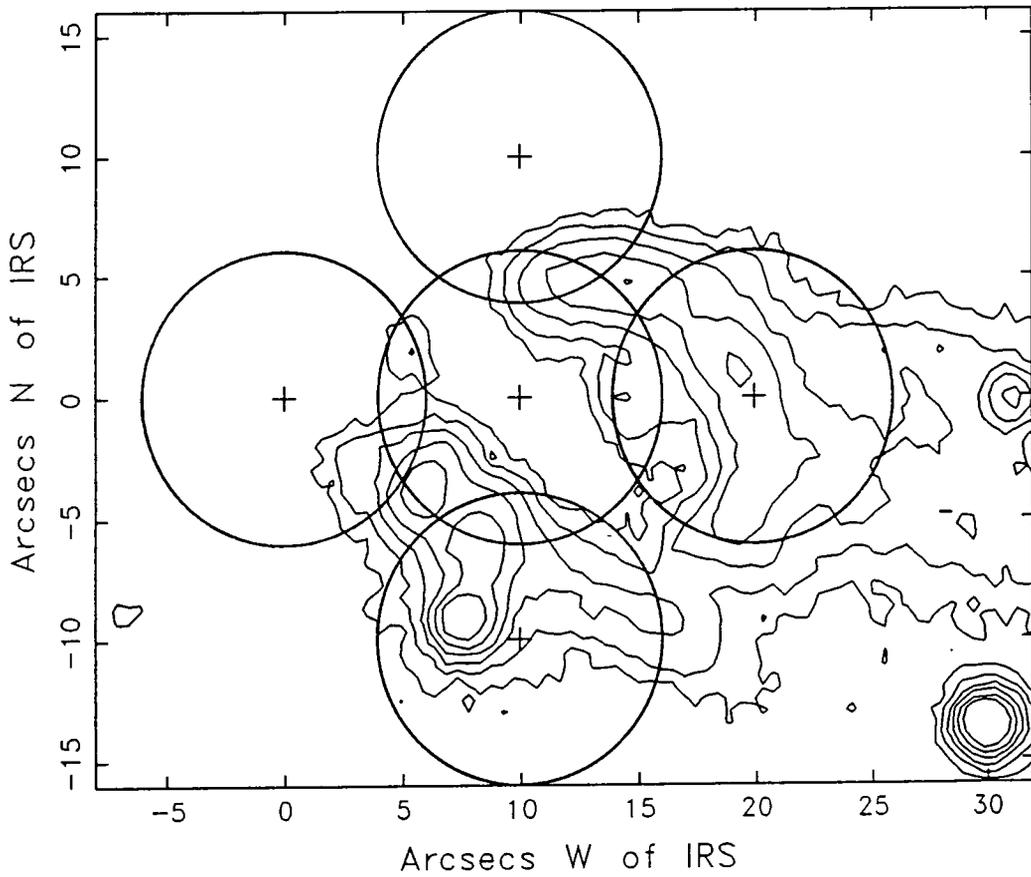
Figure 4.7: An intensity contour map of the GL2591 nebulosity, showing the positions of Hodapp's 12″ apertures.

at PA= 197 ± 8°. Although the level of polarisation is lower than that measured by Hodapp at this position the orientation is similar.

Hodapp's measurements are combined with the data of Yamashita *et al.* in their K band polarisation map of a 2 × 1 arcminute area around Gl2591. They found faint nebulosity to the east of the IRS and were able to make polarisation measurements in this region. The vector orientations form a centrosymmetric pattern around the IRS, with higher levels of polarisation in the east and west, and null points to the north and south of the source. The data presented here show no evidence of optical nebulosity to the east of the IRS.

Lenzen mapped the linear polarisation of the Gl2591 nebula at 1μ, and concluded that 'all polarisation vectors point towards the position of the IR source'. Since the object is so red the effective bandpass of our observations should be close to Lenzen's and indeed the maps are similar. Lenzen, however, made no correction either for interstellar polarisation or for the effects of extinction within the dark cloud, and the most convincing area of his map is that closest to the IRS; the northern half of the eastern patch of nebulosity. This is the brightest and most highly polarised part of the nebula, and therefore the region in which absorption by the dark cloud will have the least noticeable effect—the pattern here is similar to that seen in figure 4.6.

Lenzen's results were not confirmed by the optical polarimetry of Rolph and Scarrott, who proposed that a second source is situated between the two regions of nebulosity and is responsible for illuminating the western lobe and the southern half of the eastern lobe. This conclusion was drawn from the fact that their proposed source lies at the geometric centre of the arc formed by the western nebulosity, and is at the centre of a smooth centrosymmetric pattern of polarisation vectors. Although a small correction was made for possible effects of interstellar absorption, no correction was made for any contribution to the polarisation from the dark cloud. If such a correction had been made their polarisation map would probably look very similar to that in figure 4.6, except for a high degree of

smoothing caused by the 2.5″ seeing.

Minchin *et al.* produced a model for the GL2591 nebula based on the linear polarisation mapped in the J, H and K wavebands. The J intensity contour map is morphologically similar to the optical map in figure 4.4, showing a bright arc of 15″ diameter with the IRS on its eastern edge. At longer wavelengths a smaller arc or loop is seen, comparable with the "bubble" seen by Forrest and Shure. In all of the polarisation maps produced by Minchin *et al.* the vectors are centrosymmetric about the IRS, the degree of polarisation being as much as 20% in some areas. The source polarisation, integrated within a 6 arcsecond aperture, was measured to be 9.7 ± 0.3 per cent at PA= 171 ± 1° in the K waveband, rising to 23.7 ± 1.4 per cent at 171 ± 1° in J. The level of polarisation in the J waveband is much higher than that measured by Hough *et al.*, and is not confirmed by our optical data. Since the source is not seen in the waveband studied here, it is probable that any optical polarisation measured at the IRS position arises as a result of part of the reflection nebulosity being included in the aperture.

If the dark cloud does have a polarising effect in the optical waveband we might expect to see a similar, if smaller, effect in the NIR. The H and J polarisation maps of Minchin *et al.* show that the pattern of vectors across the star to the SW of the IRS is not consistent with the centrosymmetric pattern across the rest of the nebula. These authors did not comment on this, nor did they investigate the possible effects of the dark cloud. Had they subtracted the polarisation measured at the position of the star from that measured over the rest of the nebulosity the change in the maps might hardly have been noticeable, since the polarisation of the nebula in the IR is high, but it would have been a valuable aid in interpreting the optical data. There is however no reason to believe that the position of the illuminating source inferred from such a "corrected" map would differ significantly from the IRS position.

4.2.6 Interpretation of results

Figure 4.8 shows a map of the polarised intensity in the GL2591 nebula, after a correction of 4% at PA= 40° for the dark cloud effect. The vectors have been rotated by 90°, so that for a simple reflection nebula they should point to the illuminating source. The majority of the vectors form a radial pattern around a point within 5″ of the IRS, which must therefore be assumed to be the illuminator of most of the nebula.

There are however two regions where the vectors do not point towards the IRS; these do not arise as a result of the polarisation correction, since they can also be seen in the uncorrected map of figure 4.4, one just to the south of the embedded star SW of the IRS, and the other in the most northerly part of the nebula. These areas are clearly illuminated by a source other than the IRS, at least at optical wavelengths. One candidate for the illuminator could be the obscured source proposed by Rolph and Scarrott, in the centre of the obscuring lane.

The star to the SW of the IRS, which Lenzen assumes is an unrelated foreground star, could, on the basis of the polarisation vectors shown in figure 4.8, be responsible for illuminating those parts of the nebula that do not appear to be illuminated by the IRS, particularly if it is slightly more embedded in the dark cloud so that the cloud's contribution to the nebular polarisation has been over-compensated for. At longer wavelengths where the star is fainter the nebula would be expected to be illuminated entirely by the IRS, which is of course much brighter in the IR, and the maps of Lenzen and Minchin *et al.* show that this is indeed the case. This visible source is therefore identified with the source proposed by Rolph and Scarrott. The discrepancy in position arises from the large correction for dichroic extinction which the high spatial resolution data presented here show is necessary. The data of Rolph and Scarrott are affected by poor seeing and a large pixel size which caused the star discussed here to be unresolved; this is undoubtedly a factor leading to the slightly different interpretation which they made.
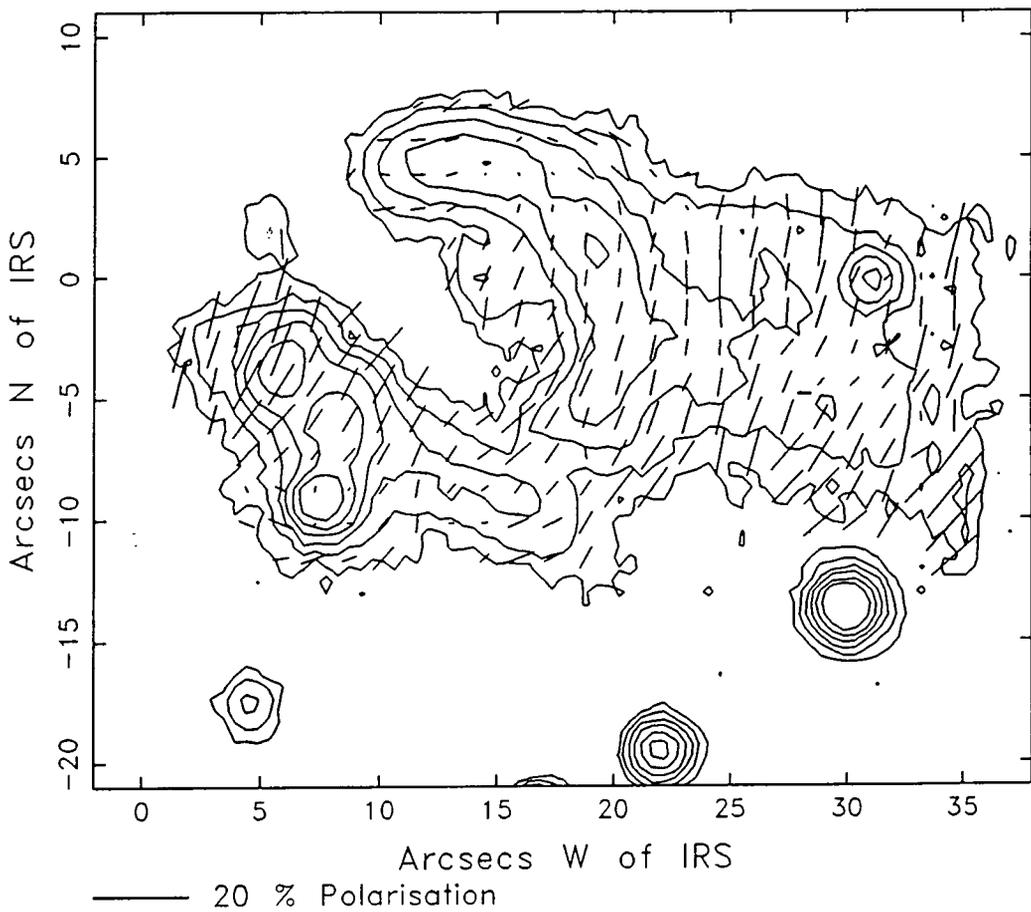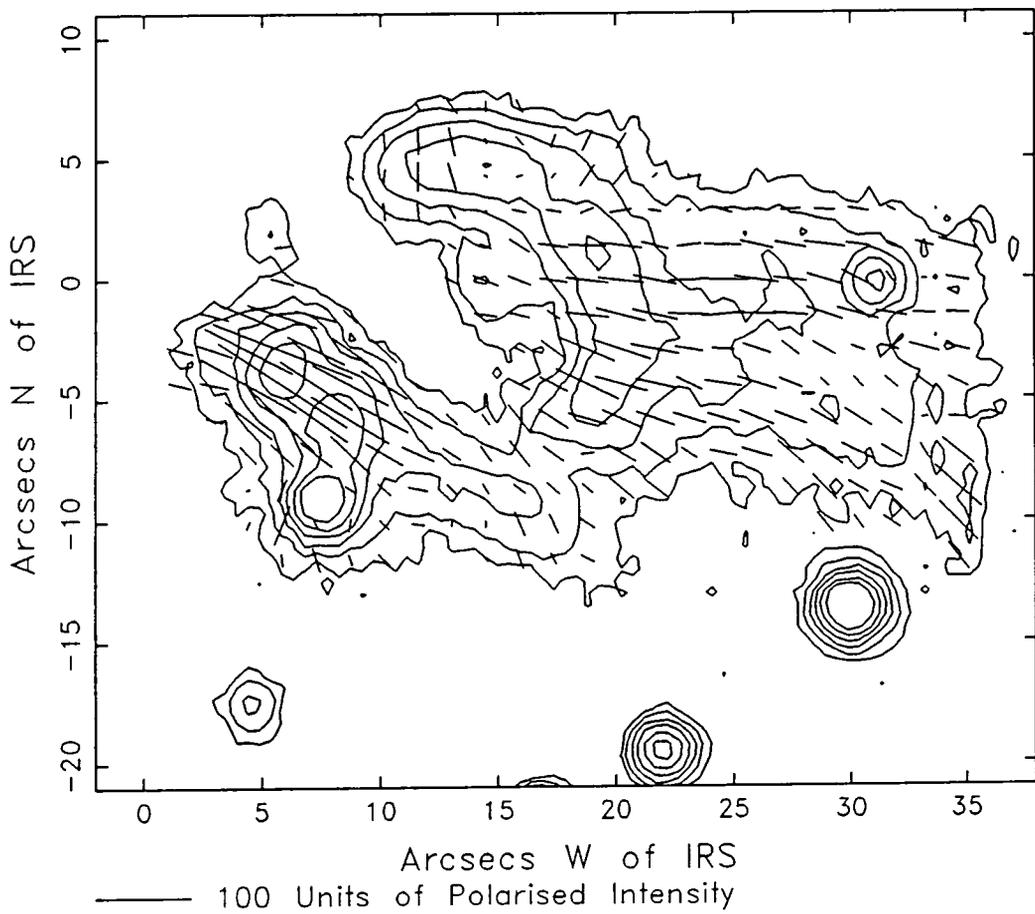
Figure 4.8: A "corrected" map of the polarised intensity of the GL2591 nebula after the contribution of the dark cloud has been subtracted from the data. The vectors have been rotated by 90° so that for a simple reflection nebula they should form a radial pattern around the illuminating source.

Since the IRS cannot be seen at optical wavelengths, yet illuminates the visible reflection nebulosity, it must be much more highly obscured along the line of sight than the nebula is. The implication of this additional obscuration is that the IRS is surrounded by an anisotropic cloud of optically thick material which allows more light to escape in the direction of the nebula than in other directions. A spherical shell with a hole in it is one such distribution, but the observations of Yamashita *et al.* show that a more likely scenario is a dense circumstellar disc which allows radiation to escape along its axes.

The polarisation of the IR source itself measured at optical wavelengths ($13.0 \pm 4.0\%$ at $176 \pm 10°$) must be attributed to the material surrounding it, since the source cannot be seen. It is likely that the aperture used includes some of the nearby reflection nebulosity, and it is the polarisation of this that is being measured. At NIR wavelengths, however, the source can be seen directly, and its polarisation must be caused by one of two effects: either selective absorption is occurring inside the optically thick disc, or it is produced by light escaping along the axes of a small-scale ($< 3''$) anisotropic dust cloud around the IRS and being scattered towards the observer. It is possible that a combination of the two effects is occurring, but in both cases the polarisation would be expected to be parallel with the major axis of the disc projected on to the plane of the sky. The orientation of the large scale disc as mapped in CS by Yamashita *et al.* shows that this is indeed the case.

At much longer wavelengths ($\gtrsim 10\mu$) the possibility of scattering being the primary polarising mechanism can be rejected. The wavelength of maximum polarisation is slightly longer than that for maximum extinction (Aitken *et al.* 1988) indicating that preferential absorption is occurring. Aitken *et al.* argue, on the basis of circular polarisation measurements (Lonsdale *et al.* 1980, Serkowski and Reike 1973) that dichroic absorption alone is responsible for the source polarisation at all wavelengths longward of 2.2μ. High resolution polarisation maps in the NIR, such as those produced by Minchin *et al.* show that in this region of the spec-

trum there appear to be two competing polarising mechanisms which fully cancel in specific regions to produce null points on either side of the source and colinear with it. Bastien and Menard (1988) attempted to explain similar observations by invoking a double-scattering model, but this cannot explain the polarisation of the source when it is seen directly (in the IR in this case). We therefore deduce that the NIR polarisation measured at the source position is due to a combination of the effects of scattering and preferential absorption by aligned grains within the disc.

4.3 Discussion

As well as the optical/IR nebulosity and the compact IRS itself, there are a number of other features observed in the region which any modelling of the system must allow for, if not account for. These include the H_2O maser source discovered by Bade *et al.*, and found by Lada *et al.* not to be coincident with the IRS ($\sim 4''$ to the NE of the IRS). Lada *et al.* also showed that an extended high velocity bipolar outflow is centred on the IRS; the blue-shifted part of the outflow coincides with the nebular regions. At least four HII regions are known to lie close to GL2591; none of these is coincident with the IRS. In addition, the presence of two HH objects just to the west of the nebula has been suggested by Tom Ray (private communication).

4.3.1 The illuminating sources

The polarisation map of figure 4.6 clearly identifies the IRS as the primary illuminating source of the GL2591 system at optical wavelengths, with the star to the SW of it being responsible for illuminating some small areas of nebulosity. Comparisons of optical and NIR images show that the two stars are apparently very different, and they will be discussed individually here.

The IRS

The IRS is without doubt the only illuminator of the GL2591 nebulosity at IR and NIR wavelengths, and the main illuminator at optical wavelengths. It is seen within a molecular disc thought to be contracting towards it (Yamashita *et al.*), and is at the centre of a bipolar molecular outflow (Lada *et al.*). These observations place it in the third of the four stages of star formation described by Shu *et al.* (1987), where both infall and outflow are occurring. On the basis of this information alone, then, we might infer that the source is at an evolutionary phase intermediate between an accreting protostar and a fully revealed pre-MS star. Lada *et al.* show that the IRS consists of a compact ($\sim 0.06''$) cocoon of dust around a stellar source which heats it to ~ 800K. The dust is responsible for emitting all of the observed IR radiation. Such a source, at a distance of 2kpc, would have a total luminosity of $\sim 10^5 L_\odot$ and would be extinguished by 40–50 visual magnitudes. The flux measurements and extinction estimates of Lada *et al.* are consistent with an O7.5 ZAMS star, showing that the object is of high mass and has evolved directly onto the MS, reaching the H-burning phase with no pre-MS stellar evolution. During the subsequent MS evolution both inflow and outflow processes would be expected to cease, and the circumstellar dust shell would dissipate to reveal an O star with a flattened disc surrounding it.

The second illuminator

Since it has not been well studied and photometric or spectroscopic information is not currently available, little is known about the other exciting source in the region. We can infer from its presence in the optical data, and its absence in K band images, that it is a more highly evolved star than the IRS, having lost the dust that once surrounded it as it formed. From its degree of polarisation ($\sim 4\%$) we estimate that the extinction to it is 3–4 visual magnitudes. It is possible that this star reached the MS shortly before the IRS, and is an example of another region within the molecular cloud that has undergone collapse and

star formation. The dark cloud probably hides several other systems at various stages in the star formation process. It is likely that this second illuminator is not physically associated with GL2591, but is able to illuminate it simply on account of its proximity to the system.

4.3.2 The circumstellar disc

The CS mapping of Yamashita *et al.* shows that the large scale anisotropic distribution of optically thick material surrounding the protostellar source is undoubtedly in the form of a disc. It is assumed that the disc is responsible for collimating the molecular outflow, and for obscuring the IRS from direct view at shorter wavelengths, whilst allowing radiation to escape along its axis in the direction of the reflection nebulosity. The longer wavelength source polarisation, which cannot be attributed to scattering alone, suggests that there is an ordered magnetic field in the plane of the disc, of sufficient strength to cause alignment of nonspherical dust grains.

The optical reflection nebula is seen only in the region of the blue-shifted molecular outflow; this is evidence that the disc is tilted with its axis out of the plane of the sky, so that it obscures any nebulosity which might lie in the redshifted outflow region. The angle of the nebulosity subtended by the IRS is approximately 90°. Assuming, then, that optical radiation escaping along the axis of the disc is confined to a cone of 90° opening angle (projected onto the plane of the sky), an upper limit of 45° can be put on the angle which the axis of the disc makes with the plane of the sky. The actual angle must be close to this value since nebulosity can be seen very near to the source (within $\sim 5''$). Yamashita *et al.* estimate the dimensions of the disc to be $80'' \times 50''$ in the plane of the sky, which puts an upper limit of 38° on the inclination angle—consistent with the previous estimate. This also eliminates the possibility of seeing any optical nebulosity associated with the redshifted molecular outflow, to a distance of at least $25''$ to the east of the IRS.

4.3.3   The reflection nebulosity

In the previous section it was shown that the inclination of the plane of the circumstellar disc to the line of sight is less than, but close to, 45°, and that radiation escaping along the axes of the disc is confined to a cone of opening angle $\leq 90°$. If we assume that the stellar wind from the IRS, collimated by the molecular disc, excavates a cavity in the less dense cloud material, then at optical wavelengths we might expect to see light from the IRS reflected off the the walls of the cavity, producing a smooth U-shaped nebula, slightly brighter at its edges than in the centre. This is clearly not the case—the nebula is clumpy and of arcuate shape.

Several models have been proposed for the three-dimensional distribution of the nebular material in order to explain the apparent clumpiness. Forrest and Shure suggested that the stellar wind from the IRS blows the molecular cloud material into the spherical bubble which is clearly seen in the K waveband, but the larger arcs of nebulosity seen at shorter wavelengths cannot be easily explained by this model. Minchin *et al.* argued that the material lies in concave slabs inclined by 50°–55° to the plane of the sky. These sheets of material would consist of matter that has been ejected by the YSO itself in discrete outbursts, and would expand as they move away from the protostar. Complex density gradients are required by this model if the observed clumps of nebulosity are to be explained, and Minchin *et al.* give no indication of how such gradients might arise. There is, however, a relatively simple process which could cause the density at the edges of the slabs to be greater than in the centre, as the model requires. A short, discrete period of mass ejection would send a "puff" of material along the direction of the disc's axis. This material would expand as it moves away from the star, remaining within the 90° outflow cone defined by the disc. More interestingly, it would be possible for the ejected matter to interact with the stationary dark cloud material surrounding the IRS in such a way as to form a vortex ring, similar to a smoke ring in air. As a result, for each outburst of the protostar we might expect to see an expanding ring with an increased density of material around its outer edge; projected onto the

plane of the sky such rings would appear to be ellipses of increasing size moving away from the IRS.

The contour map of figure 4.4 shows that the western arc is approximately elliptical and could be part of a ring of material ejected by the IRS. The eastern nebulosity does not lie on the same ellipse and must be attributed to a second short outburst of matter. Although this is a simple and appealing model to explain the distribution of the observed reflection phenomena, the polarisation data show that it is an inaccurate representation of the system. The eastern nebulosity is rather brighter than the western arc; this could be explained if it lay towards the front surface of the outflow cone and is seen by forward scattering, with the western nebulosity lying towards the rear of the cone and seen by back-scattered light. The scattering angles would, however, be $\sim 10°$ and $\sim 110°$ respectively, and the western region would therefore be expected to be much more highly polarised than its eastern counterpart, irrespective of the nature of the scattering particles. This is not observed—the nebula is more highly polarised in the east, if anywhere—so it can be inferred that the two areas have approximately the same line of sight to the IRS, and are not in the form of vortex rings as described above. The difference in intensity must be due to illumination effects, such that less light reaches the western arc. It could be that the eastern nebulosity itself is responsible in part for obscuring the IRS from the western region. It seems likely that both regions of nebulosity are seen by forward scattering, since if they lay towards the back of the outflow cone the scattering angle would be close to 90° and higher level of polarisation would be expected. They could be the results of two discrete outbursts of the IRS, or just high density regions in the surrounding dusty material that have not yet been cleared away by the outflow activity.

Lenzen remarked on a jet-like feature to the SW of the IRS, colinear with it, the H_2O maser and two HII regions. This feature is visible in the optical data presented here, particularly in the total intensity image of figure 4.1. It appears to run roughly along the southern edge of the outflow cone, but there is no noticeable

drop in polarisation that might be expected if it were an emission-line feature. If it were a jet then it would require the presence of some small-scale collimating feature close to the IRS whose axis is inclined to the axis of the molecular outflow and the cone containing the nebulosity. A more likely suggestion is that the "jet" is simply caused by ablation of matter from the eastern condensation by the stellar wind. Similarly the radial streaks seen in the direct R and I images (figures 4.2 and 4.3) are probably caused by the stellar wind eroding material from the western arc and carrying it away from the IRS.

4.3.4 Hɪɪ regions

Despite the proximity of at least four radio sources to GL2591 (Campbell, 1984) no evidence of emission from ionised gas has been found coincident with the IRS. Thompson and Tokunaga (1979) proposed a model whereby the dust cloud around the IRS is beginning to break up. UV photons escaping through holes in the cloud can then ionise the surrounding gas to produce Hɪɪ regions. The brightest of the four radio sources so far discovered is consistent with an optically thin photoionised region, and is coincident with part of the eastern nebulosity which could therefore be illuminated by optical photons escaping through the same hole in the dust cloud, lending credence to the model. The strong UV flux produced by a ZAMS O star would be more highly collimated by the circumstellar disc than would optical radiation, so the Hɪɪ region would be expected to be smaller than the optical nebula, and this is in fact the case (the Hɪɪ region is approximately 4″ across). Campbell, however, showed that this cannot be the case for the three fainter radio sources, and argued that although they could be clumps of matter ejected by the IRS and subsequently ionised by UV radiation escaping through the resulting evacuated path from the star, an explanation more consistent with current observations is that they are part of a cluster of totally independent Hɪɪ regions, each containing its own ionising source. Clumps of matter illuminated by UV photons from the IRS should also be visible at optical wavelengths but

none are seen, which adds weight to the second of Campbell's models. Currently, however, no IR sources have been seen at the positions of the radio sources either. The estimates of the luminosities of the sources and the extinction to them by Campbell led her to suggest that if they were independent sources then mid- to far-IR photons would escape, but no surveys of sufficiently high limiting magnitude and resolution have been carried out to be able to confirm this.

It is not clear then, whether or not the radio sources are physically part of the GL2591 system or not. On the basis of Campbell's calculations it seems unlikely that the three fainter sources are related to the IRS, and if they are self-illuminating compact HII regions then it raises the possibility that further, as yet undiscovered, sources exist in the same region of sky. Campbell's survey covered only a small area around the IRS; a more extensive survey might reveal further HII regions whose exciting sources can be accurately located.

4.3.5 The molecular outflow

The CO outflow data presented by Lada *et al.* showed that the directions of the red- and blue-shifted outflows are not exactly opposite, with the red flow extending to the northeast and the blue one to the west. The higher resolution observations of Yamashita *et al.*, however, show that on a smaller scale ($\sim 100''$) the outflow directions are separated by 180° in the E–W direction, with the centre 20″ north of the IRS.

The geometric configuration of the outflow phenomena, then, is that of the prototypical star-forming region, with a bipolar outflow orientated with its axis perpendicular to the plane of a circumstellar disc. Although the centre of the outflow has been found to be offset from the IRS position, the disparity is barely more than the observers' beamwidth (17″), and there is no reason to believe that the source of the outflow is not close to the surface of the protostar.

It has been suggested that the molecular outflow phase marks the end of star formation and the beginning of stellar evolution (Lada 1985). This would be

consistent with the view that GL2591 is a ZAMS star emerging from its dusty shell.

4.3.6 The H_2O maser

The velocities of the H_2O maser source (-21.6kms^{-1} and -23.6kms^{-1}) determined by Wynn-Williams *et al.* led Lada *et al.* to identify it with the blue-shifted lobe of the molecular outflow, once it was realised that it is not coincident with the IRS. It is possible that an intense stellar wind could accelerate a maser knot to such high velocities although in this case we might expect it to be to the west of the IRS as this is the preferred blue-shifted outflow direction. Since the disc is tilted by as much as 45°, however, this possibility cannot be rejected and must be retained as the most probable explanation until further observations can resolve the matter.

4.3.7 HH objects

Herbig-Haro objects are common features in regions of energetic star formation and might be expected to be present in the GL2591 system. Since they are probably shock excited emission nebulae ejected by T-Tauri like stars it is likely that they would be seen in the blue-shifted molecular outflow region, within the emission cone defined by the disc.

It has been suggested by Ray that there are two candidates for HH objects in the specified region—deep SII plates show compact clumps of nebulosity just to the west of the western arc, which are not visible in a continuum image. The positions of these two clumps are indicated in figure 4.9, which has been obtained by taking the ratio of the direct R and I frames. HH objects should be much brighter in R than in I and would show up clearly in this image. There is evidence for a small knot of nebulosity which appears to be slightly brighter in the R waveband, just to the north of the bright field star. This corresponds to the position of one of Ray's proposed HH knots. The other proposed knot lies just to the east of this; there is no evidence for it in figure 4.9. At the position of the knot to the north
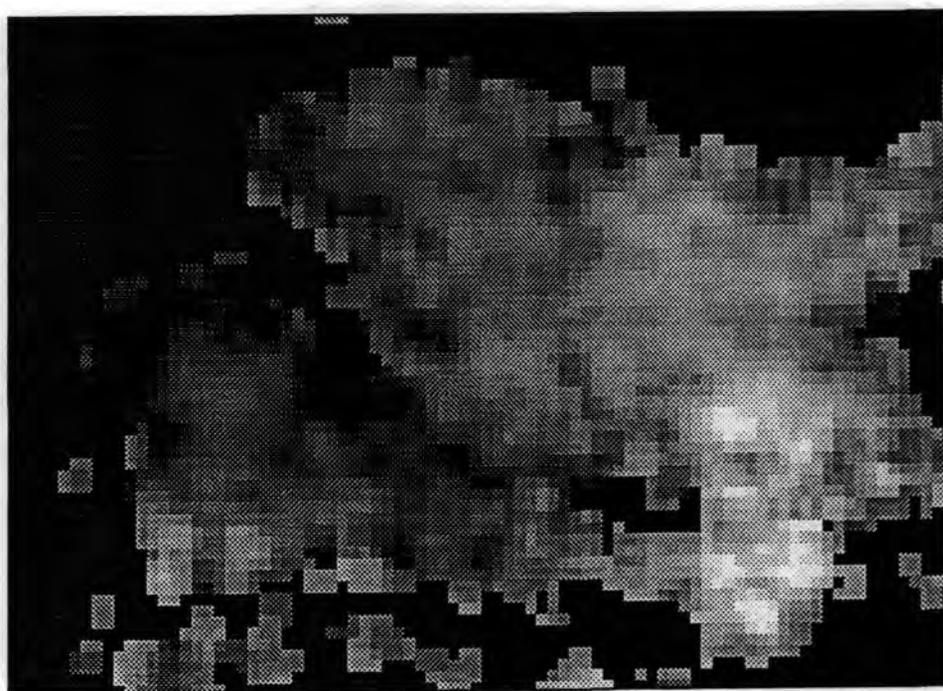
Figure 4.9: Colour diagram of the GL2591 nebula obtained by taking a ratio of the R and I images. White corresponds to areas which are brighter in the R waveband.

of the bright star the polarised intensity image of figure 4.5 shows no significant minimum, showing that if there is an emission feature here it is weak in comparison with the bright reflection nebula.

4.4 Concluding remarks

From the evidence amassed here it is apparent that the GL2591 complex is a small region within a molecular cloud that has undergone collapse and accretion, and is nearing the end the star-forming phase. The optical data presented here provide further evidence for an obscuring circumstellar disc, and show that this is inclined such that light escaping along the axes of the disc can illuminate nebulosity which is seen by reflection.

Figure 4.10 shows a schematic diagram of the system, with a ZAMS O star inside a cloud of IR-emitting dust. The cloud is breaking up and lies at the centre of a large optically thick disc which confines short wavelength photons to a cone centred on the disc's axis; within this cone ejecta from the source are illuminated and are visible by reflection at optical wavelengths. UV radiation photoionises the nearer clump of ejected material giving rise to the large HII region. The line of sight is shown at approximately 45° to the disc's axis, so that any reflection nebulosity in the red-shifted outflow region is hidden by the dense disc.

This picture represents our current understanding of the GL2591 system and is probably typical of high mass star formation regions as they reach the MS. It does not preclude the existence of additional YSO's within the same dark cloud—in fact the radio data and the other nearby star would suggest that their existence is to be expected, and that the molecular cloud supports several regions of ongoing star formation. Further observations at radio and IR wavelengths are required to discover the true nature of Campbell's radio sources; if they are excited by the star at the centre of the GL2591 system the current model will have to be modified.
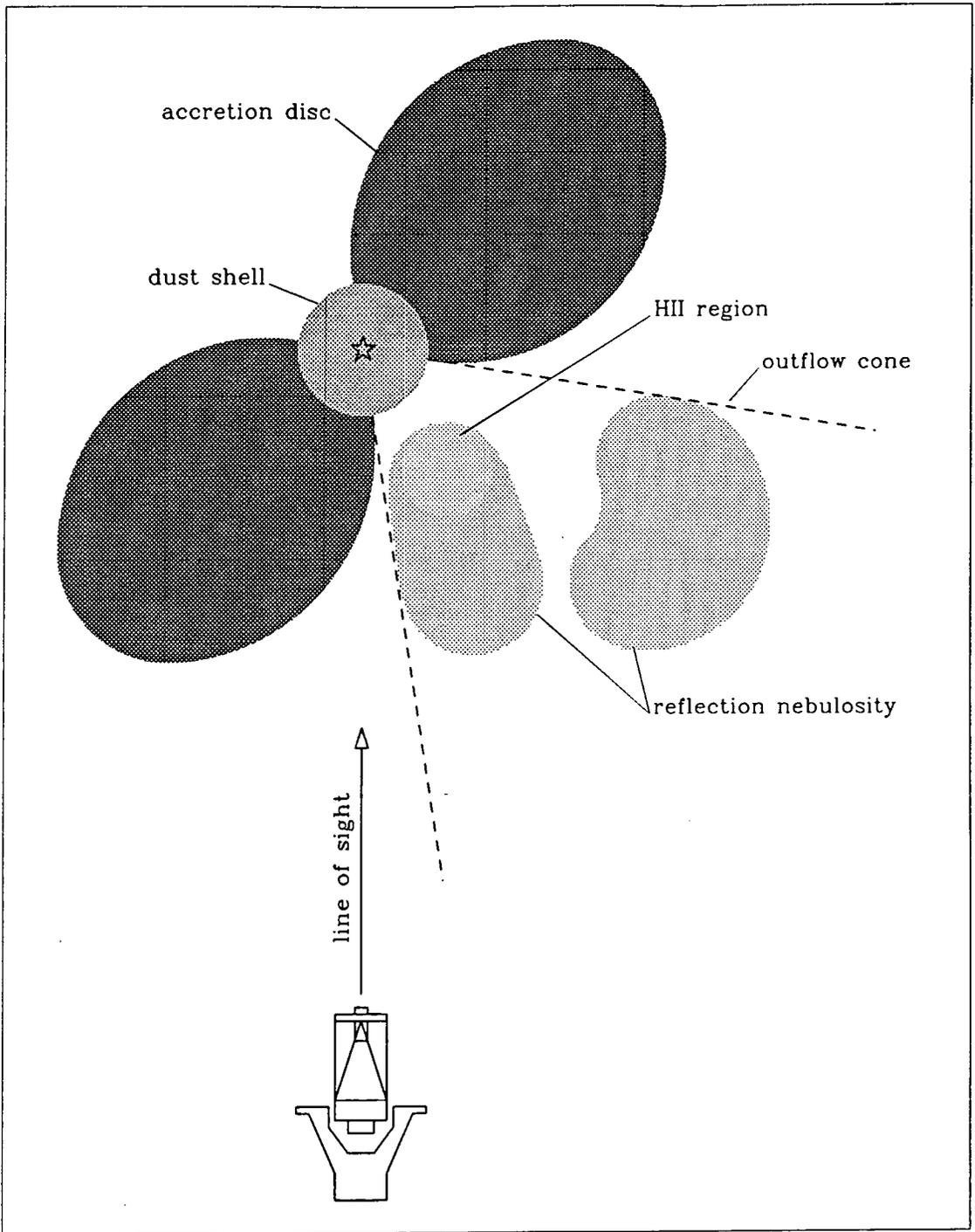
Figure 4.10: Schematic diagram of the GL2591 complex, showing the observed features of the system.

Chapter 5

The nebulosity around
IRAS 07131-0147

During a search for the optical counterparts of 25μ IRAS sources Wolstencroft, Scarrott and Menzies (1989) discovered a small faint bipolar nebula at the position of IRAS 07131-0147. A preliminary analysis of the object led these authors to suggest that the IRAS source is a post main-sequence star, and that the nebula associated with it is a protoplanetary reflection nebula.

This chapter presents CCD images of IRAS 07131-0147 and the surrounding nebula in several colours, and also high spatial resolution polarisation maps of the nebula. The data are used to determine the three-dimensional structure and evolutionary state of the system.

5.1   IRAS 07131-0147

Optical spectra of IRAS 07131-0147 were obtained by Scarrott *et al.* (1990), who found Ti and CaI absorption bands, weak narrow Hα and Hβ absorption lines, and a general absence of emission lines. By comparing the spectrum of IRAS 07131-0147 with those of typical stars of different spectral types and luminosity classes the authors were able to identify it with an M5III star. Scarrott *et al.* also extracted four spectra from the IRAS LRS database (Atlas of Low Resolution IRAS spectra, 1986) for IRAS 07131-0147 and found evidence for broad silicate

emission around 10.5μ (and possibly at 18μ also) on a continuum rising towards longer wavelengths, which suggested that the star has an optically thin, oxygen rich shell surrounding it.

The nature of IRAS 07131-0147 can be investigated by looking at its position in the IRAS colour-colour diagram. Van der Veen and Habing (1988) plotted the $25 - 60\mu$ colour against that for $12 - 25\mu$ for over 8000 dust-gas envelope (DGE) stars and divided the resulting plane into ten zones which contain DGE stars at different evolutionary stages. The IRAS fluxes of IRAS 07131-0147 (2.58 ± 0.21Jy, 4.22 ± 0.34Jy and 3.96 ± 0.48Jy at 12, 25 and 60μ respectively) place it in region IV of the classification scheme of Van der Veen and Habing. According to these authors then, IRAS 07131-0147 is one of a number of variable stars from which mass loss has recently ceased, which are shining through a circumstellar shell that is expanding and becoming increasingly transparent. The circumstellar shell is thick and oxygen rich; in some cases this will already have become a planetary nebula. These conclusions are not inconsistent with the evidence derived from the optical and IR spectra, and it is likely that IRAS 07131-0147 is an evolved star that has moved off the main sequence to the asymptotic giant branch (AGB) of the H-R diagram, and is now evolving off the AGB.

Walker *et al.* (1989) devised a similar methods for classifying objects, using the $60 - 100\mu$ colours as well as $[12 - 25]$ and $[25 - 60]$. They did not restrict the type of object studied to AGB stars only, but included sources of all types and evolutionary stages. In particular they distinguished between two classes of planetary nebulae: "blue" planetary nebulae which show no discernable IR emission lines, and "red" planetary nebulae [1] which exhibit unidentified IR emission bands $(8-13.5\mu)$ and an underlying red continuum. The $[12 - 25]$, $[25 - 60]$ and $[60 - 100]$ colours of IRAS 07131-0147 place it in either the "blue" planetary nebulae or T-Tauri zones of the colour planes defined by Walker *et al.*. The optical spectrum, with its lack of emission lines, rules out any possibility of the object being a T-Tauri

---

[1] Note that in this context the terms "blue" and "red" refer to the relative IRAS colours and not to optical features.

star, so we deduce that it must fall into the category of "blue" planetary nebulae. By definition the unidentified IR emission features are absent from this class of objects (this is consistent with the IRAS LRS spectrum) and it therefore seems likely that the grains surrounding IRAS 07131-0147 are silicates, not carbon rich material such as PAHs which are thought to carry the unidentified infrared features (Cohen *et al.*, 1989).

It is apparent that all the evidence points towards IRAS 07131-0147 being a post main-sequence star that has undergone mass loss, which has culminated in an optically thin oxygen rich circumstellar shell. The star appears to be in a short-lived transitory phase between red giant and the central star of a planetary nebula.

5.2 Observations of the nebula

The Durham Imaging Polarimeter was used at the f/15 focus of the 2.5m Isaac Newton Telescope to observe IRAS 07131-0147 and the surrounding nebula in March 1988. Both direct and polarimetric images were recorded. The direct images were made using V, R and I filters, with short (10sec) and long (300sec) integrations in order to record accurate information at all brightness levels. They were normalised to each other within each waveband and mutually aligned, giving a common image scale of 0.48 arcseconds pixel^{-1}. The effective seeing of the combined images was 1.2 arcseconds. Polarisation images, each of 600 seconds duration, were taken in the V and I wavebands only. The polarisation images were similarly aligned and reduced to the same image scale as the direct images.

5.3 Results

Greyscale intensity images of IRAS 07131-0147 in each of the V, R and I wavebands are shown in figure 5.1. The structure of the object is similar in all three wavebands, with a central star clearly visible between bipolar lobes. There seems
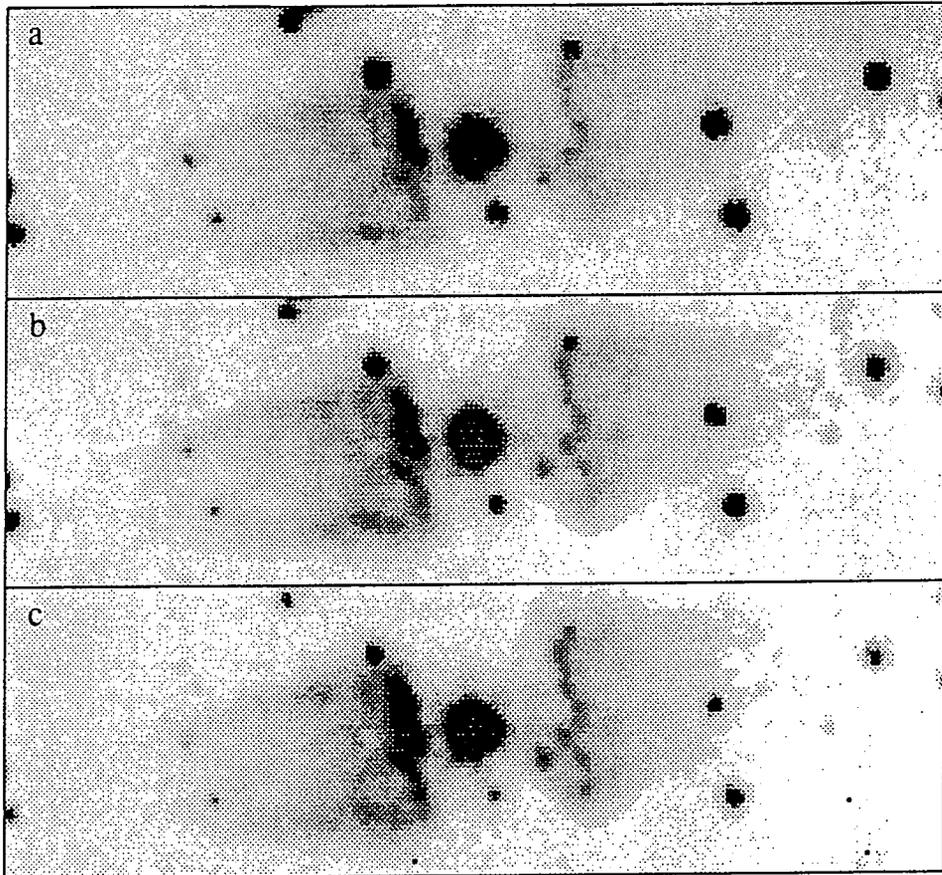
Figure 5.1: Greyscale intensity images of the nebula around IRAS 07131-0147 in the V (a), R (b) and I (c) wavebands.

to be little nebulosity close to the star; the lobes appear to start ~ 7 arcseconds away from it in the form of a line of small knots. The knots are unresolved and have intensity profiles which are apparently stellar-like. Outwards from the knots the fainter lobes show streaks which converge to a focus some 40–50 arcseconds away from the central star. In all of the intensity images the eastern lobe is slightly brighter than its western counterpart; this might indicate that the axis of the nebula is tilted out of the plane of the sky, with the eastern lobe being the nearer.

Figure 5.2 shows a colour image of the nebula, obtained by taking the ratio of the R and I images. The nebula has an almost uniform colour; in particular it is noticeable that the knots are of the same colour as the surrounding nebulosity. This suggests that they are not superimposed emission features, but are part of the matter constituting the lobes. Field stars, which are generally brighter in the R waveband, show up white in this image; a few are seen close to the IRS.

The polarisation data are presented in figures 5.3 and 5.4. These maps show that the nebula is illuminated solely by the central star. The circular pattern is typical of a reflection nebula with a single illuminating source, and shows that the polarisation arises as a result of light from the central star being scattered by grains of dust in the bipolar lobes. The level of polarisation increases with distance from the source to a maximum of $\sim 69\%$ in the I waveband, higher than is normally seen in a reflection nebula (20–40%), and also appears to be higher at the edges of the nebula than along its axis. The variations in the levels of polarisation across the nebula is probably a geometric effect arising from changes in the scattering angle, and is one of a number of important factors which must be taken into consideration when the three-dimensional structure of the system is determined (section 5.4.1).

Polarisation maps covering the central region with a higher spatial resolution are shown in figures 5.5 and 5.6. With the exception of the topmost knot on the western side, the array of knots on each side of IRAS 07131-0147 are polarised
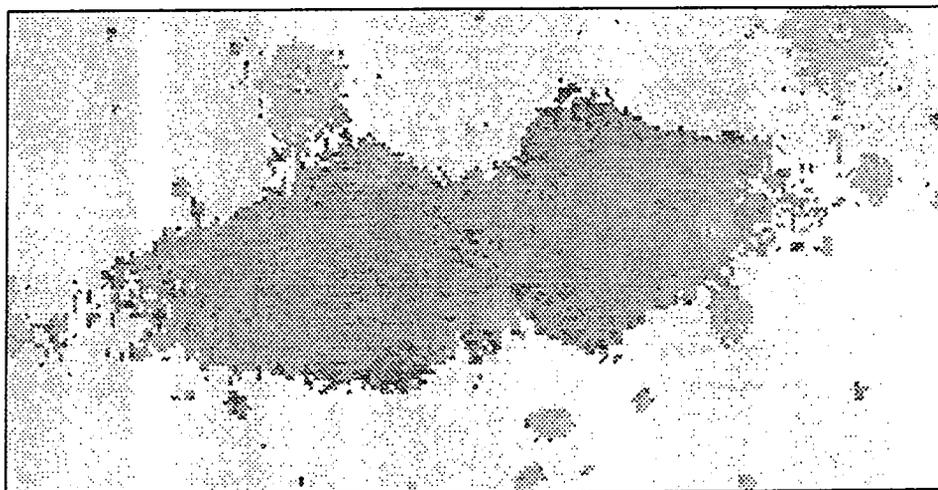
Figure 5.2: Colour image of the nebula around IRAS 07131-0147 obtained by taking the ratio of the R and I images. White corresponds to areas which are brighter in the R waveband.
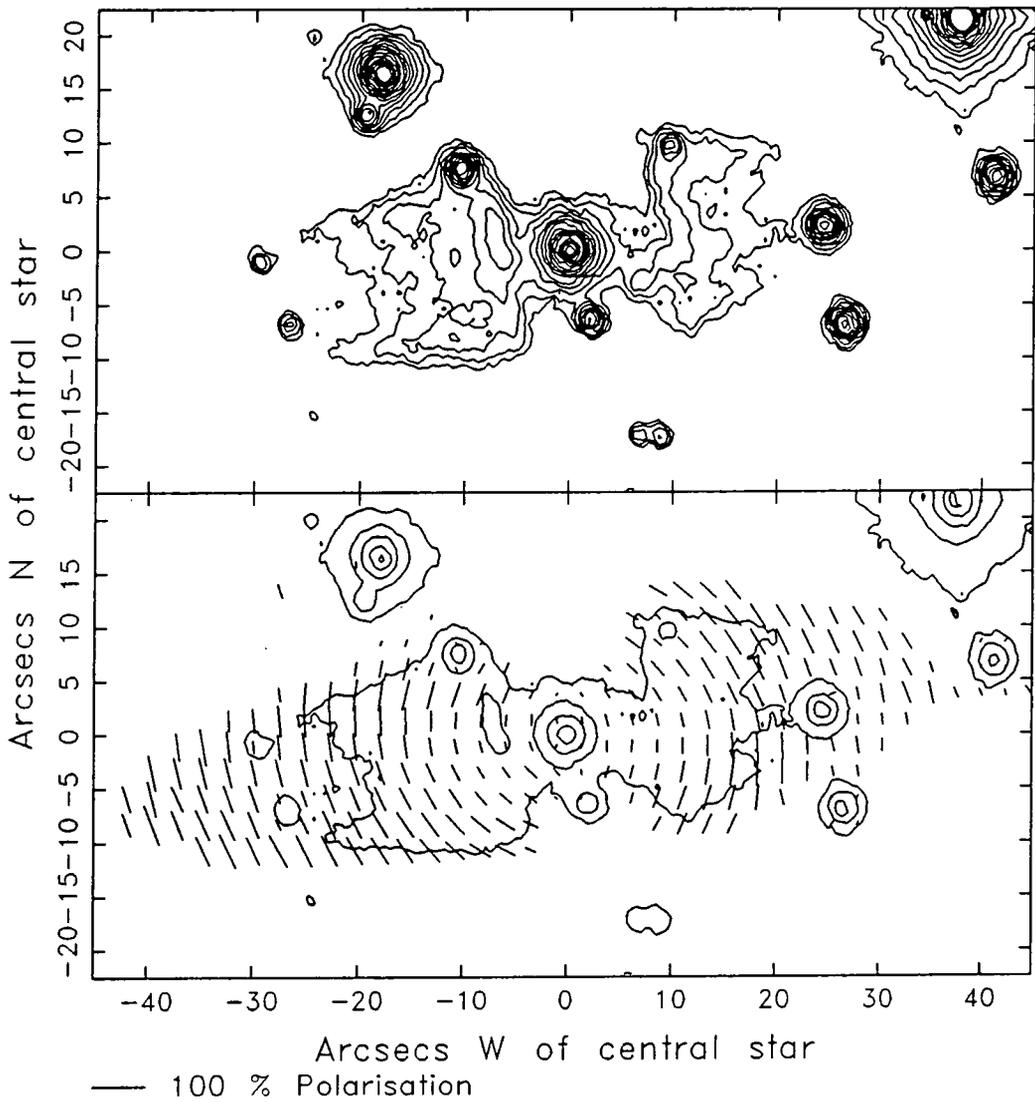
Figure 5.3: Intensity contour and linear polarisation maps of the nebula around IRAS 07131-0147 in the V waveband.
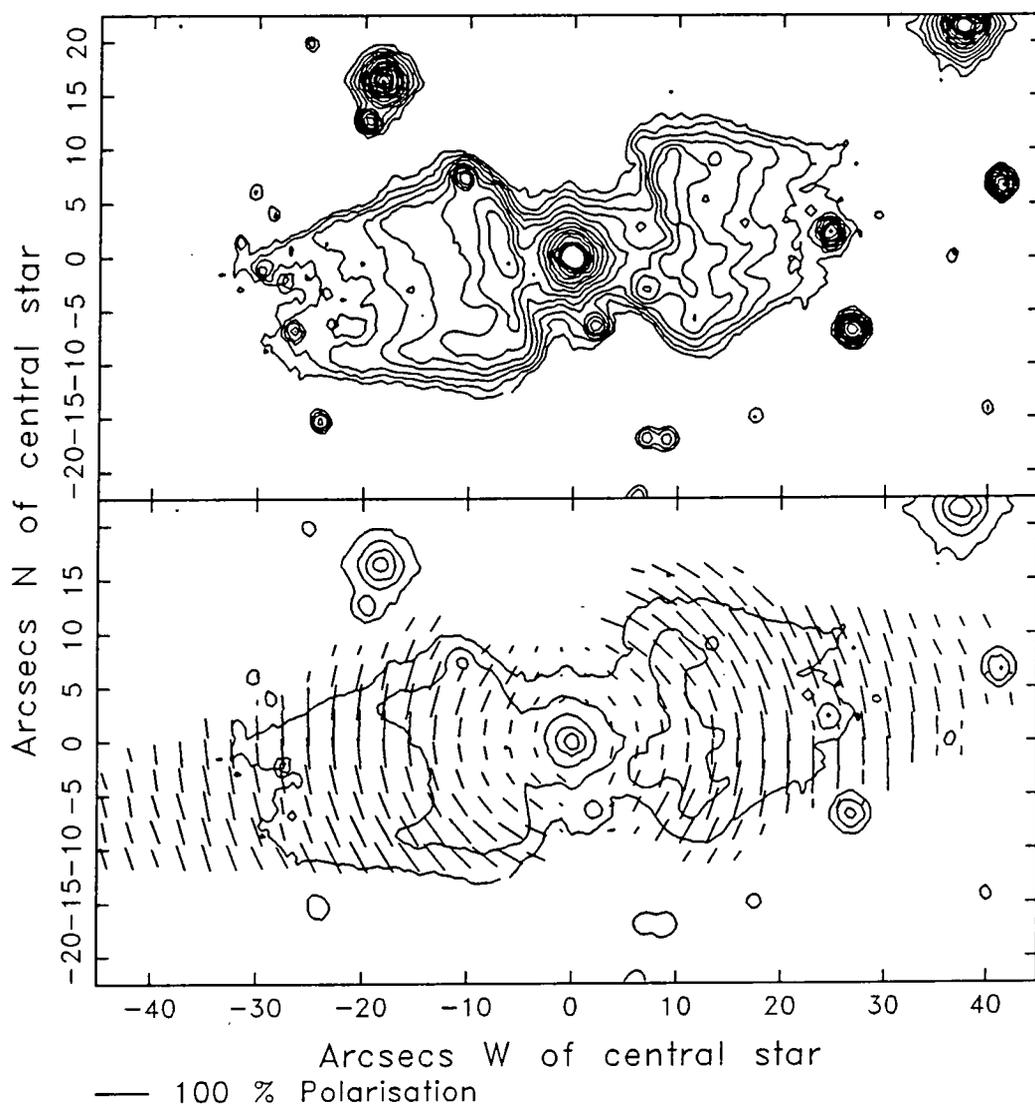
Figure 5.4: Intensity contour and linear polarisation maps of the nebula around IRAS 07131-0147 in the I waveband.
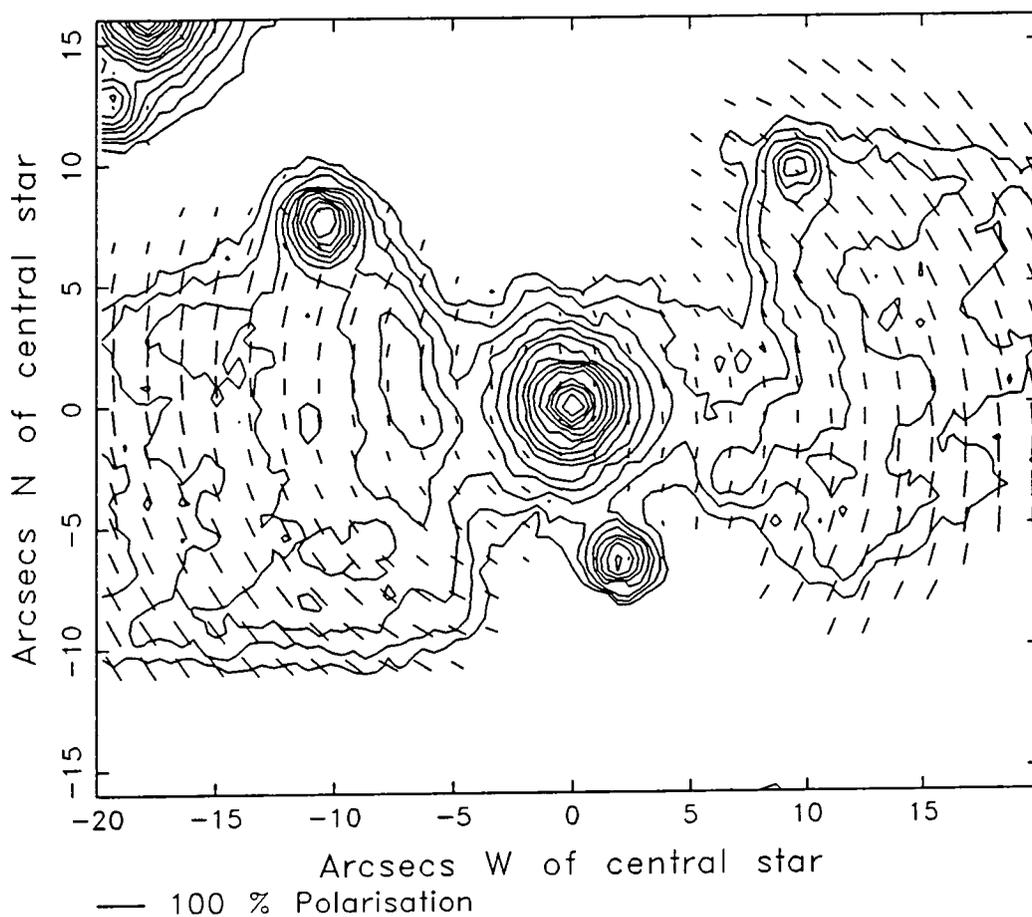
Figure 5.5: High spatial resolution intensity contour and polarisation maps of the nebula around IRAS 07131-0147 in the V waveband.
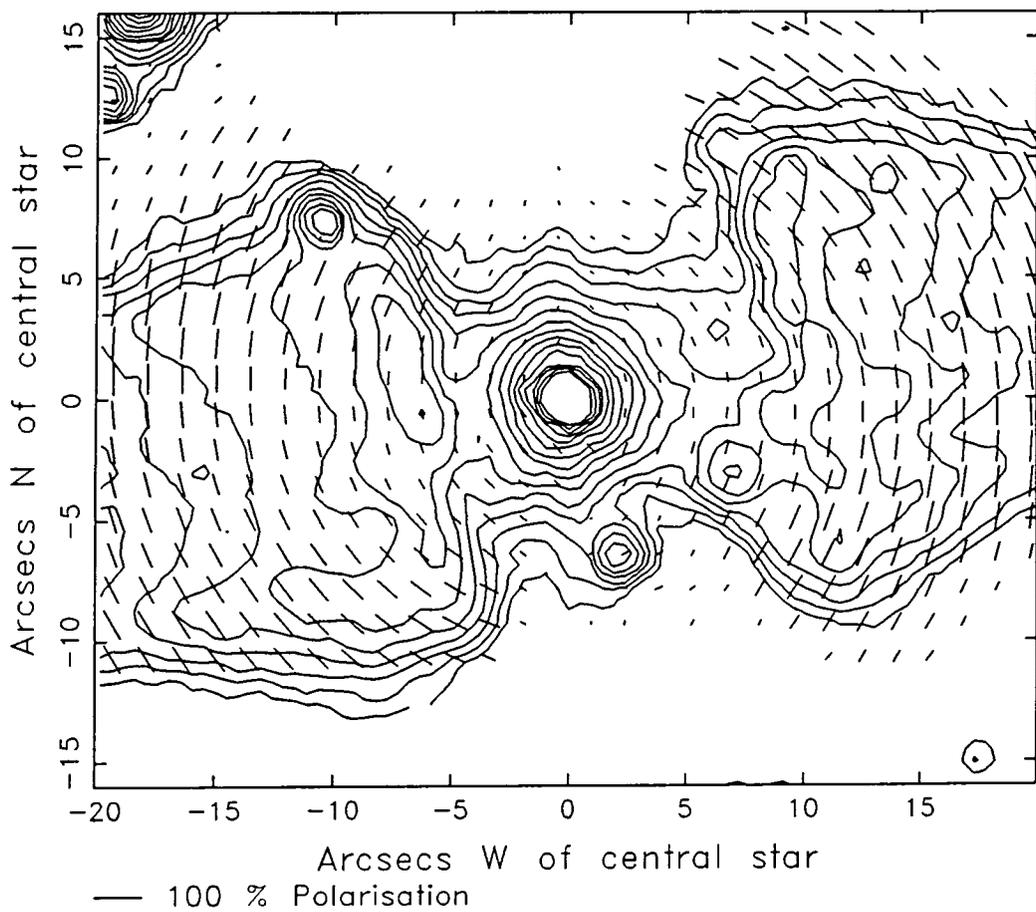
Figure 5.6: High spatial resolution intensity contour and polarisation maps of the nebula around IRAS 07131-0147 in the I waveband.

by approximately the same amount as the nearby nebulosity ($\sim$ 20%) which is confirmation of the earlier suggestion that they are concentrations of scattering material, and not emission features. The knot which appears to be less polarised than the surrounding material in the V waveband is conspicuously brighter in this waveband than in R and I (see figure 5.1). It is seen by emission, and could be a field star that coincidentally lies on the same line of sight as the IRAS 07131-0147 knots. No polarisation is measured to the north and south of the central star in either of the two wavebands studied here; it can be seen from figure 5.1 that these regions are devoid of nebulosity.

5.4 Discussion

5.4.1 The geometry of the IRAS 07131-0147 nebula

The polarisation data allow us to propose a three-dimensional geometry for the IRAS 07131-0147 nebula. Figures 5.7 and 5.8 show profiles of polarisation, polarised intensity and total intensity measured along a line perpendicular to the major axis and 15 arcseconds east of the central illuminator. In both the V and I wavebands the polarisation and intensity have maxima not at the position of the major axis, but at $\sim 7''$ offset from it. The same pattern is seen to the west of the central star. This "limb brightening" effect is a direct indication that the observed bipolar structure of the nebula is a result of light being scattered by dust grains on the walls of an elongated cavity centred on the illuminating star. If the structure were "filled" with a uniform density of dust grains we would expect both the polarisation and intensity to be higher on the major axis than at the edges of the nebula due to the longer line of sight through the scattering material. This is clearly not the case.

Figure 5.9 provides further evidence for a hollow cavity, and gives us a clue about the symmetry of the nebula. Profiles of polarisation, polarised intensity and intensity along the major axis of the nebula are shown. As we have already
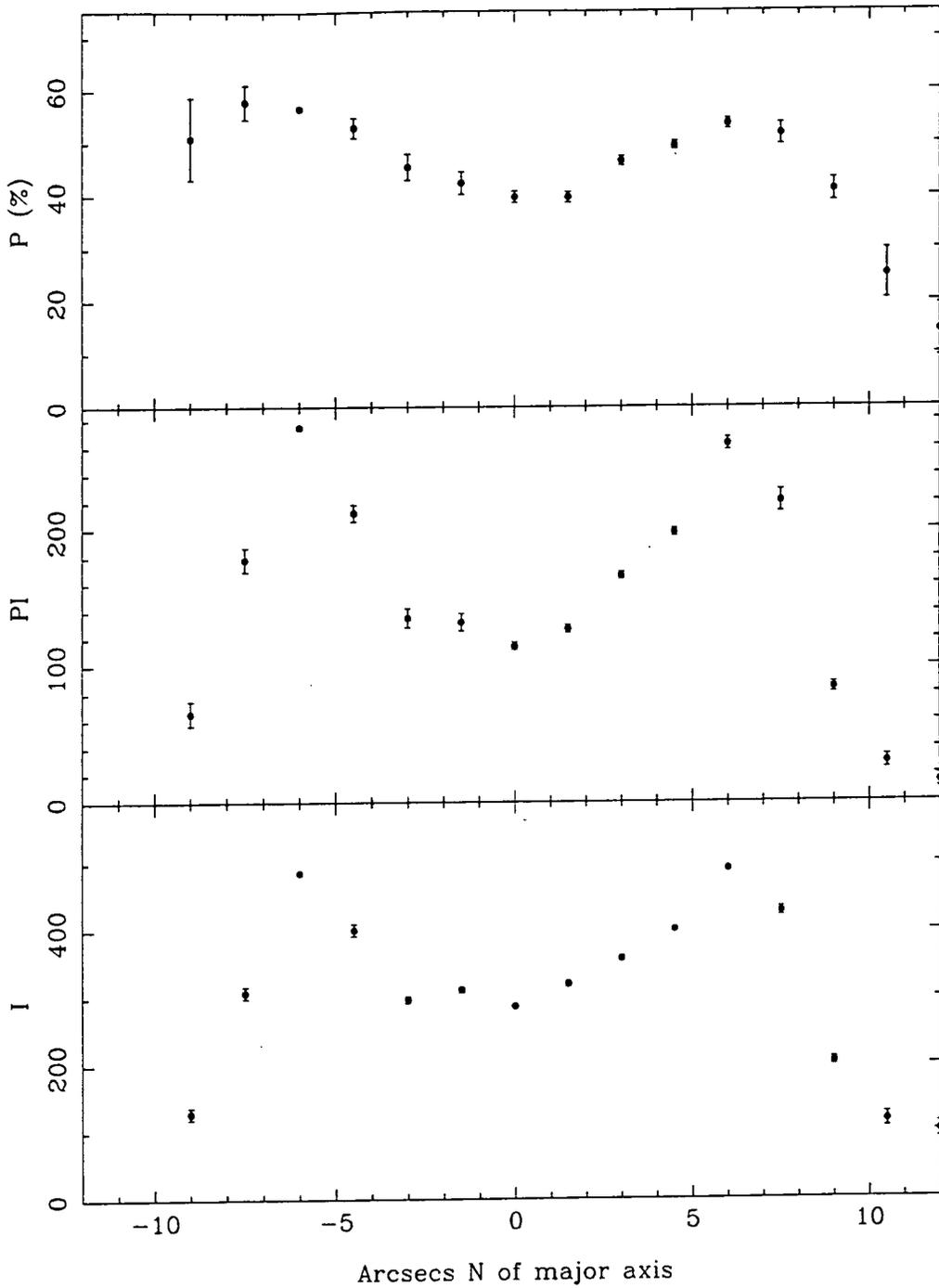
Figure 5.7: Profiles of polarisation, polarised intensity and total intensity measured along a line perpendicular to the major axis at a point 15″ east of the central star in the V waveband.
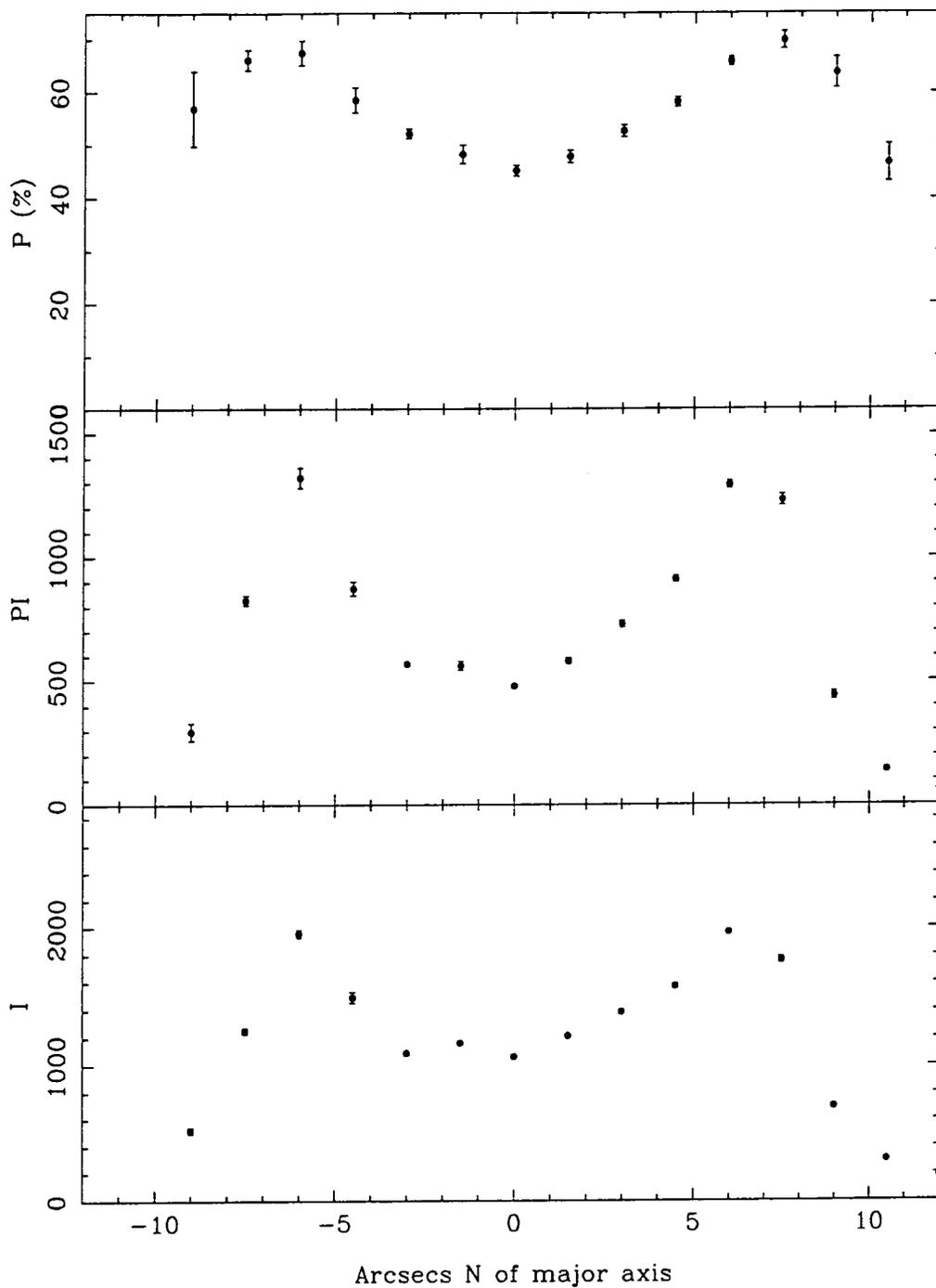
Figure 5.8: Profiles of polarisation, polarised intensity and total intensity measured along a line perpendicular to the major axis at a point 15″ east of the central star in the I waveband.
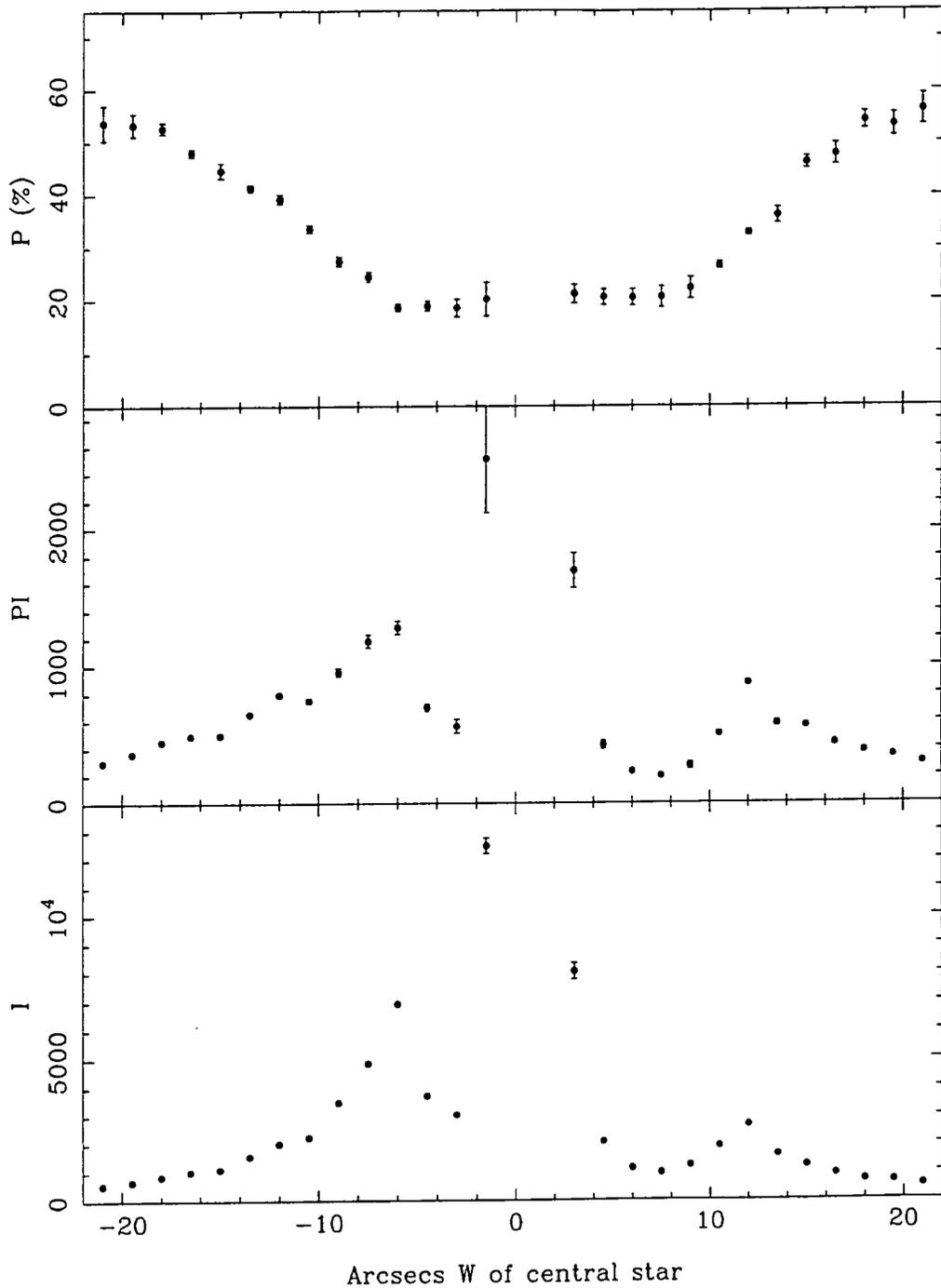
Figure 5.9: Profiles of polarisation, polarised intensity and total intensity of the IRAS 07131-0147 nebula measured along the major axis of the system in the I waveband.

noted, the polarisation increases monotonically with distance from the central star which suggests that the scattering geometry becomes more favourable at greater distances (i.e. the scattering angle approaches 90°). Figure 5.10 shows a schematic diagram of a geometry which would give such an increase in polarisation along the major axis. The line of sight to the observer is shown to be perpendicular to the major axis. It is clear that the shape of the nebula in the schematic diagram is similar to the observed nebular shape; this is an indication that the nebula could have rotational symmetry about its major axis. The polarisation of the schematic nebula measured along the major axis, assuming the simplest case of single scattering by very small (Rayleigh) particles, is also shown, and the shape of the curve is not unlike that defined by the points plotted in the top graph of figure 5.9.

Figure 5.9 also shows that whilst there is a peak in the intensity profile along the major axis at the position of the lines of knots ($\sim \pm 7''$ offset from the centre) there is no corresponding decrease in the polarisation measured at these positions. This further confirms our supposition that the knots are seen by reflection and are not emission features. The knots appear to be sparsely distributed around rings defined by the intersection of the hollow cavity with planes perpendicular to the plane of the sky. The streaks of nebulosity which lie almost parallel to the major axis of the nebula are probably composed of material that has been eroded away from the knots and carried further away from the star by some outflow mechanism.

5.4.2   The effective grain size

The levels of polarisation measured throughout the IRAS 07131-0147 nebula (up to 69% in the I waveband) are much higher than are normally seen in the reflection nebulae that are associated with young stars (20-40%).This suggests that in this case the grains are much smaller than those found in the ISM and in dark clouds where star formation is occurring. Without any detailed knowledge of the geometry of the nebula an upper limit can be put on the grain size.
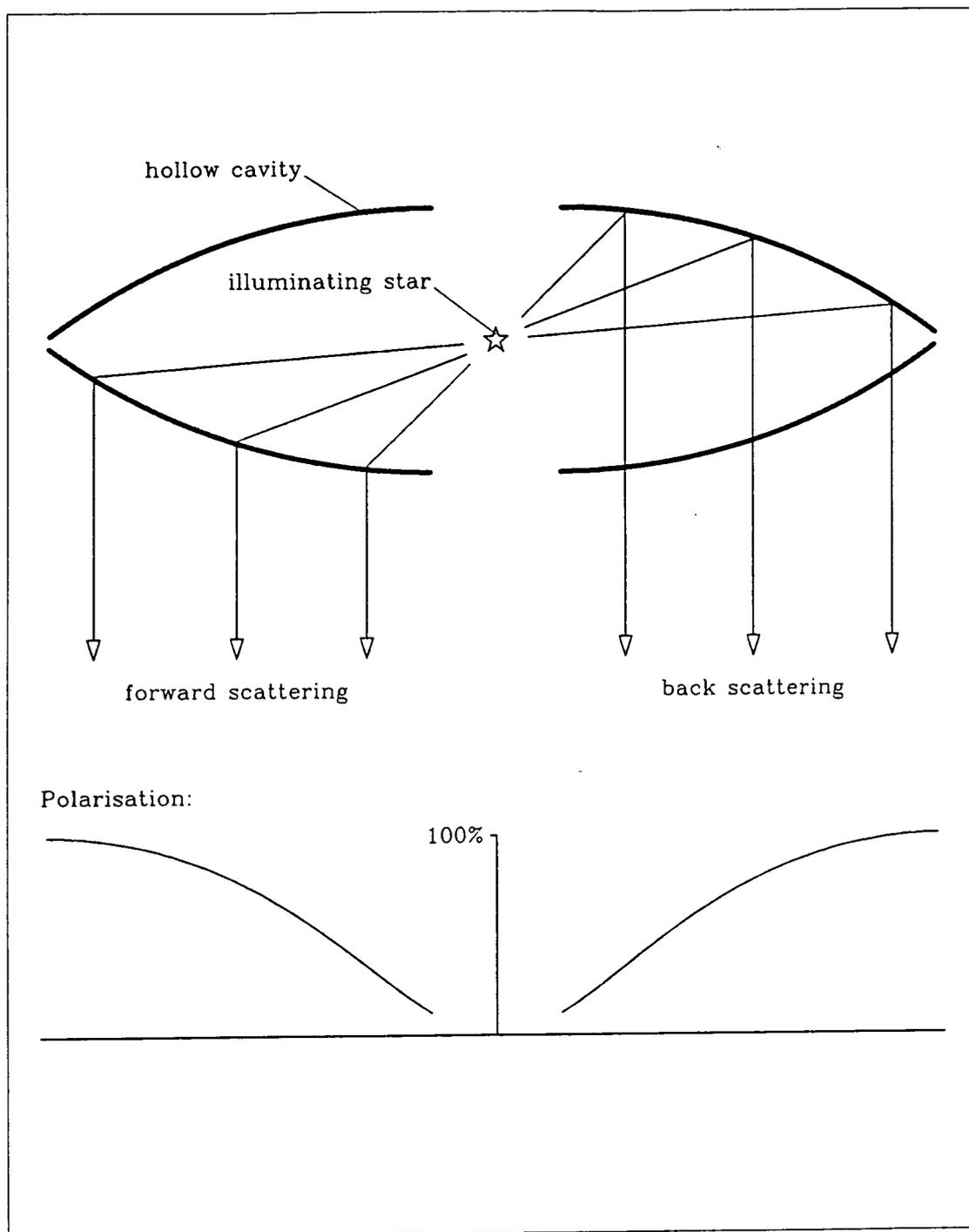
Figure 5.10: Schematic diagram of a hollow structure which would show an increase in the level of polarisation with increasing distance from the central source, due to the scattering angle approaching 90°. The level of polarisation expected for Rayleigh particles is shown.

Mie theory can be used to calculate the polarisation, $P(\theta)$, differential scattering cross-section $\sigma(\theta)$, and the total scattering cross-section $\sigma_T(a)$ as a function of scattering angle θ and particle size a, assuming grains of a specific composition and size distribution. We make the assumption that the grains are silicates with a refractive index of $1.63 - 0.05i$, based on the fact that the position of the IRAS source in the two colour IR diagram is consistent with an oxygen rich circumstellar envelope which could lead to silicate grain formation. Aitken and Roche (1982) showed that the 10μ spectra of several oxygen rich planetary nebulae are fitted well by assuming a composition of silicate grains with small amounts of SiC and graphite, and the LRS IRAS spectra extracted by Scarrott $et\,al.$ (1990) showed evidence of silicate emission from the central star, so it does not seem unreasonable to assume that the silicate grains are present in the nebula. In common with current ISM grain models a power law of the form $N(a) = a^{-n}$ is used for the size distribution of the silicate grains (see Mathis $et\,al.$, 1977), where $N(a)$ is the number of grains of size a, and n is an index dependent upon the effective grain size, which will be determined experimentally.

In figure 5.11 a graph of the polarisation as a function of scattering angle is shown for various power law size distributions of silicate grains. The uppermost curve is for the case where the particle size a is much smaller than the wavelength (Rayleigh scattering); the curve is symmetric about $\theta = 90°$ and has a maximum polarisation of 100% at this scattering angle. If the dust grains in the IRAS 07131-0147 nebula were Rayleigh particles then the observed maximum polarisation (69%) shows that the nebula could not be tilted out of the plane of the sky by more than $\sim 25°$. If we assume the particles are larger and treat them according to Mie theory then figure 5.11 shows that $n \geq 5.3$ in order for polarisation levels of $\sim 69\%$ to be observed, even for scattering angles close to 90° (c.f. $n \sim 3.5$ for the ISM, $n \sim 4.2$ in the reflection nebula NGC1999; Warren-Smith 1983). A power law size distribution would result in a maximum polarisation which is marginally higher in the I waveband than in V, and this is indeed what we observe
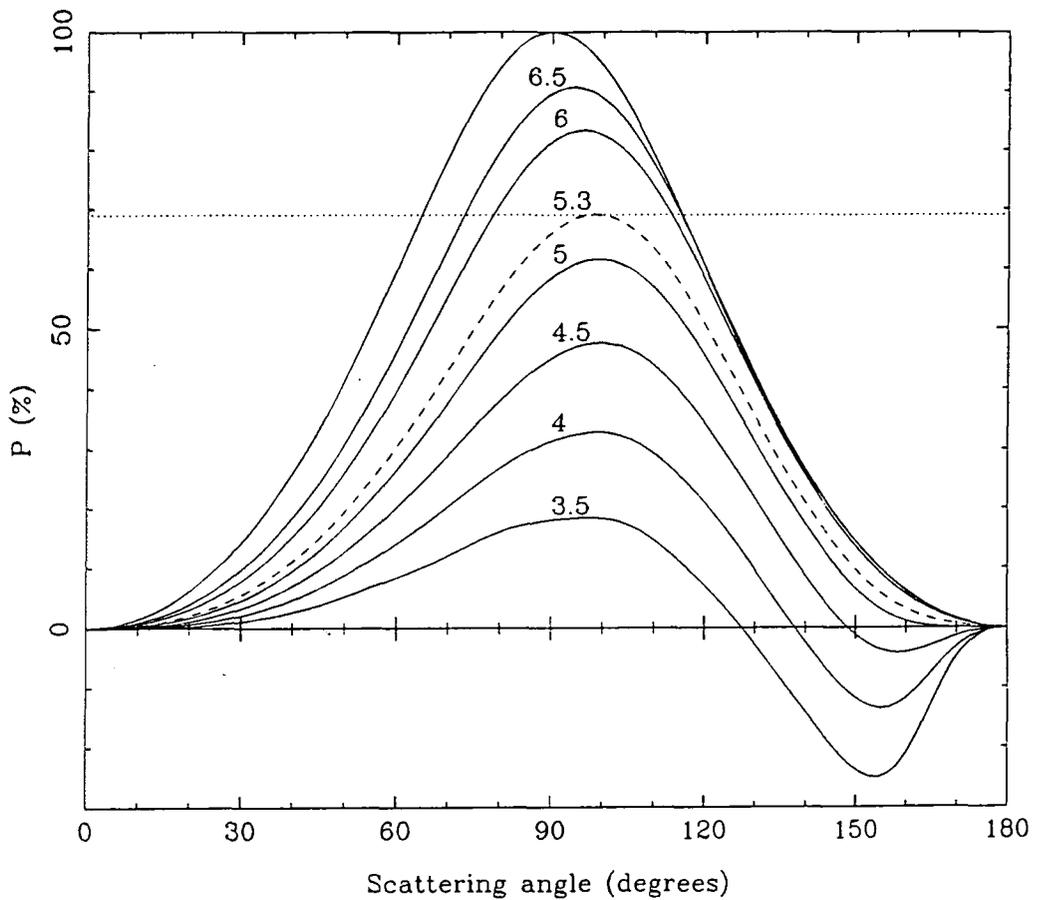
Figure 5.11: Plot of polarisation as a function of scattering angle for various power law size distributions of silicate grains. The uppermost curve is for Rayleigh scattering where the particle size≪the wavelength, which is 800nm for all curves. The power law index for each of the Mie curves is shown.

throughout the IRAS 07131-0147 nebula.

For a power law size distribution there is no mean grain size, but an effective size for the scattering particles, a_o, can be defined by determining the value of a for which $\sigma_T(a)N(a)$ reaches a maximum. The function $\sigma_T(a)N(a)$ is plotted against particle size a for power law index $n = 5.3$ in figure 5.12, and it can be seen that $a_o \lesssim 0.15\mu$. Therefore under our simple assumptions it is apparent that the effective size of the scattering particles in the IRAS 07131-0147 nebula is much smaller than in the ISM or dark cloud reflection nebulae ($\sim 0.3\mu$ and $\sim 0.25\mu$ respectively).

If we assume that the particle size distribution is of the form $N(a) = a^{-5.3}$ then Mie theory can also be used to set a limit on the inclination of the nebula to the line of sight. It has already been established that the eastern side of the nebula is brighter than its western counterpart—the difference amounts to a factor of ~ 2 in V, R and I (see figure 5.9). If the scattering centres were Rayleigh particles then no angle of inclination could account for this difference in brightness, since the differential scattering cross-section $\sigma(\theta)$ would in this case be symmetric about 90°. Figure 5.13 shows $\sigma(\theta)$ plotted as a function of scattering angle θ for Rayleigh particles, and also for Mie particles with a power law size distribution of index -5.2. The curve for the Mie particles is highly asymmetric which indicates that for a large inclination to the line of sight the forward scattering lobe of the nebula would be much brighter than the back-scattering one. In order for the difference in brightness between the two lobes to be a factor of ~ 2 at most, it is clear that the nebula cannot be tilted by more than $\sim 18°$ out of the plane of the sky.

5.4.3 Formation of the system

Given that the star at the centre of the IRAS 07131-0147 nebula is an evolved object which has undergone mass loss, the morphology of the nebula must be explained in a manner that is consistent with current theories of AGB evolution and planetary nebula formation. It is generally accepted that post AGB evolution
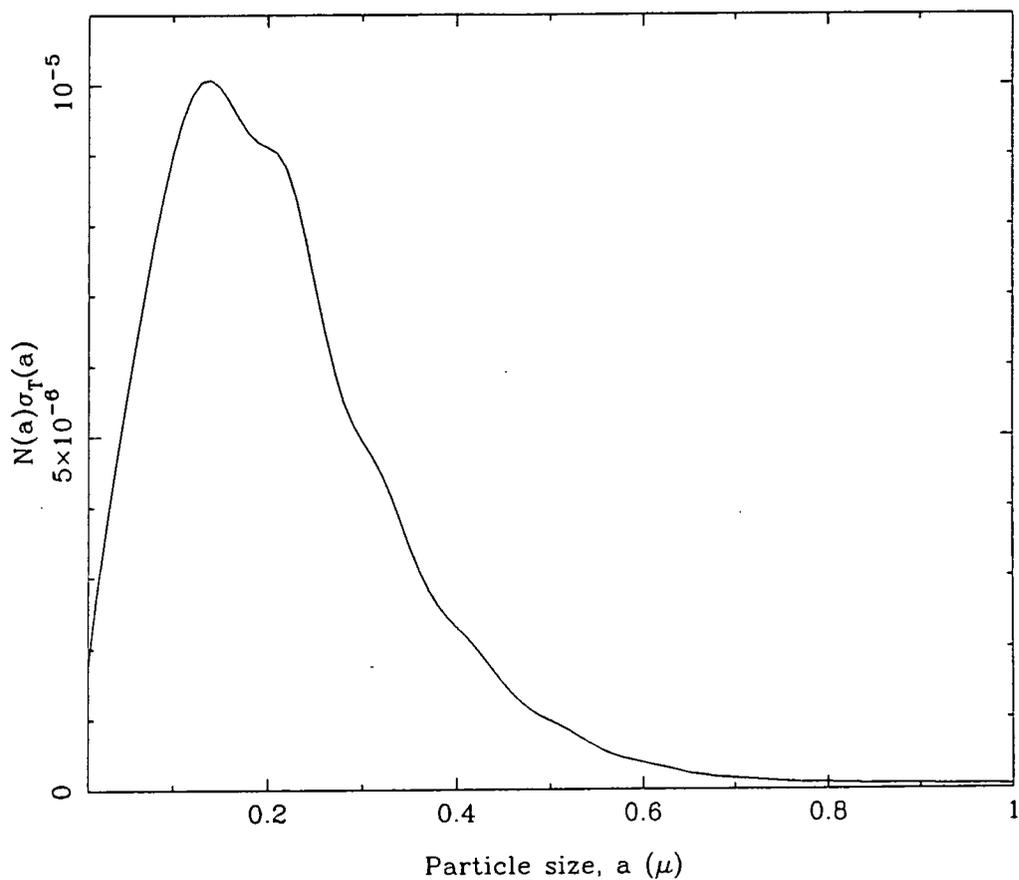
Figure 5.12: The product of the total scattering cross-section $\sigma_T(a)$ and the particle size distribution $N(a)$ plotted as a function of particle size, (a) for silicate grains. The wavelength used is 800nm, and the size distribution function is $N(a) = a^{-5.3}$.
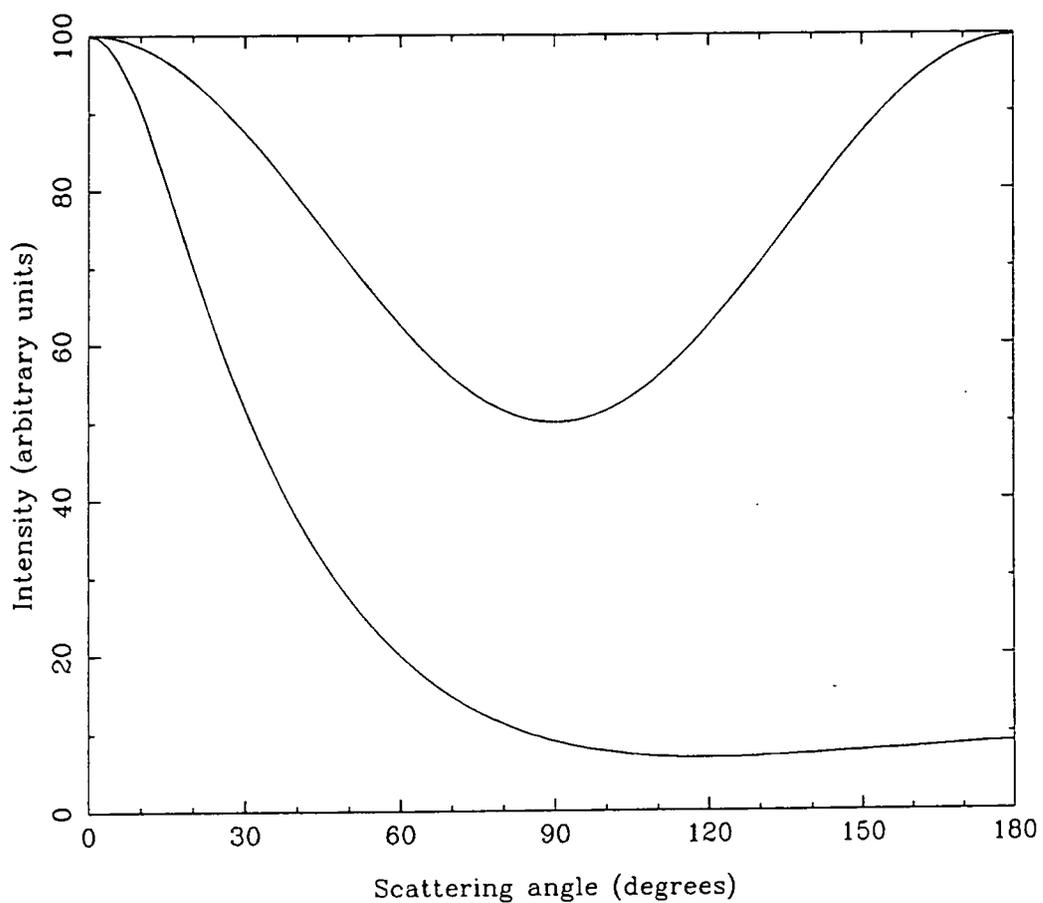
Figure 5.13: The differential scattering cross-section plotted as a function of scattering angle for Rayleigh particles (upper curve) and Mie particles with a power law size distribution of index -5.3. The two curves are normalised to have the same value at $\theta = 0°$.

begins with a period where the extended red giant envelope (RGE) is formed by mass loss generated by a "slow wind", giving a reflection nebula with an obscured star located at its centre (e.g. GL2688). This is followed by a lower density "fast wind" which clears material away from the regions close to the stellar core, and which drives a shock wave into the RGE, creating a bright shell within the envelope. The stellar core contracts and becomes visible as the material around it is swept away by the fast wind; eventually it heats up sufficiently to ionise the remains of the RGE, which is then seen in the emission line radiation characteristic of young planetary nebulae. The transition from AGB star to the central star of a planetary nebula is extremely rapid—it has been estimated to take place in 500-2000 years (Bujarrabal et al., 1988).

Balick et al. (1987) showed that whilst the slow wind usually propagates relatively uniformly in all directions from the AGB star, the fast wind is often highly collimated which results in axisymmetric shock fronts in the RGE. Evidence for asymmetric fast winds is seen in the form of bipolarity of the resulting planetary nebulae; the lobes are often of a bow-tie or butterfly shape (see for examples the photographic catalogue of Balick, 1987, which shows many planetary nebulae with bipolar structures). Whilst it is clear from observational evidence that asymmetries do occur in the fast outflows from AGB stars, the collimating mechanism is not obvious. Zuckermann and Gatley (1988) showed that the likelihood of outflow asymmetries being caused by the gravitational effects of nearby companion stars, or by a rapidly rotating central star, is low, but that it might be possible for collimation to be caused by a circumstellar disc, or a magnetohydrodynamic effect. There is no evidence in the data presented here for magnetically aligned grains in a disc around the central star (which would be seen as polarisation vectors parallel to the plane of the disc, perpendicular to the major axis of the nebula), and if such a disc did exist it would have to be optically thin in order for the star to be seen so clearly. On the basis of our polarimetric data, however, the possibility of a small-scale circumstellar disc collimating the fast wind cannot be completely

rejected even though it seems an unlikely scenario.

Balick (1987) shows that protoplanetary nebulae of intermediate age could have a near nuclear structure resembling a cylindrical sleeve around a central cavity if a spherical or ellipsoidal RGE is penetrated by a bipolar fast wind. This type of cylindrical structure would account for the large-scale features of the nebula around IRAS 07131-0147; the bright rims of the nebula represent the edges of the cylindrical cavity that has been excavated in the RGE by the fast wind. The high polarisation of the edges of the cavity shows that they are seen by scattered light, not by shock excited emission, which indicates that the fast wind has stopped and that mass loss has ceased. This is in agreement with the conclusions drawn from the IRAS colours of the central star in section 5.1. Although the cavities of the nebula appear to converge to foci on either side of the central star, examination of these regions shows no evidence of emission knots caused by interaction of the fast wind with the RGE (HH-type knots). This is further evidence that the fast wind has now ceased.

Some insight can be gained on the nature of the small-scale features of the IRAS 07131-0147 nebula by making comparisons with other objects at a similar evolutionary stage which have been more well studied. Since the transition from AGB star to planetary nebula is rapid, such examples are few and far between, and the evolutionary state of many of the candidates is shrouded in uncertainty. There are, however, a handful of objects which may help to shed light on the nature of IRAS 07131-0147.

Knotty structures are not uncommon in objects which represent the transitory state between AGB star and planetary nebula; M2-9 is one of the better examples. The shape of M2-9 is similar to that of the IRAS 07131-0147 nebula with bipolar lobes centred on a bright star, and the nebular lobes also contain knots and streaks. The star itself is variable, and interestingly it has been shown that the knots also vary in brightness and position, on a timescale of $\sim$ 10 years (van den Bergh, 1974). Future investigations of IRAS 07131-0147 and its associated nebula may

well reveal similar variability.

From observations of M2–9, Aitken and Roche (1982) show that there is strong evidence to suggest that dust grains form in the winds associated with planetary nebulae, very close to the hot central stars. Schmidt and Cohen (1981), in a study of the protoplanetary nebulae GL618 and M2–9, concluded that the physical conditions in such nebulae are conducive to the formation of dust, dense condensations of atomic gas, and also of molecules. They assert that it is possible for grains which condense as they cool soon after being released from the stellar surface to act as condensation sites for other molecules; from this we can see how the knotty areas close to IRAS 07131-0147 might be formed as grains coalesce around particular concentrations of condensation sites. Ablation of material from these knots would then give rise to the streaks seen in the outer part of the nebula by scattered light.

It has been suggested (van der Veen, 1987) that young Mira stars lose mass in discrete outbursts resulting in clumps of matter surrounding the star, and it might be possible that the same thing happens as the star continues to evolve, so that the knots we see in the case of IRAS 07131-0147 are direct products of mass outflow, although why they should be distributed in rings on either side of the star is unclear. Balick *et al.* (1987) mention the possibility of "soft bullets" which plough into the the RGE—the "bullets" are formed by the interaction of the fast wind with the surrounding envelope and would be expected to lie on the axis of the nebula. These "soft bullets" can be identified with the ansae which are often seen on either side of the central star of young planetary nebulae (e.g. IRAS 09371+1212; Morris and Reipurth 1990), but cannot explain the distribution of the knots around IRAS 07131-0147.

None of these explanations for the existence of knotty structures in a protoplanetary nebula can account for the spatial distribution of the knots that we see close to IRAS 07131-0147. There is currently no well-developed model for mass outflow that predicts concentrations of scattering centres lying in rings close to the central star. However, in discussing the nebulosity close to GL2591 on page 70

the possibility of a vortex ring of material forming as a result of a short period of mass ejection was mentioned, and it might be possible for such a structure to form in the RGE around IRAS 07131-0147 after a short burst of mass outflow. The mechanism which collimates the fast wind could form a kind of nozzle through which the mass ejected from the star would flow; the resulting jet of material could then form a ring as it interacts with the extended RGE. The outburst of matter might simply be due to a fluctuation in the density of material carried by the fast wind, and could cause the arrangement of knots that are seen here.

5.5 Conclusions

The highly polarised bipolar nebula associated with IRAS 07131-0147 is a protoplanetary nebula, formed during the post-AGB evolution of the central star. This conclusion cannot be reached from the polarisation measurements and IRAS colours alone, but requires recourse to the optical spectrum in order to rule out the possibility of it being a pre-main sequence object.

In order to explain the high levels of polarisation measured throughout the nebula the effective size of the scattering particles has been found to be $\lesssim 0.15\mu$, assuming the grains to be silicates. This is consistent with the idea that the grains are freshly condensed in the material surrounding an oxygen rich giant star. The polarimetric data also show that the structure of the nebula resembles a hollow cylinder which is viewed along a line of sight almost perpendicular to its major axis; this cylinder is thought to be a cavity in the RGE eroded by the fast wind from the central star. The edges of the cavity are seen by scattered light and not emission so we conclude that the fast wind has ceased; the object is in the highly transitory state between the cessation of mass loss and the onset of ionisation of the remains of the envelope.

The observed bipolar structure of the nebula indicates that the fast wind did not occur isotropically, although there is no direct evidence from the polarisation data for a collimating mechanism close to the central star.

Chapter 6

OH 231.8+4.2

OH 231.8+4.2[1] is a highly evolved object at a distance of 1.3-3pc which exhibits strong IR and OH emission but which has no optical counterpart. It is associated with optical and IR nebulosity that has a bipolar morphology.

In this chapter linear polarisation measurements are used to investigate the geometry of the optical nebula, and the nature of the particles within it are discussed.

6.1 Previous work on OH 231.8+4.2

In a survey of planetary nebulae, Turner (1971) discovered OH 231.8+4.2 close to the planetary nebula NGC2438. H_2O emission was discovered in the same region shortly afterwards by Morris and Knapp (1976) and a 2.2μ source was discovered by Wynn-Williams, Becklin and Neugebauer (1974). Cohen and Frogel (1977) reported a red nebula composed of two bar-like components centred on OH 231.8+4.2. They inferred from the low reddening in the direction of OH 231.8+4.2 that the red colour is intrinsic to the nebula itself.

Allen *et al.* (1980) presented IR maps which confirmed the bipolar nature of the OH 231.8+4.2 nebula, and also made spectroscopic observations in the IR which led

---

[1]On its discovery OH 231.8+4.2 was labelled OH 0739-14 according to its geocentric coordinates. Contemporary convention now labels OH objects according to their Galactic coordinates; consequently the nomenclature OH 231.8+4.2 is used throughout.

them to propose that OH 231.8+4.2 is an M star. They attributed the nebulosity to mass loss from the central star which they suggested could be a Mira variable.

Optical spectra of the brightest knot of nebulosity close to OH 231.8+4.2 were obtained by Cohen (1981) who classified the illuminating source as an M9III star. Subsequent long-slit spectroscopy along the length of the nebula confirmed this (Cohen et al., 1985) and also revealed the presence of a Herbig-Haro like knot at the end of each nebular lobe. The knots were shown to be shocks in an extensive circumstellar envelope which is rich in nitrogen; the central star would require a mass of $> 3M_\odot$ in order for convective processes to bring nitrogen to its surface. The presence of both OH and H_2O emission appear to be an indication that the circumstellar shell is also rich in oxygen.

Deep $H\alpha$/[NII] images of OH 231.8+4.2 obtained by Reipurth (1987) showed that the filamentary optical nebulosity runs along the axis of a bipolar bubble structure which is seen purely in emission-line radiation. The proposed HH objects of Cohen et al. were found to lie on the front edges of the bubbles. Reipurth proposed that the central star is hidden from direct view at optical wavelengths by a thin circumstellar disc, which also obscures part of the southern nebulosity. In subsequent evolution of the central star the disc might be expected to cause bipolarity of the planetary nebula resulting from the ionisation of the ejected RGE.

Optical and IR polarisation measurements were made by Heckert and Smith (1988) at the position of OH 231.8+4.2. They found the source to be highly polarised ($\sim 30\%$) at optical wavelengths, and attributed this polarisation to scattering off a mixture of 0.05μ silicate grains and 0.1μ ice grains. The polarisation measured at longer wavelengths was thought to be caused by dichroic extinction by grains aligned by a supersonic flow along the axis of the nebula (see Gold, 1952a, b).

NIR images of the nebula were made by Woodward et al. (1989) who showed that the northern HH object is seen by IR continuum emission. They also measured the extent of the circumstellar disc, and inferred that the emission line bubbles seen

by Reipurth represent the edges of evacuated cavities, with the optical nebulosity being seen by scattered light from dust within each cavity.

6.2 Polarimetric observations of OH 231.8+4.2

6.2.1 Observational details

OH 231.8+4.2 was observed in February 1989 using the Durham Imaging Polarimeter with its associated hardware as described in chapters 1 and 2, and the DUPCAT software described in appendix A. A total of four CCD frames, each of 300 seconds duration, were taken at the f/15 focus of the 3.9m AAT. No filter was used, and the atmospheric seeing was $\sim 1.5''$. Due to a lack of time it was only possible to observe a single field which contains the central section of the filamentary nebulosity associated with OH 231.8+4.2.

6.2.2 The basic results

Figure 6.1 shows a greyscale intensity image of the OH 231.8+4.2 nebulosity formed by adding all 8 polarisation images together. A narrow dark lane separates the nebula into two filamentary structures; the position of the OH/IR source is in this dark lane, but no optical counterpart is seen. It is clear that the filaments are not straight but have distinct kinks and bends, and in addition they have a somewhat knotted appearance. The apparent clumpiness is not however solely due to the physical structure of the filaments, since the image is confused by the presence of a number of foreground field stars which cannot be distinguished from the nebulosity in this image. The filaments on both sides of the dark lane extend as far as the HH objects reported by Cohen *et al.* and Reipurth, which lie close to the bright knots to the extreme north and south of this image.

Intensity contour and linear polarisation maps are presented in figure 6.2. The nebula is highly polarised, with a maximum polarisation of $\sim 40\%$ in one of the southern knots. Some of the knotty features have very low levels of polarisation;
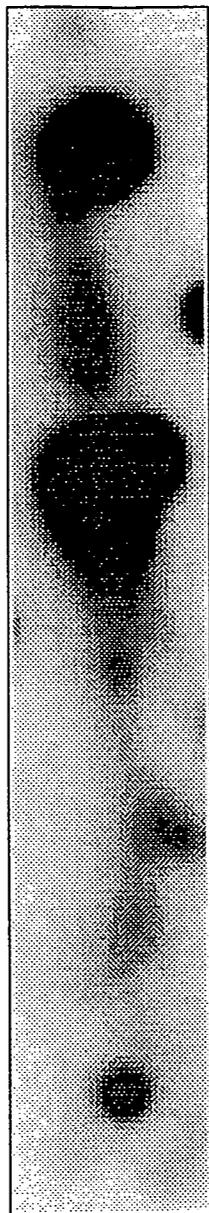
Figure 6.1: Greyscale intensity image of the OH 231.8+4.2 nebulosity.
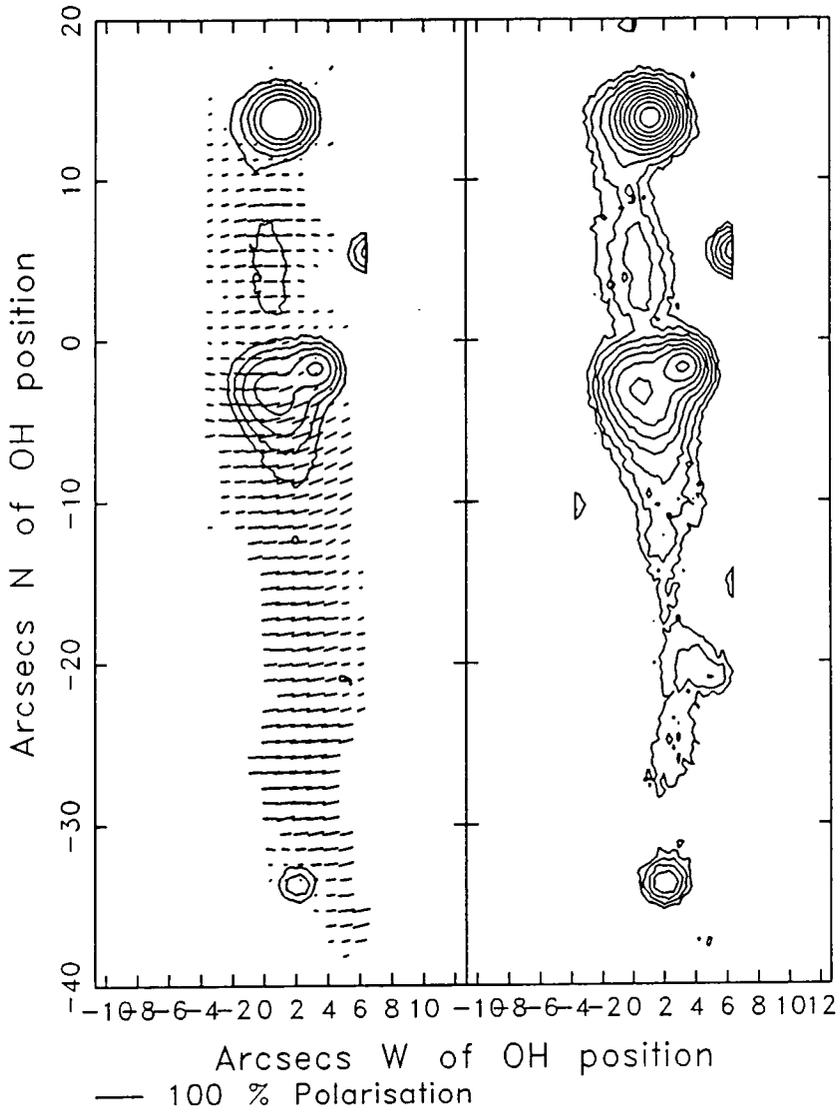
Figure 6.2: Intensity contour and linear polarisation maps of the OH 231.8+4.2 nebula.

these are probably unpolarised field stars whose radiation dilutes the polarised light from the nebula.

The pattern of polarisation vectors is roughly centrosymmetric over the pear-shaped nebulosity in the centre of the map, suggesting that it is a reflection nebula illuminated by a source which lies at the centre of the pattern, in the region of the dark lane dividing the filamentary nebula into two components. In the dark lane itself, however, the centrosymmetric pattern is distorted so that the polarisation vectors lie parallel to it. The pattern of the polarisation vectors over the northern filament is distorted in a similar fashion, but to a lesser degree.

6.3 Comparison with other measurements

Heckert and Smith (1988) compiled a list of optical and IR polarisation measurements for various regions of the OH 231.8+4.2 nebula. Since their paper omits the exact positions at which their measurements were made the only direct comparison that can be made with the high resolution data presented here is at the position of the OH/IR source. Even at this position the measurements of Heckert and Smith cannot be reproduced exactly since they used a $16''$aperture, and the image passed by the occluding bars of the polarimeter's grid assembly is only 11 arcseconds wide. Consequently a software aperture of $8''$ was used to measure the polarisation at the position of OH 231.8+4.2; it was found to be $18.8 \pm 1.0\%$ at a PA of $98.6 \pm 1.5°$. Heckert and Smith obtained a value of 33–55% at an angle of 112–115° in the R/I wavebands in their aperture. The difference between the two measurements is probably due to the fact that the large aperture used by Heckert and Smith contained a considerable area of nebulosity, which is polarised by as much as 35% in this region.

Although direct comparisons cannot be made over the rest of the nebula we can see from figure 6.3 that on a superficial level at least our results agree with those of Heckert and Smith. In this diagram the level of polarisation and position angle are plotted as a function of distance from the OH/IR source along the major
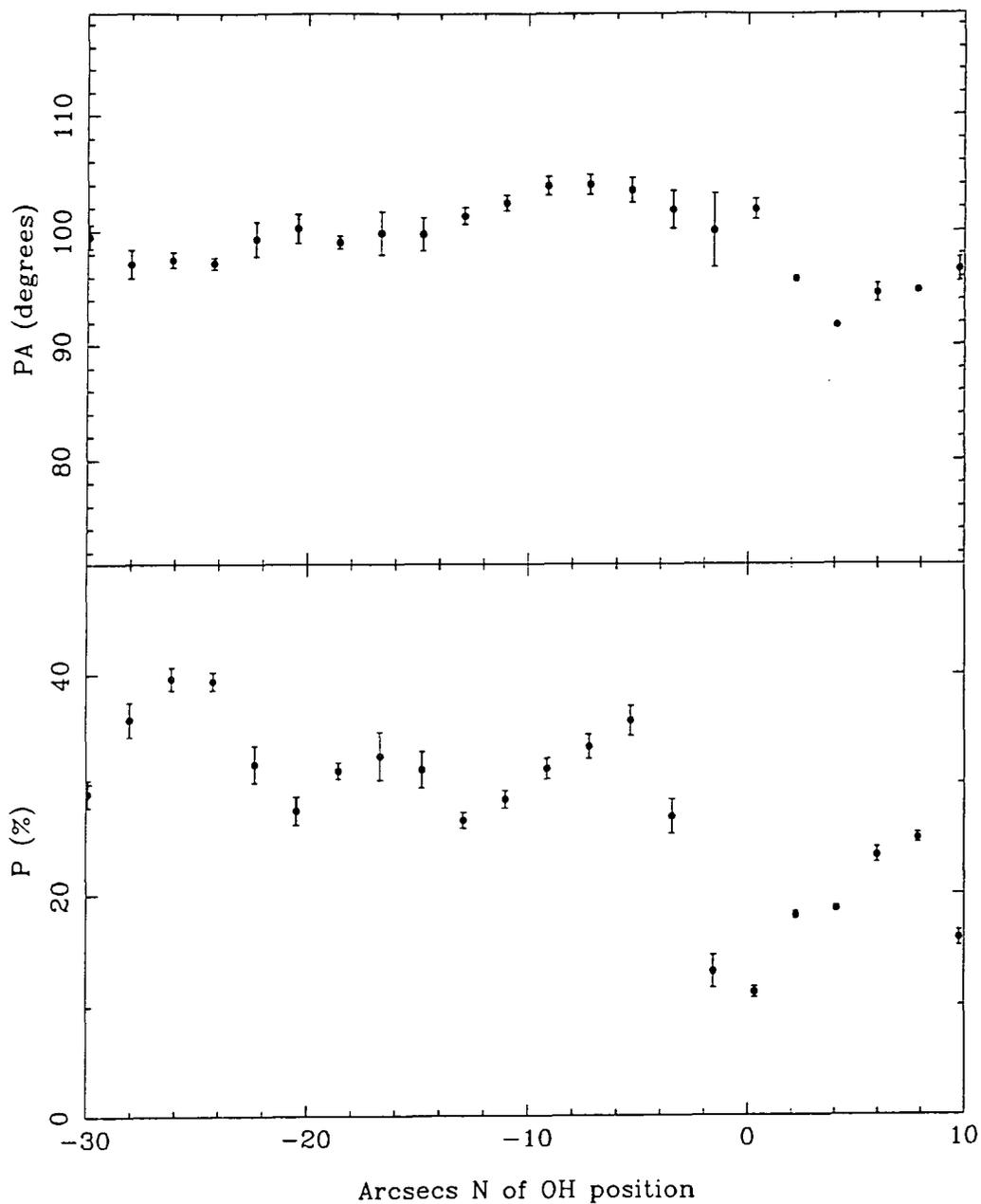
Figure 6.3: The level of polarisation and position angle along the axis of the OH 231.8+4.2 nebula.

axis of the nebula. Heckert and Smith obtain values of 33–38% at 108–114°; it can be seen that these are consistent with the measurements shown in figure 6.3.

6.4 The location of the illuminating source

In figure 6.4 intensity contour and polarised intensity maps of the central region of the OH 231.8+4.2 nebula are shown. In the polarised intensity map the vectors have been rotated by 90° so that they point to the location of the illuminating source, which clearly lies in or near the dark lane separating the northern and southern nebulosities. The majority of the vectors form a radial pattern, whose centre can be more precisely determined using an iterative process to estimate the source position for which the difference between the expected PA and the observed PA of the polarisation, summed over every point in the nebula, is a minimum. The optimum position for the illuminating source according to this criterion is $\sim 2.1''$ north of the OH source position (as determined by Morris, Bowers and Turner, 1982). The errors on this estimate of the position are, according to our minimisation technique, $\pm 1.5''$, and the astrometry is accurate to within ~ 1 arcsecs. There are, however, additional uncertainties due to the fact that the pattern of polarisation vectors is not perfectly circular near the source. This distortion of the circular pattern tends to displace the estimate source position somewhat, especially if one side of the pattern suffers more distortion than the other, as we see here. We might therefore expect the uncertainty in our estimated source position to be $\sim 3''$.

Heckert and Zeilik (1983) presented a 2.2μ polarisation map of a $10''$ square region around the IR source. The pattern of vectors is not dissimilar to that seen in figure 6.2; these authors placed the centre of the pattern at the waist of the bipolar IR nebula mapped by Allen *et al.*, which is the position of the IR source determined by other observers at poorer resolution (Wynn-Williams, Werner and Wilson, 1974; Wynn-Williams, Becklin and Neugebauer, 1974). Heckert and Zeilik attribute the 2.2μ polarisation solely to scattering by dust close to the source which, lying in the faintest part of the IR nebula, must be obscured from direct
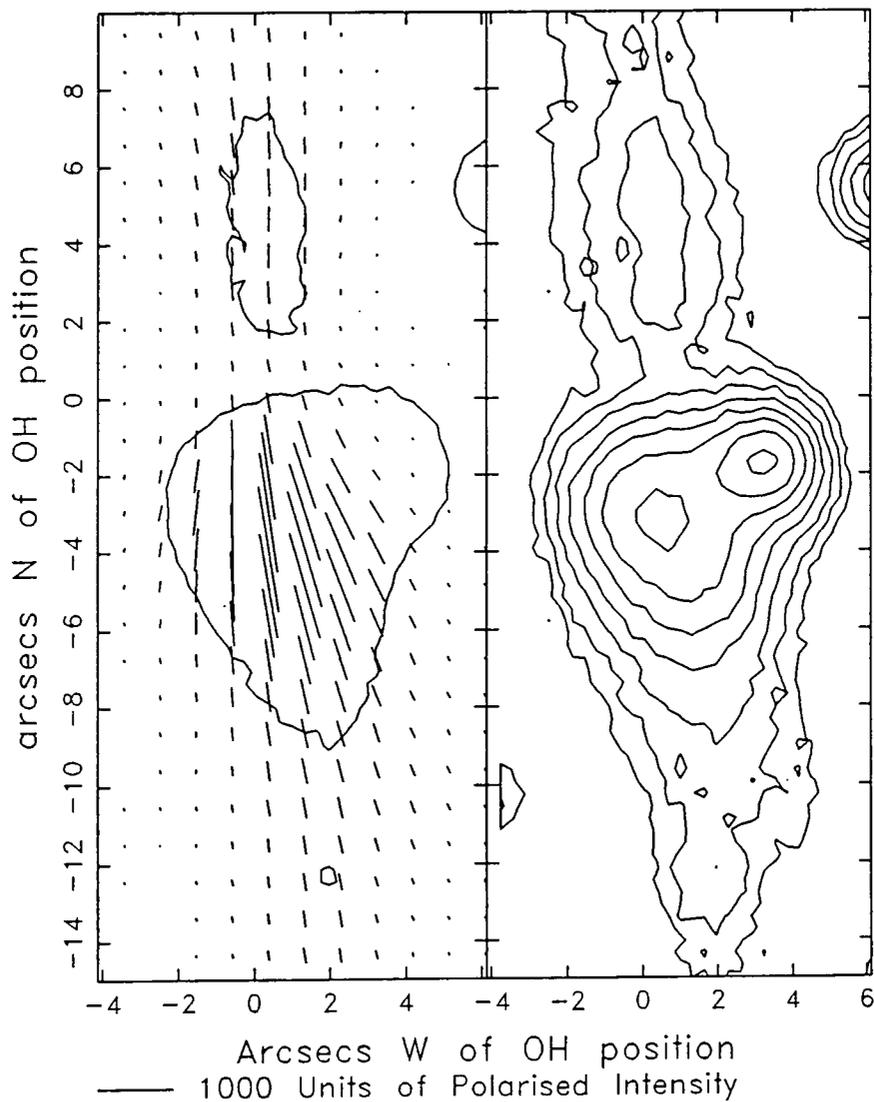
Figure 6.4: Intensity contour and polarised intensity maps of the central region of the OH 231.8+4.2 nebula. The polarised intensity vectors have been rotated by 90°, so that for a simple reflection nebula they point to the position of the illuminating source.

offset from $7^h39^m58\overset{s}{.}9\ -14°35'43\overset{''}{.}4$			uncertainty	references
Centre of OH emission	$0''$E	$0''$N	$0.2''$	a,b
SiO$_2$ maximum	$1.5''$E	$2.4''$N	$3''$	c
IR position: 2.2μ	$0''$E	$0.6''$N	$4''$	d
20μ	$0''$E	$0.6''$N	$4''$	a
IRAS	$4.3''$E	$1.4''$N	$6''$	e
Centre of polarisation pattern	$0''$E	$2.1''$N	$\sim 3''$	f

Table 6.1: The positions of sources close to OH 231.8+4.2. References: a. Wynn-Williams, Werner & Wilson (1974), b. Morris, Bowers & Turner (1982), c. Jackson & Nguyen-Quang-Rieu (1988), d. Wynn-Williams, Becklin & Neugebauer (1974), e. IRAS point source catalogue, f. This work.

view.

The relative positions of the star at the centre of the OH 231.8+4.2 system, as determined by various investigators using a number of different techniques, are shown in table 6.1. The uncertainty in most cases is considerable, and the table gives no justification for proposing that the OH, IR, SiO$_2$ and optical sources are anything other than a single centre of activity—an M9III star as suggested by Cohen (1981).

6.5   The geometry of the OH 231.8+4.2 nebula

The generally accepted model for the OH 231.8+4.2 system, as deduced from observations made at different wavelengths using a variety of techniques, has a centrally placed giant star surrounded by an extensive disc of gas and dust which totally obscures the star at optical wavelengths. The central M9 star is the source of OH and IR emission and is continuing to evolve, expelling matter from its surface as it does so. This outflow is channelled by the circumstellar disc which causes it to form a pair of partially evacuated cavities in the surrounding medium. The walls of the cavities are seen by shock excited emission as the outflow material interacts with the ambient medium; this is likely to consist of the extensive RGE created in

an earlier phase of the object's evolution.

The polarisation measurements presented here permit refinements and additions to be made to this model. The edges of the cavities cannot be investigated since they lie outside the observed region, but the filaments in the axial regions of the nebula and the circumstellar disc regions can be examined more closely.

6.5.1 The circumstellar disc

The OH 231.8+4.2 complex, in common with many other bipolar nebulae, whether illuminated by pre- or post-MS stars, has a reflection nebula illuminated by a star that is obscured from direct view at visible wavelengths, and possibly at NIR wavelengths as well. It is clear then that some material surrounds the source in such a way as to prevent it from being seen directly but at the same time allowing radiation to escape in the direction of the axis of the nebula, in order to illuminate the lobes to the north and south. The presence of cold absorbing material close to the central star is also indicted by the spectra obtained by Gillett and Soifer (1976), and Soifer *et al.* (1981). It seems likely, and has been assumed in much of the literature, that OH 231.8+4.2 is surrounded by a dense optically thick disc of dust, so that radiation can only escape from the star along the axes of the disc.

Further evidence for such a disc is seen in the distortion of the centrosymmetric pattern of polarisation vectors in figure 6.2. A band of parallel vectors running across the source of scattered light is known as a "polarisation disc" (see Scarrott, Gledhill & Rolph, 1990), and a standard interpretation for this kind of effect is that elongated dust grains aligned by a magnetic field in the plane of a circumstellar disc polarise the light passing through the disc by dichroic extinction. This could be tested by further polarisation measurements over a wide wavelength range to see if the wavelength dependence fits the empirical Serkowski law (Serkowski *et al.* 1975). In front of the source, then, we would expect to see the polarisation vectors lying parallel to the major axis of the disc projected onto the plane of the sky. The orientation of the disc around OH 231.8+4.2 can be inferred from the PA of

the polarisation measured at the source position; at ~98° this is perpendicular to the axis of the nebula, which has a PA of ~7°. This arrangement is precisely what we might expect if the disc only allows radiation to escape along the directions of its axis to produce the reflection nebulosity.

The influence of the disc on the otherwise centrosymmetric pattern of vectors caused by simple scattering appears in figure 6.2 to extend at least 5″ to the north and south of the source position. This is in agreement with the spatial extent of the disc estimated from the IR colours by Woodward *et al.* (1989). These authors showed that the total thickness of the disc is ~10″, with very high optical depth in the central 4″and the polarisation data show that there appears to be an ordered magnetic field throughout this region.

6.5.2   The axial filaments

In figure 6.5 greyscale intensity and polarised intensity images of the axial regions of the OH 231.8+4.2 nebula are shown, together with contour maps of the same images. It is immediately apparent that several knot-like features in the intensity image are absent from the polarised intensity image, showing that they are seen in unpolarised light. The brightest of these are probably field stars; others may be emission line objects such as shock regions or HH-type objects (see section 6.5.3).

The wiggly filamentary feature which is common to both intensity and polarised intensity images is seen to extend ~ 13″ north and ~ 35″ south of the source position, which is marked with a circle whose size represents the positional uncertainty of the centre of the polarisation pattern. The filaments extend in each direction from the source to the furthest point on the walls of the cavity, and are seen by reflected light as the polarised intensity image shows.

Given that there are partially evacuated cavities in the RGE to the north and south of the OH/IR source, then the filamentary structures appear to be enhancements in the density of material within the cavities; concentrations of dust grains constrained to a narrow path which lies approximately along the axis of the
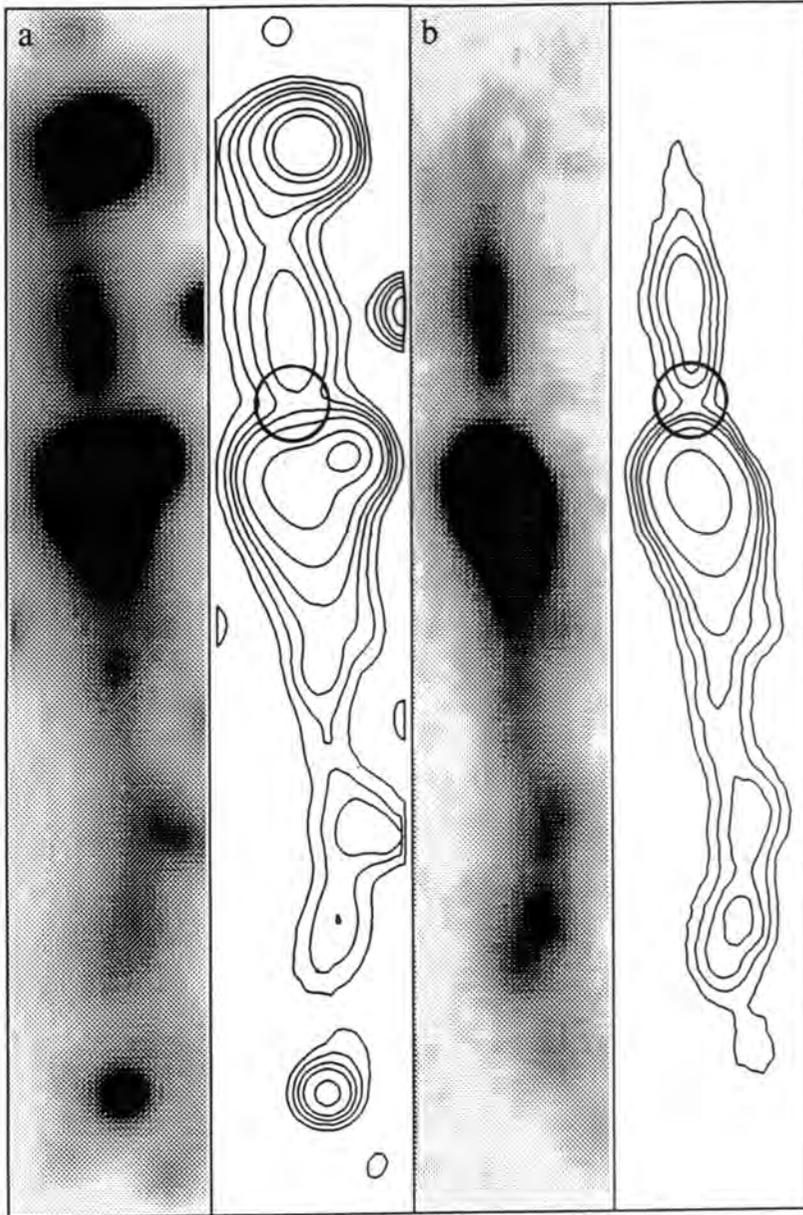
Figure 6.5: Greyscale images and contour maps of the OH 231.8+4.2 nebula seen in total intensity (**a**), and polarised intensity (**b**). Unpolarised features are absent from the polarised intensity image.

partially evacuated lobes. These dust grains are seen by light reflected from the
central star, creating the polarised reflection nebula seen at optical wavelengths.
The matter within the filaments has presumably been ejected from the OH/IR
source at some stage, possibly in discrete outbursts, and is probably still moving
away from it. Since the dusty filaments extend to the furthest edges of the evac-
uated cavities they may be at least partially responsible for the excitation of the
bow shocks at the extremities of the nebula.

6.5.3   The proposed HH objects

Cohen *et al.* (1985) detected two extended areas of nebulosity seen in line emission
at the extremities of the lobes of the reflection nebula, 13″ north and 35″ south
of the OH/IR source. These two regions have HH-type spectra, normally seen in
pre-MS objects. Reipurth (1987) identified bow shocks to the north and south
of OH 231.8+4.2 at the positions of the proposed HH objects; the northern one
has a smooth profile but in the southern bow shock three distinct knots can be
distinguished, with a fourth just outside the main shock region.

Since the observations of OH 231.8+4.2 presented here were made without a
filter, spectral features arising from both continuum and line emission should be
present in the intensity images, and HH objects should therefore be visible. A high
number of field stars confuses the total intensity image of figure 6.5 however, so
that the only HH knot which can be clearly distinguished is that lying outside the
region of the southern bow shock. A bright field star lies very close to the north-
ern shock rendering it invisible in our image, although the contours do indicate
some nebulosity just to the north of the star. Of the three knots in the southern
bow shock, one is outside the area covered by our observations, one is virtually
coincident with a bright star, and the other is very close to the same star.

Although both line emission and continuum light is recorded in the intensity
image, the polarised intensity image is devoid of features seen by emission rather
than reflection since such features are by their very nature unpolarised. The south-

ernmost HH knot, which can be clearly seen in the intensity image of figure 6.5 just to the south of the bright star, is notably absent from the corresponding polarised intensity image, which is confirmation that it is seen in emission line radiation intrinsic to the knot itself. Intensity profiles through the knot show that it has a non-stellar shape and is not therefore a foreground star. Although the other proposed HH knots cannot be distinguished in the intensity image they would be visible in the polarised intensity image if they were at all polarised since in this image the field stars are absent. The HH objects are not seen, however, which is an indication that they are not clumps of scattering particles but are seen by radiation which originates within the knots themselves.

Images of OH 231.8+4.2 the H and K wavebands made by Woodward *et al.* are not confused by the field stars seen at optical wavelengths, and they show that the northern bow shock is redder than might be expected for an HH object. Woodward *et al.* attribute this red colour to multiple scattering by a region of high density dust at the interface of the shock with the surrounding material.

6.5.4 The tilt of the nebula

There are a number of observations which indicate that the axis of the OH 231.8+4.2 nebula is tilted out of the plane of the sky. Morris *et al.* (1982) measured OH outflow velocities which showed that the northern lobe is tilted towards us and is closer than the southern one, although the optical appearance of the nebula suggests that the fainter northern lobe is more obscured and therefore tilted away from us. Velocity measurements derived from optical spectra of the proposed HH objects by Cohen *et al.* (1985) and independently by Reipurth (1987) suggest that the northern lobe is the nearer, confirming the interpretation of Morris *et al.*. Reipurth quotes a tilt of 47° out of the plane of the sky.

In the optical polarisation data the influence of the polarisation disc is stronger to the north of the central star than it is to the south. This would normally lead us to conclude that the northern lobe points away from us and is seen through

the circumstellar disc, whilst the southern lobe is seen in front of the disc. If the tilt derived from outflow and spectroscopic observations is accepted however, this cannot be the case, and we have to assume that the obscuring material lying in front of the inner parts of the nebula is distributed in an unusual fashion, being more dense to the north of the star than to the south. Such is the conclusion of Woodward et al. (1989), whose measurements of the relative colours of the northern and southern lobes show that, apart from a small region very close to the central star, the southern lobe is redder and therefore more obscured. The small region of the nebula in which the northern lobe is redder corresponds to the area 2–5″ N of the source in which the effects of the circumstellar disc are seen most clearly in the polarisation data, and is attributed by Woodward et al. to an enhanced density of dust grains in this region of the disc. The southern lobe is thought to be brighter than the northern one simply because it contains a higher density of scattering centres.

6.6 The nature of the scattering particles

The observed levels of polarisation allow an estimate of the effective grain size to be made since, as section 5.4.2 showed, there is a maximum polarisation that can be produced by grains of any given size distribution. In the case of OH 231.8+4.2 the maximum observed polarisation, which any model of the scattering particles must account for, is $\sim 40\%$. If we assume initially that the scattering centres are Rayleigh particles then this limits the scattering angle, θ, to $49° < \theta < 131°$. If scattering takes place only along the axis of the nebula (i.e. in the filaments) then in order for θ to lie in this range the tilt of the nebula out of the plane of the sky has to be $\leq 41°$. This maximum value of the inclination of the nebula is close to the tilt quoted by Reipurth, and produces 40% polarisation irrespective of the direction of tilt. For an inclination of $> 41°$ there is no particle size distribution that can produce a polarisation of 40%.

If the scattering particles were larger, so that they no longer fall within the

Rayleigh regime, then Mie theory must be used to calculate the levels of polarisation that could be produced by a given size distribution. Mie particles with a power law size distribution $N(a) = a^{-n}$ with a silicate refractive index require $n \gtrsim 4.3$ to produce polarisation levels of 40%, even at scattering angles of 90° (i.e. zero tilt). This corresponds to an effective particle size of $\lesssim 0.2\mu$. If any tilt is introduced the effective grain size must be reduced to produce 40% polarisation. Ice crystals (refractive index $= 1.33$) with a similar power law size distribution would require an index $n \geq 3.0$ to produce levels of polarisation as high as 40% at 90° scattering angles; this corresponds to an effective particle size of 0.6μ. These particle sizes are not dissimilar to those required by the scattering model of Heckert and Smith (1988) and it is clear that if the nebula is indeed inclined by $\sim 47°$ to the plane of the sky the silicate grains at least must approximate to Rayleigh particles. They are therefore smaller than those found in the ISM or in reflection nebulae associated with YSOs.

This estimate of the grain size, based entirely on the polarising properties of the dust grains in the nebula, is not inconsistent with the results of Woodward *et al.* (1989). These authors showed that although the nebula is seen predominantly by scattering at NIR wavelengths and that no emission is seen from grains in thermal equilibrium, any emission from transiently heated ultrasmall grains cannot be ruled out. This transient heating process has been described by Sellgren (1984): very small grains ($\sim 0.1\mu$), briefly heated to $\gtrsim 600K$ by individual photons, radiate thermally at NIR wavelengths. It is possible that the very small grains which the polarisation data have shown to be present could give rise to such NIR emission, and indeed Heckert and Zeilik (1981) measured constant levels of polarisation in the J, H and K wavebands, but found a significant decrease in polarisation in the L waveband. This is indicative of an emission process at these wavelengths, and provides some evidence for Sellgren emission by small grains.

The atmospheres of evolving red giant stars are thought to be the source of dust grains which ultimately become a component of the ISM. If the grains have only

recently condensed around OH 231.8+4.2 they might be expected to be smaller than those in the ISM, and to have a different size distribution. Whittet (1989) attributed IR features in the spectrum of OH 231.8+4.2 to H_2O frost on silicate cores; it is possible that the small grains which cause the high levels of polarisation in the nebula are the silicate cores themselves, and that frost on some of these cores could also contribute to the observed polarisation.

A further point of note which arises if the nebular grains act as Rayleigh particles is that the scattering cross-section for Rayleigh particles is symmetric about 90°. This means that for scattering by small grains the two lobes of the nebula will be equally bright, whatever the inclination to the line of sight, assuming they contain the same density of scattering centres and neither is more obscured than the other. Our observation that the northern lobe is the fainter of the two therefore suggests that either it is more obscured than the southern lobe, which is refuted for the most part by the NIR colours, or more likely that it contains fewer scattering particles. This tends to suggest that the effect of outflow activity to the south of OH 231.8+4.2 is greater than to the north of it. The relative sizes of the cavities seen in Reipurth's narrow band image lend credence to this suggestion; perhaps the irregular distribution of dust within the disc, with a greater density to the north than to the south, inhibits activity in this direction.

6.7 The evolutionary state of the OH 231.8+4.2 system

It is clear that OH 231.8+4.2 is at an evolutionary stage similar to that of IRAS 07131-0147. The fact that the filaments can be seen so close to the OH/IR source and that the edges of the cavities are seen by emission line radiation, however, shows that in the case of OH 231.8+4.2 mass loss is still occurring, and that IRAS 07131-0147 is therefore the more highly evolved of the two objects. OH 231.8+4.2 seems to be losing mass via the so-called fast wind, the slow wind having produced the extended RGE and now ceased. The fast wind is obviously

not isotropic, but has a bipolar form similar to the shape of other protoplanetary nebulae (e.g. GL2688, M2-9, GL618). In this case however the bipolar structure is not symmetrical; the effectiveness of mass loss by the fast wind seems to be greater to the south of the stellar core than to the north. In addition, the mass loss within each lobe is concentrated towards a narrow axial region which results in the filamentary reflection nebula.

It is likely that the circumstellar disc is responsible for the collimation of the outflows from OH 231.8+4.2; Balick (1987) shows that portions of a circumstellar disc composed of RGE material can be evaporated by the stellar wind resulting in a flow pattern that is highly collimated, eventually forming a butterfly shaped planetary nebula. We cannot necessarily generalise to other protoplanetary nebulae, however, where bipolarity could be caused by other mechanisms such as stellar magnetic fields or nonradial pulsations (Zuckermann and Gatley, 1988).

6.8 Conclusions

OH 231.8+4.2 is a post-MS star that has evolved off the AGB shedding its RGE by means of a slow wind, and is continuing to lose mass via an anisotropic fast wind. This wind has created a pair of spherical cavities in the extended RGE around the star, which illuminates matter flowing along the axes of the cavities producing the observed optical reflection nebulosity. The star itself is totally obscured from direct view at optical wavelengths; the polarisation maps provide evidence of a circumstellar disc of dust with an ordered magnetic field, but show that the distribution of material throughout the disc is far from uniform, being more densely concentrated to the north of the star.

The grains comprising the dense axial regions of the optical nebula have been shown to be much smaller than those of the ISM, or those around YSOs, so that Rayleigh scattering occurs. It is possible that these small grains emit NIR radiation by the Sellgren process, and are silicate cores, precursors to the ice covered grains which are known to exist around the star.

It has been shown that at least one of the proposed HH objects is not seen by reflected radiation which confirms that it is seen by its own intrinsic emission, probably shock excited.

Chapter 7

Summary and conclusions

The work in the preceding chapters can be conveniently divided into three sections: instrument design and control; the study of pre-MS objects; and the study of post-MS objects. In this final chapter the results of each section are summarised, and fresh conclusions are drawn from an intercomparison of the pre- and post-main sequence results.

7.1 The polarimeter and CCD camera

The mechanical construction and principles of operation of an automated imaging polarimeter controlled by an Apple II computer have been described, bringing the documentation of the Durham instrument up to date, and providing a reference for its users. A detailed account has also been given of the CCD camera system based on an Elonex PC which is currently used in conjunction with the Durham Imaging Polarimeter.

Although the optical layout of the polarimeter is almost identical to that of the first Durham polarimeter, built over 15 years ago, the modifications which have been made in order to permit remote operation of the instrument now give the observer a freedom and flexibility that was not possible with previous models, and have as a result made observing with this instrument easier and more comfortable. There is now rarely any need for anyone to work in the telescope dome whilst ob-

servations are being made, and at most sites it is possible to situate the Apple II and Elonex PC in the telescope control room, thereby enabling both the telescope and instruments to be controlled from a single location. This can mean that fewer people are required on an observing run, and obviously alleviates the communications problems which can otherwise arise between the telescope operator and observer.

The coated GEC CCD which has been used as a detector with the automated polarimeter permits observations to be made throughout the BVRIZ wavebands. The PC used to control the CCD has advantages over the original computer, being much lighter and easier to transport, and eliminates the need for an external disc drive and frame store. The software which enables instructions to be given using a mouse and graphics tablet provides a friendly interface between the PC and observer, giving him full control over the CCD and relieving him of the need to know complex command structures and syntax.

Together the automated polarimeter and PC-based CCD camera have eased the pain of long observing runs, and have proved to be a fast and reliable system for measuring the polarisation of extended astronomical objects. This is demonstrated by the wealth of publications based on results obtained using this arrangement at various observing sites around the world (see appendix B for some examples).

It is hoped that eventually a single computer will replace the Apple II and Elonex PC. A second automated polarimeter employing the operational principles described here is already under construction; this new instrument will be controlled by an Elonex PC instead of the Apple. It is envisaged that the programmes for both CCD and polarimeter control will then be combined on the same computer, and will be executed using macros defined for the graphics tablet. This will further simplify the observing process, and cut down on the amount of hardware that needs to be transported with the polarimeter. The use of a single computer to control both instruments will also make it possible to make a series of exposures completely automatically, leaving the observer to monitor the telescope tracking

only.

It is also hoped that some preliminary data reduction might be carried out at the observing site as the data are collected—portable but powerful computers such as the recently-acquired VAXstation 3100 now make this a possibility—and it is clear that there is still further potential for the future development of what is currently a highly successful instrumental setup.

7.2 Pre-main sequence objects

It is now generally accepted that most stars pass through a period of energetic mass loss before evolving onto the main sequence. This mass loss occurs, at least in part, in the form of molecular outflows which molecular line observations have shown to be composed of cold gas moving at high velocities. Over 70% of the observed molecular outflows associated with YSOs have a bipolar morphology and of these many are collimated to a fairly high degree (Lada 1985). The mechanisms causing the collimation are not yet fully understood, but are thought to involve circumstellar discs of material and/or magnetic fields around the stellar cores. At optical wavelengths the insides of the cavities excavated in dark clouds by the molecular outflows are often seen by reflection; these are usually bipolar and may contain optical jets and HH objects (although not all HH objects and jets are associated with molecular outflows). The optical outflow features tend to be aligned with the magnetic field direction of the parent cloud, which suggests that it might play an important part in the initial collapse of the cloud fragment and in the formation of the protostar and circumstellar disc. IR excesses are often seen in the direction of protostellar objects; these are thought to be caused by absorption of visible light by dust around the source which then re-emits the radiation at infrared wavelengths.

It is immediately apparent that the two young objects studied here, HH83/Re17 and GL2591, have many of the characteristics of star formation associated with them. Neither of the nebulae have a primary illuminating source which can be

directly detected at optical wavelengths, but both illuminators can be clearly seen at IR wavelengths, which is an indication of heavy obscuration around the source. Both of these objects are associated with a dark molecular cloud and in each case the nebula appears to be seen as a result of radiation from the IRS illuminating material inside a cavity within the dark cloud. The cavities indicate the presence of some outflow mechanism, and there is evidence in both examples that the outflows have a bipolar structure. A large molecular disc is known to exist around each of the sources; the visible reflection nebulae are centred on the axes of the discs. The systems are both tilted so that only the nearer of the two cavities created by the bipolar outflow can be seen, the other lying hidden behind the optically thick disc.

There are however differences between the two systems: HH83/Re17 has a jet seen in the emission lines characteristic of HH objects, which terminates in bow shocks on either side of the source. GL2591 has associated with it at least one HII region, and a source of H_2O maser emission, but although it has been suggested that there are HH objects associated with GL2591 there is no evidence for these in the data presented here. A less obvious difference is that for HH83/Re17 the visible reflection nebula is caused by light from the IRS reflecting off the walls of the cavity in the dark cloud, whilst in the case of GL2591 the nebula appears to be caused by reflection off clumps of material lying within the outflow cavity, the walls of which are not seen. This tends to suggest that mass loss has, at least for some of the time, been intermittent, and also that the cavity close to GL2591 is less well defined, which may be an indication that it is the older of the two systems.

It is clear that both of the young objects investigated here are fairly typical of regions of energetic star formation. Imaging polarimetry has been used to identify the position of the illuminating source of each nebula, which is not necessarily obvious from the shape of the nebulosity (although in the case of HH83/Re17 the jet does give an indication of the direction in which the source lies). The

polarimetric data have helped to show which particular characteristics of star formation are present in each system, and in conjunction with the results of work by other investigators they have enabled simple models of the two complexes to be visualised.

7.3 Post-main sequence objects

The evolution of stars off the main sequence and onto the AGB is relatively straightforward and well understood, but immediate post-AGB evolution is less easily explained. This is due in part to the fact that stars terminate their lives in different ways according to their masses, but also to the extremely short evolutionary period between the AGB and planetary nebula stages (~ 1000 years). There are therefore relatively few examples of this class of object available for study.

It is thought that as a star of intermediate mass evolves on the AGB it becomes a Mira variable and loses mass isotropically at a fairly low rate, depositing the ejected material in an extended RGE. Towards the end of AGB evolution mass loss becomes more rapid as a fast wind removes the last vestiges of excess material from the stellar core, which remains and probably becomes a white dwarf. This core eventually ionises the remains of the RGE to produce a planetary nebula.

The two post-MS objects studied here, OH 231.8+4.2 and IRAS 07131−0147, both appear to have undergone mass loss by the dense slow wind and have already moved off the AGB. The nebulae associated with the central stars are not at first sight similar, but it has been shown that both are related to cavities blown in the extended RGE by the fast wind. In the case of OH 231.8+4.2, where the edges of the cavity are seen by shock-excited emission, the fast wind is still blowing, but the polarimetric data show that IRAS 07131−0147 is at a slightly later evolutionary stage, the fast wind having ceased, although ionisation of the RGE does not appear to have begun yet.

The results presented in this work demonstrate that in these cases the dense fast wind is not isotropic, but is collimated to some degree and in both instances is

bipolar. Many planetary nebulae exhibit a bipolar dumbbell or butterfly (bow-tie) structure which is thought to arise as a result of a collimated fast wind, and the observations presented here add weight to this theory. The collimation mechanism is not well understood, but it has been shown that for OH 231.8+4.2 at least, there is a circumstellar disc whose axis is parallel to the flow direction of the fast wind, and which probably contains a well ordered magnetic field within it. The link between the disc and the collimation of the fast wind is not clear, but on a very simple level it is likely that the disc prevents the fast wind from carrying material in the direction of its plane, so the predominant outflow direction is along the axis of the disc.

The dust grains in the nebulae around the post-AGB stars have been shown to be very small, assuming that they are silicates which seems likely, and act as Rayleigh particles. The grains are probably freshly condensed in the extended RGEs and could act as condensation nuclei which are required for the formation of larger grains. This shows that in principle it would be possible for the envelopes of red giant stars to be the birthplace of one component of the ISM grain population, as current theories of ISM formation commonly assume.

7.4   Pre- and post-MS objects: a comparison

In presenting observations of star formation regions side by side with those of post-AGB systems it has become apparent that the two evolutionary stages share a number of common features. Although they arise by different means it is of some value to briefly compare those characteristics which apparently link objects at opposite ends of their evolutionary tracks.

7.4.1   Collimated outflows

It is now widely recognised that outflow mechanisms operate in both pre- and post-MS evolution; mass is lost via molecular outflows and stellar winds from YSOs, and via the fast and slow winds from AGB stars. The majority of outflows from

YSOs are known to have a bipolar structure, and the large number of butterfly-shaped planetary nebulae suggests that mass loss from evolved stars has a similar propensity to be bipolar in nature. Although it was once thought that outflows were characteristic only of early evolution of massive stars it is now known that such activity can also be an indication of low mass star formation, and that it represents an important stage of pre-MS evolution for stars of all masses. Similarly with AGB evolution; the ejection of the RGE represents a stage which all stars of intermediate to high mass are likely to go through, although it is thought that bipolarity of the fast wind which follows is more likely to occur if the progenitor MS star is of high mass (Zuckermann and Gatley, 1988). The fast wind from an evolved object seems to be most directly comparable with outflows from young stellar systems, the slow wind which is responsible for the ejection of the RGE having no real pre-MS parallel.

The time scales over which pre- and post-MS mass loss occurs are radically different; $\sim 10^5$ years for young stars and only $\sim 10^3$ years for stars evolving off the AGB. As a consequence of this, and of the difference in density between the two types of outflow, the amount of material carried by the outflows is much greater in the case of young stellar systems, typically $10-100 M_\odot$ (Lada, 1985) compared with $< 1 M_\odot$ for evolved systems (Bujarrabal *et al.*, 1988).

In this work it has been demonstrated that the winds carrying material away from the central stars are usually responsible for creating cavities in the ambient material; in the dark cloud material surrounding a YSO and in the extended RGE around the degenerate core of a highly evolved star. The insides of the cavities are then seen by reflection. It has also been shown that in some instances (as in the case of IRAS 07131-0147 and GL2591) there is evidence that mass is sometimes lost in discrete episodes, in both pre- and post-MS systems.

7.4.2 Circumstellar discs

Probably the most interesting question that arises from the similarity of the outflows from pre- and post-MS objects has to do with the collimating mechanism: is it the same in each case? It has been shown that circumstellar discs are seen around both young stars and more highly evolved stars, and it is likely that they play a major part in collimating the outflows of these objects.

The origin of the discs

The origin of the circumstellar discs is different for the two classes of object. In the case of star formation regions the disc forms as a fragment of the molecular cloud contracts and collapses. Collapse tends to occur along the field lines so a flattened distribution of matter results; an accretion disc with a protostar at its centre. Material will be lost from the disc as it falls onto the surface of the protostar, and also by a process of erosion as the stellar wind carries matter away from the system. It is thought, however, that in the case of high mass star formation stellar evolution begins (i.e. the star joins the MS) before the disc has completely dissipated, so ZAMS stars which still have circumstellar discs could be commonplace. β-Pictoris is a well-known example of a young MS star with a circumstellar disc of dust, and it has been suggested (Smith and Terrile, 1984) that there are many other older MS stars with similar discs.

The discs surrounding post-MS stars are less well understood but a model has been proposed whereby the rapid rotation of some stars causes the density of the stellar wind to be considerably greater in equatorial regions that it is in the direction of the poles. When the RGE is ejected then, it may well contain within it a dense equatorial region that could be classed as a disc if the density gradient is high. This disc will collimate the fast wind in a simple mechanical fashion, the efficiency of the collimation decreasing as the centre of the disc is gradually eroded away. Magnetic fields and nonradial pulsations may also play a part in the formation of discs within the RGE and the collimation of the fast wind.

Magnetic fields in discs

Many models for collimation mechanisms require magnetic fields to be present in circumstellar discs of dusty material (see for example the paper by Uchida and Shibata, 1985), and it has been seen that there is some evidence for these in the discs surrounding objects at both ends of the evolutionary track. The magnetic fields that are often seen within the circumstellar discs of young objects are thought to be the remains of the magnetic field of the parent molecular cloud that has been "frozen" in the material as it collapsed. Collapse along the field lines supporting the cloud results in an oblate spheroid, and rotation of this, which may be required to conserve the angular momentum of the cloud, will wind up the field within it and cause magnetic braking. There is therefore a tendency for discs to be aligned with their axes parallel to the local field direction, and to contain a magnetic field which lies parallel to that direction, as we have already noted and as the observations demonstrate.

The magnetic field seen in the discs around evolved stars must have been present in the RGE material before it was ejected, i.e. in the stellar atmosphere. It is well known that the magnetic fields around MS stars have large scale structures which are typically poloidal and have no known toroidal component which could cause a field in the plane of a disc. It is thought, however, that stars similar to the sun have a toroidal field in the material just below their surface, and this might be the precursor to the fields which we see in the planes of circumstellar discs. In addition if an MS star has a field whose axis does not coincide with the axis of rotation this will have a toroidal component which could result in a planar field around the star when it leaves the AGB. Since so little is really known about the mechanics of the formation of post-MS circumstellar discs these theories can only hope to give some vague indication of how toroidal magnetic fields might arise in the discs.

7.4.3   HH objects

HH objects are usually associated with regions of energetic star formation, but since they are caused by material in rapid motion interacting with stationary or more slowly moving material, there is no reason why they should not be expected wherever energetic mass loss is occurring within some surrounding stationary medium. The work presented in the preceding chapters has shown how the action of the fast wind from an evolved star carves out a pair of cavities in the RGE surrounding it, and it should come as no surprise to find that HH objects are associated with at least one such star. The polarisation data for HH83/Re17 and OH 231.8+4.2 show that there are compact regions within each nebula that are seen by emission, and their spectra are apparently typical of those of shock-excited HH knots.

7.4.4   Jets

Long, narrow jet-like features are often seen in nebulae associated with star formation, and occasionally in the nebulae surrounding post-AGB stars as well. Some of these are not strictly jets but are merely filamentary structures or the effects of projection on observations of a cavity wall (see Cantó $et\,al.$,1986). In the cases of HH83/Re17 and OH 231.8+4.2 long filamentary structures are seen on the axes of the nebulae; the former is seen in emission and the latter by reflection. Both structures terminate in bow shocks which is indirect evidence of their high velocities.

The elongated structure seen running across the centre of HH83/Re17 is undoubtedly a jet of shock-excited gas ejected by the protostar. The structure seen on the axis of the OH 231.8+4.2 nebula consists of dusty material, again ejected by the central star which also illuminates it, rendering it visible. Although the physical composition of the material is different for the two systems, they are both characterised by their high degree of collimation—both are extremely narrow structures confined to a path with apparently parallel boundaries—and also

by their length—both structures extend from the central star to the edge of the cavity. The mechanism which maintains such a fine thread of material over so long a distance is not known in either case, but in common with the collimation of the rest of the outflow material it is likely that the process is similar for the two objects, probably involving magnetic fields and dense dusty discs or toroids close to the central star.

7.5 Conclusions

It is evident that at optical wavelengths pre-MS nebulae bear more than a passing resemblance to more highly evolved structures. Nebulae around stars at opposite ends of their lives seem to be characterised by the same features—dusty knots, jets, cavities, outflows and circumstellar discs—so that spectral information is required if their evolutionary status is to be accurately determined (Cohen, 1983, notes that pre-MS objects have amorphous and ragged structures whilst highly evolved nebulae are more symmetrical, but attempting to differentiate between objects on the basis of this difference would be extremely subjective). Whilst the processes causing these characteristics are not necessarily the same the resulting structures show a remarkable similarity which indicates an unexpected uniformity of morphology throughout the stellar life cycle. Additional observations of post-AGB stars are required to confirm the similarities between these and much younger objects, and as our understanding of the relationship deepens it might become possible for observations of stars at one end of their life to give some insight into the processes which occur at the opposite end of the evolutionary track.

7.6 Final remarks

It has been shown that the spatial information which imaging polarimetry makes available is an important tool which can be used to investigate the geometry of reflection nebulae, and to give us an indication of the nature of the scattering par-

ticles. This work has drawn upon the results and conclusions of a number of other investigators in the field, working at different wavelengths and using different investigative techniques, which has aided the interpretation of the polarimetric data so that a linear polarisation map can yield far more information than a superficial estimate of the location of the illuminating source. Advances in instrument design and detector technology have ensured that the rate of data collection has increased monotonically, and it is hoped that further automation of the Durham Imaging Polarimeter will cause this trend to continue. The comparison of pre- and post-main sequence nebulae has revealed a number of parallels between the two classes of object, and further investigations into their similarities should prove interesting and increase our understanding of the complex series of changes that are involved in stellar evolution.

Appendices

Appendix A

The DUPCAT system

This appendix contains the manual which was written by the author to aid observers using the DUPCAT system. It includes detailed descriptions of all the macros used when observing and explains how to use the PC and its peripherals. A brief summary can be found in chapter 2.

A.1 Introduction

The DUPCAT system is based on DORADO, which has been used to obtain CCD images and store them on the hard disc of a Nova computer, subsequently downloading them to magnetic tapes to be read later using the Vax in Durham. DUPCAT incorporates most of the features of Dorado, plus several additional features which allow a limited amount of image processing to be performed at the observing site. The system is based on the Imager program produced by Astromed, utilising Imager commands which are of a Unix format, and the Astromed Imager manual should therefore be studied before attempting to use DUPCAT in order to gain a more thorough understanding of the system. The main advantage of DUPCAT over Dorado is that it runs on a PC-AT which is considerably lighter and easier to transport than the old Nova. The PC contains an integral hard disc on which the data is temporarily stored, and can be linked either to a Cipher magnetic tape drive or to an Archive tape streamer in order to write the data to tape for easy and safe transportation back to Durham. There is space on the hard disc for 70 images which is usually enough for one night's observing, so the data can all be written to tape at the end of the night if required, although the system will always attempt to write each frame to tape as it is taken.

DUPCAT makes use of a Summagraphics Summasketch graphics tablet which permits operations to be carried out at the touch of a button. The tablet can be used to execute most of the procedures which will be required when running the CCD in conjunction with the Durham polarimeter, but the keyboard is still required for inputting exposure times etc. This makes the system simple to use and requires virtually no knowledge of Unix whatsoever.

For the user with a knowledge of Unix and also of C source code there exists a facility to allow user-written image processing functions to be linked to the Imager program. At present there are no compiled image processing extensions but some may be introduced in future updates.

A.2 Getting started

A.2.1 Setting up the hardware

When the equipment is unpacked it should be ready to use, after connecting a few cables. The PC, communications box and Cipher tape drive (if used) all travel in a purpose-built case, which serves as a convenient method of holding them while observing, and also of minimising the number of cables which the user has to deal with, since connections between these three devices need not be removed in order to travel. Figure A.1 shows the rear views of the hardware devices and their connections. The cables and their corresponding sockets on the various devices are labelled as follows:

A Coaxial cable connecting the communications box to the electronics rack which is bolted to the side of the polarimeter.

C Short bunch of cables between the PC and the communications box. This should only be unplugged if the PC has to be removed from the case. Note the left and right labelling.

G Cable to the graphics tablet. Note that the tablet has its own power supply unit which is also housed in the PC case; although the connections to this need not be undone the plugs often fall out in transit and should therefore be checked on arrival at the observing site.

I Image display cable. The two ends of this cable are marked computer and monitor; they are *not* interchangeable.

K Keyboard lead. The PC case contains a short extension from this socket, allowing the keyboard to be plugged in to the front panel of the case, which is often more convenient.

M Lead to the text monitor. This also has an extension to the front panel of the PC case for convenience.

Graphics tablet
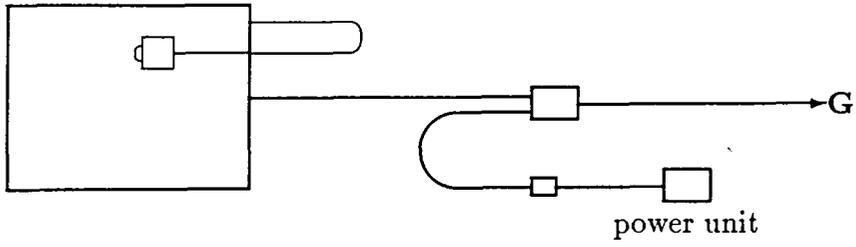
Communications box
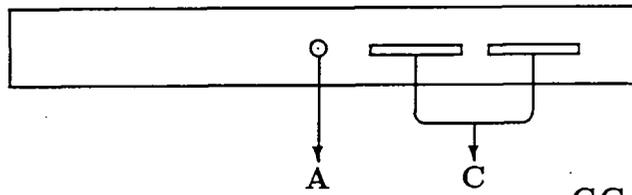
Computer
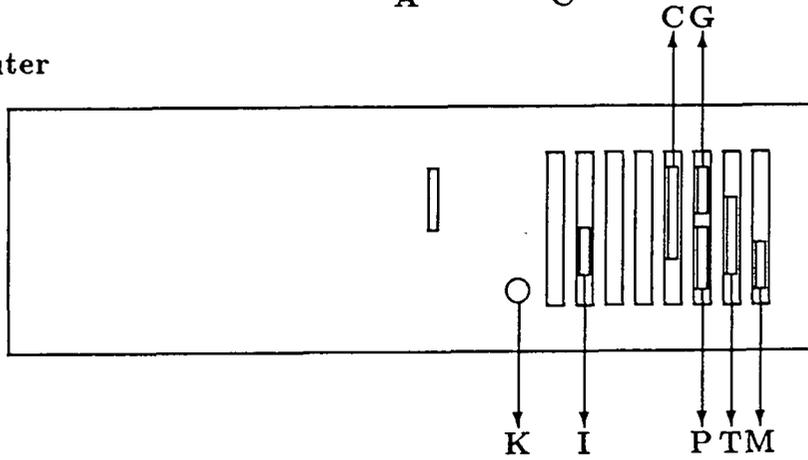
Tape units
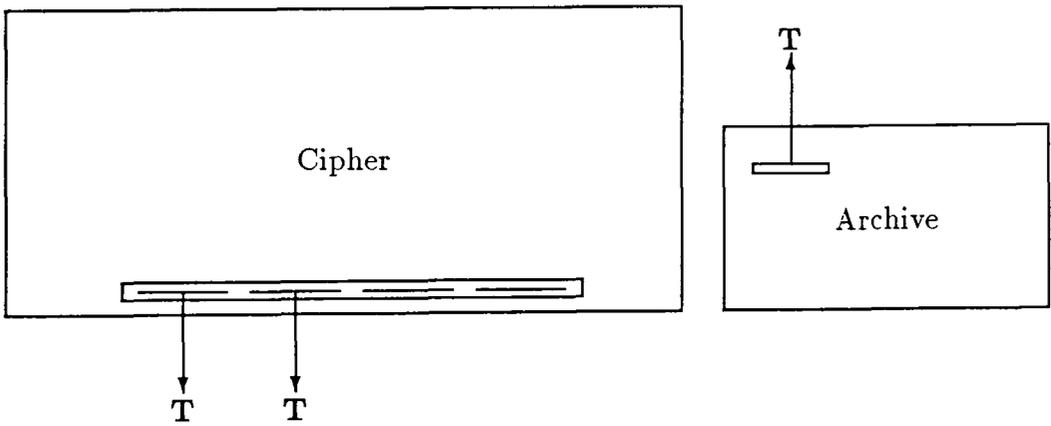
Figure A.1: Hardware connections for the DUPCAT system.

P Parallel printer port (printer is optional). Note that the printer will not operate if the PC is booted with the `system5.ar` kernel. The spooler for the printer is not set up; in order to print out a file use the `cat >/dev/lp1` command (see Unix manual).

T Cable to the tape unit. For the Archive tape drive the card which has to be put into the PC has a socket on the back which can simply be connected to the lead to the tape unit. The Overland card, however, which is used with the Cipher tape drive, has two slots which take ribbon cables. These must be threaded through the hole in the back of the PC and connected to the card before carefully installing it in the slot on the PC's motherboard. The two cables are clearly labelled F (front) and M (middle), corresponding to the relative positions of their sockets on the card, and Left and Right at the other end. It is important that these cables are connected correctly, with the longer cable on the left-hand board of the Cipher unit. The red strip on the ribbon cable should be at the *top* on the Overland card and to the *right* on the Cipher unit.

Once the cables have all been installed the protective card should be removed from the PC's floppy disc drive before powering up.

A.2.2   Booting the system

When the PC is powered up it will prompt for the system to be booted. This will depend on which type of tape drive is installed. If the Cipher half-inch tape drive and Overland card is installed the PC must be booted with `system5`, the default. Alternatively, if the Archive tape streamer and card are installed the PC must be booted with `system5.ar`. If the PC is booted with the wrong system kernel the tape commands (see section A.3.1) will all fail, and the PC will have to be rebooted if they are to be used. When the system has booted it will prompt for a username; simply type `user` to log on.

If the menu has already been set up on the graphics tablet (see section A.2.3) the Imager environment can be entered simply by typing the appropriate command, `cipher`[1] or `archive` (dependent upon the tape drive which is installed), in response to the

```
user>
```

prompt. A symbol table will be allocated, default values for all variables will be set up, and the macros to be used by the graphics tablet defined. After displaying a warning message the system will return

```
MENU Choose a macro from the tablet menu
```

as a prompt when the initialisation process is complete and control will immediately be handed to the graphics tablet. If the wrong command was used to enter Imager use the mouse to select the **quit** macro in order to return to Unix and re-enter Imager using the correct command. Unless a blank tape is being used the **inittape** macro should be run straight away to position the tape ready for writing. If this is not done any data which already exists on the tape (e.g. from a previous night's observing) will be lost (see section A.3.3).

A.2.3 Using the graphics tablet

The graphics tablet is used to begin all DUPCAT processes, and to control the image display setup (i.e. to change grey levels etc.). It is also used in a few of the macros to define areas of an image to be analysed or to zoom in on particular regions. The tablet is quite straightforward to use and provides a quick method of running programs with the minimum of effort.

If the menu for the graphics tablet has not been aligned this must be done before entering Imager, by typing **demo** and moving the mouse across the graphics tablet. The coordinates of the cross wires of the mouse (relative to the origin of

---

[1]Note that all Unix commands are case sensitive.

the tablet) and the state of the mouse (i.e. which buttons are currently being pressed) will be echoed to the screen once every second. The origin can easily be found and the menu placed in its correct position, such that the bottom left corner coincides with the tablet origin. If the menu is positioned correctly the coordinates of the boundaries of the squares should all be divisible by 500. When the menu is in place the demo program can be terminated by hitting the delete key, or it can be allowed to continue, in which case it will terminate after 100 seconds. Note that this program is also a useful test to check that the graphics tablet is working correctly.

When the menu has been set up a macro can be executed from within the Imager environment simply by moving the cross-wires of the mouse to the relevant square on the tablet menu and pressing button 1 (yellow). Whenever a macro has been successfully completed the system will return

> >

> MENU Choose a macro from the tablet menu

All macros may be interrupted by hitting the delete key, which causes control to return to the graphics tablet once the currently executing stage of the macro has completed. It is not advisable to interrupt a macro in this way when the CCD is reading out, as only the row of pixels which is currently being read will be completed, leaving charge stored on the chip.

When the tablet is used interactively in a macro, for example to define regions of an image in **find & zoom**, definitions of the functions of the mouse buttons are always given, but they are normally so concise as to be confusing to the novice. An explanation of these definitions is given here:

reset When a macro is executed the mouse will be positioned randomly on the tablet and by default this position will be set as the origin of the image[2] in some procedures. Moving the mouse to the tablet origin and pressing this

---

[2]the tablet origin is *not* the same as the screen or image origin.

button will set the screen origin to the bottom left of the image, allowing the whole screen to be accessed by the cursor. Button 1 is defined to be reset in the **find & zoom, fastfind** and **horiz/vert profile** macros.

size This definition allows the user to "drag" the sides of a region towards or away from its centre by moving the mouse up/right or down/left respectively, thus decreasing or increasing the size of the region. The size button must be continuously depressed while dragging the boundaries of the region, and when the size has been set the region will usually be moved to the top right-hand corner of the screen, as will the image origin, so a reset will be needed to set the origin again. Button 2 is defined to be size in the **fastfind** and **find & zoom** macros.

exit This button actually executes the command (displays the zoomed image, for instance) and continues with the next procedure of the macro. Button 3 is defined to be exit (sometimes called doit) in the **fastfind, find & zoom, soft zoom** and **horiz/vert profile** macros.

exit_zoom After interactively panning an image in a zoomed state this button allows the user to leave the image zoomed and continue with further operations (see the note in section A.3.2 on hardware bugs). The reset macro redisplays the image in unzoomed mode. This definition is given to button 4 in the **hard zoom** macro.

exit_unzoom Again, after panning the image in a zoomed state this will exit to allow further operations to continue, but will return the image to the unzoomed mode. This definition will be given to button 3 in the **hard zoom** macro.

pan-in This button causes the size of the rectangular region outlined on the screen to be reduced, and moves it so that it is centred on the arrowhead cursor.

This definition is given to button 2 in **soft zoom** and results in increased magnification.

pan-out This button causes the size of the region to be increased and moves it so that it is centred on the arrowhead cursor. The maximum size which can be obtained is about half the image size, giving a magnification factor of approximately 2. Button 4 is defined to be pan-out in the **soft zoom** macro.

pan This button simply moves the outlined region so that it is centred on the cursor, without changing its size. Button 1 is defined to be pan in the **soft zoom** macro.

A.2.4 Using the tape drives

Archive tape streamer

Once the hardware has been set up the Archive tape drive is very simple to use. Cassettes should be pushed into the slot on the front of the drive with the aluminium side facing downwards. Writing will begin at the position of the tape when it is loaded, so a partially used cassette should always be rewound (using the **rewind tape** macro) and **inittape** run before any other operation is attempted. When a cassette is full it should be rewound and removed from the drive, and write-protected by turning the black screw on the top cover. Cassettes may be removed from the drive at any time (except during a read or write operation), but to be safe **rewind tape** and **inittape** should be run when they are replaced.

Cipher half-inch tape drive

To load a tape into the drive simply open the door and place a tape on the capstan. Pressing the LOAD REWIND button on the drive will cause the tape to be automatically threaded and moved to the logical beginning of tape. The light in the button will flash until the tape is loaded, and the ON-LINE button can then be used to put the device on line allowing the computer to write to it.

The WRT EN TEST light will be illuminated if the tape is write-enabled with a write-ring. Note that unless **inittape** is run when a tape is put onto the drive, data will be written from the beginning of the tape irrespective of any frames which are already on it; these will be overwritten. A tape can be rewound using the **rewind tape** macro or by pressing the LOAD REWIND button after taking the device off-line (using the ON-LINE button)—both these operations rewind to the logical beginning of tape mark and do not dismount the tape. This may be done by taking the device off-line and pressing UNLOAD, which causes the tape to be wound back onto its spool and allows it to be lifted out of the drive (when the UNLOAD light stops flashing). (See also the sections on **inittape, taperead, tapedump** and **rewind tape**).

WARNING: Do not attempt to write more than 64 frames to a half-inch tape as this will cause an error which may require a reboot of the system to rectify—see sections A.3.1 and A.4.6 for more information.

It is also possible to store images on floppy discs (see section A.3.3), but this is not to be recommended due to the limited amount of data which each disc can hold.

A.3 The tablet menu

A menu sheet is available which sits on the graphics tablet, and which should be aligned using the procedure outlined in section A.2.3. The menu shows all the available macros, which are allocated to specific regions of the tablet to enable them to be executed using the mouse. If further macros are required they may be defined using the **def** command (see Imager manual). The DUPCAT system comprises a number of macros which are tailored to suit the needs of Durham polarimeterists. They can all be conveniently accessed from the graphics tablet or, if necessary, from the keyboard, and form a self contained system for the acquisition of CCD images. The currently defined macros are listed in table A.1.

CCD control	image display	others
ccd clear	auto	delete frames
expfin	clear	discdump
expose	colour	exit
expstat	darker	floppy dump
expstop	darker×2	floppy read
fastfind	display frame	free blocks
finder	grey	horiz profile
find & zoom	hard zoom	inittape
focus	harsh	quit
shcl	harsh×2	rewind tape
shop	lighter	tapedump
testshot	lighter×2	taperead
	mock relief	vert profile
	range	
	reset	
	soft	
	soft×2	
	soft zoom	
	tpose	
	update display	

Table A.1: The macros available in the DUPCAT system.

A.3.1 CCD control

These macros give the user complete control over the CCD and shutter and are defined as follows:

ccd clear

Continually flushes charge from the CCD and periodically reads out the chip, displaying the current state after each readout sequence. Running this program during long periods when the CCD is not in use (e.g. during the day) allows observations to be made immediately, since it keeps the readout noise from the chip low and continually clears any accumulated charge.

expfin

Waits for the allotted exposure time to expire and completes the **expose** process, or finishes an exposure immediately if the exposure time has been overrun. If this is the case the actual exposure time will be calculated and entered into the database for that frame. The frame will be autoscaled and displayed, then written to disc and tape as in **expose**. Note that this macro should only be used when **expose** has been interrupted using the delete key.

expose

Makes an exposure. The shutter is first checked to ensure that it is closed, then the user is prompted for the name of the object, the duration of the exposure, and the number of the next frame to be taken (see section A.3.3 for information on the numbering of frames). The chip is cleared of any residual charge by flushing several times, and after the exposure the image is autoscaled and displayed before being automatically written to the hard disc and then to the tape. The user is prompted for **lo** and **hi** values which will be used to display all subsequent images (see section A.3.2), until the **expose** process is terminated. While the

frame is being written to tape the user will be informed as to how many files are on the tape (*not* how many have been written since the last **inittape**). When an exposure has been made and written to disc and tape, the frame number will be incremented and the user given the opportunity to change the exposure time before taking the next exposure (useful when making flat fields if the sky brightness changes rapidly). Simply hitting return causes the next **expose** process to begin immediately. It is possible to exit from the **expose** macro at this stage by hitting the delete key, which will return control to the graphics tablet. The delete key can also be used to interrupt the program once the shutter has opened (so that, for instance, previous frames can be displayed), but the exposure must then be terminated using **expstop** or **expfin**. Note that exposure times should be integer numbers of seconds. If real numbers are entered they will be rounded up to the next integer (if non-integer values are required the value of unit must be reduced by **exiting** from tablet control and typing unit=*** milliseconds). When calculating how long a given set of exposures should take, 90 seconds should be added to the exposure time for each frame, to allow for flushing and reading out the chip, writing to disc etc.

WARNING: The standard half-inch tapes hold 64 frames. The user must be aware of the number of frames on the tape, and rewind it when the 64th frame has been written, replacing it with a new tape. If this is not done the system will attempt to write a 65th frame to tape, resulting in an error which may require a reboot of the system before further observations can be made (see section A.4.6). This must *not* be allowed to occur during an observing run as the recovery time is not short, and the tape is left with no logical end of tape marker. At the time of writing the Archive cassettes hold only 15 frames; it is not yet known what happens when a cassette fills up.

expstat

Gives the current exposure status, showing the time for which the shutter has been open, and the remaining time after which the shutter would have closed had the exposure not been interrupted. Clearly this is useful only when **expose** or **testshot** has been interrupted using the delete key.

expstop

Terminates the current exposure regardless of the remaining exposure time. The shutter is immediately closed, the CCD read out and displayed with autoscaling, and the frame written to disc. Note that the frame will *not* be written to tape (use the **tapedump** command to do this). The exposure time stored in the database will be the correct (actual) exposure time. As with **expfin** this program must not be run unless an exposure has been interrupted using the delete key.

fastfind

Performs rapid continuous readout and display update of a small region of the CCD, defined by the user. Initially the whole chip is exposed and read out, the resulting image being autoscaled before display. The user may then define a small region of the chip using the graphics tablet (see section A.2.3) which will be repeatedly read out and displayed until the delete key is hit. Due to a bug in the Astromed software this program only works well if the area chosen by the user is roughly the same size as the default area (200 × 200 pixels). Typically, this macro will be used to focus the polarimeter, when fast update of a small region of the chip containing only a few pairs of star images is required.

finder

Prompts the user for the duration of exposures to be taken, then continuously exposes and reads out the CCD. The whole chip is read out, and the display is

updated each time with the greylevel range set by the first image, which will be autoscaled. The images are *not* stored on the hard disc. To exit from this program use the delete key, preferably when the chip is being flushed free of charge.

find & zoom

Performs continuous readout and display update of a specified region of the CCD, zooming the region to fill the screen. The CCD is exposed and read out as with **finder**, but then the user is given the opportunity to define a small region of the chip which can be repeatedly read out, zoomed, and displayed (the use of the mouse buttons is described in section A.2.3). The selected region will be magnified so that, as nearly as possible, it fills the image display screen, and the magnification factor (which will be 3 for the default area with which the user is presented) will be echoed to the terminal screen. Autoscaling will be carried out on the first image which is read out of the chosen region to ensure that it is displayed with reasonable range settings. Note that the zooming process is very time-consuming, and for more rapid readout of a small region of the chip **fastfind** is recommended. This program works best with areas which are approximately square and may produce a meaningless display if the region is excessively elongated in either direction, due to bugs in the Imager program. As with the other **finder** programs the images will not be stored on the hard disc, and the program should be terminated using the delete key.

focus

Allows multiple exposures to be taken before the CCD is read out. The user is prompted for the number of exposures to be made, and for the duration of each one. The user will then be asked to hit the return key to begin each exposure. When the required number have been made the resulting image will be autoscaled and displayed; it will not be stored on disc or tape. This macro can be useful when focussing the telescope; if the telescope is moved a little between each exposure

then the images of a star at different foci can be readily compared.

shcl

Closes the shutter immediately. The CCD is not read out.

shop

Opens the CCD shutter for an (almost) indefinite period.

testshot

Prompts the user for the exposure time, then takes a single test exposure of an object. The frame is neither stored on the hard disc nor written to the tape, although these operations may be performed using **discdump** and **tapedump**.

A.3.2 Image display

The image display is controlled using the macros given on the menu which allow grey levels to be set, images to be zoomed etc. This means that a displayed image cannot be altered until any process which is currently running has completed or is terminated using the delete key. Images are held in buffers labelled 0 to 9; these are abstract entities in the main memory of the computer and are not associated with the CCD, display or disc, and their contents are therefore lost on **quitting** the Imager environment. The database information for each frame is not stored with the frame itself, but is kept in a set of 5 separate files (see section A.3.3 for more details). The macros currently defined all display image buffer 0 by default, and operate as follows:

auto

Automatically finds a suitable range for displaying the current image and updates the screen. This macro requires an image to exist in buffer 0; it will not read an

image from the disc into the buffer (use **display file** to do this).

To save time the autoscaling algorithm only samples a random selection of 1000 pixels from the centre of an image and sets **lo** and **hi** to the minimum and maximum values respectively. This means that cosmic ray spots are unlikely to be sampled, but also results in the range being slightly different each time any particular image is autoscaled. It is therefore wise to make a note of the range settings which produce the best display of each image for future reference. When using **soft, harsh, lighter** and **darker** to change the range it is best to use **auto** as a first approximation and then to step alternately in contrast and brightness (e.g. **darker, harsh, darker, harsh**, etc., to show the fainter regions of an image).

clear

Clears the display screen. The image which was previously displayed remains in buffer 0 and can be redisplayed using the **update display** or **auto** macros.

colour

Selects a colour lookup table and redisplays the current image using this lookup table with the current range settings.

darker (darker×2)

Rescales the image to appear (much) darker than before.

display frame

Displays a frame on the image display unit. The user is prompted for a frame number which is then read from the hard disc to image buffer 0 and autoscaled to a suitable range for display. In addition the database corresponding to the image is displayed, along with a colour bar showing the mapping of pixel values to grey

levels. If the frame does not exist on the hard disc the image which was previously held in buffer 0 will be displayed.

grey

Selects a grey lookup table and redisplays the current image using this lookup table with the current range settings.

hard zoom

Zooms the display by a factor of 2 and interactively pans using the tablet (see section A.2.3 for hints on use of the mouse). There is no choice as to what size region will be displayed; it will always be magnified by a factor of 2 and will fill the screen. The image can be left in the zoomed state if required (button 4), but hardware bugs on the display card may cause meaningless displays when further commands are executed. Image update is usually permitted in zoom mode, but normal unzoomed mode can be restored using the **reset** macro.

The image normally displayed on the screen is in fact only a small part of the total image which is held by the graphics card. When using **hard zoom** it is possible to view that part of the image which is usually hidden, being outside the region shown on the image display—this will contain character sets and partial images amongst other things. It is important to realise that the actual image which was displayed resides in the lower left-hand corner of the total image, and when exiting from interactive panning, but remaining in zoom mode (button 4), the user should ensure that the correct region is displayed.

harsh (harsh×2)

Redisplays the image with (greatly) increased contrast.

lighter (lighter×2)

Rescales the image to appear (much) brighter than before.

mock relief

The image is subtracted from a version of itself shifted by 2 pixels in each direction. This gives a mock relief image which is useful for showing fine texture, and is best viewed with the grey lookup table.

range

Allows the user to enter his own preferred values for the range with which to display the images. Image pixels with values less than or equal to lo will be displayed as black, and those with values greater than or equal to hi will be displayed as white.

reset

Resets the graphics board. The display will be updated with the current image scaled to the current range settings with a grey lookup table. The database will not be displayed after a **reset**, and if it has been transposed the image may be obscured by a colour table, which can be removed using **update display**. This macro is useful to return to normal unzoomed mode when an image has been left zoomed by **hard zoom** or **soft zoom**, and to reset the graphics card if it crashes due to overheating.

soft (soft×2)

Redisplays the current image with (greatly) reduced contrast.

soft zoom

Interactively magnifies a region within the display memory. The user is presented with an arrowhead cursor which can be positioned using the mouse to choose

a region to be magnified. Buttons 2 and 4 can be used to change the size of the region which will eventually fill the screen when the command completes (see section A.2.3), and button 1 shifts the box outlining the region to be zoomed so that it is centred on the cursor. The **reset** macro returns to the normal unzoomed mode.

tpose

Rotates the image through 90 degrees and redisplays it with the current range settings.

update display

Updates the image display with the image currently held in buffer 0 scaled to the current range settings.

A.3.3 Additional macros

There are a number of additional macros which may be useful:

delete frames

After a night's observing, or at any other time when the disc appears to be getting full (use **free blocks** to check), the frames which have already been written to tape should be deleted. This can be done very simply using the **delete frames** macro, which calls a Unix shell script to delete specified frames from the disc. A list of all the frames which currently exist on the disc is first given, then the user is prompted for the first and last frames to be removed. For safety's sake confirmation is required for each frame in the given range before it is deleted. If the range of frame numbers defined by the user contains any which do not exist on the disc (e.g. if they have already been deleted) the user will only be prompted with the numbers of the frames which do exist.

Note that when a frame is removed from the disc the database information (name, exposure time, etc.) will not be altered. The database is stored in 5 files:

`comment.dat`	(list of comments)
`dur.dat`	(list of exposure times)
`exists.dat`	(list of frame numbers)
`name.dat`	(list of names)
`start.dat`	(list of start times)

Each file contains a one-line record for each frame, arranged in the order in which the frames were taken. The database exists as a permanent log on the hard disc of the observing run and should not be tampered with. Since the database is not changed when frames are deleted, each frame number should be used only once; before commencing an observing run find out the number of the last frame to be taken and continue numbering your frames from there[3]. In the unlikely event of the maximum frame number (9999) being reached, the database files must be edited to allow numbering to begin at 100 again. Do not attempt to do this unless you have a knowledge of Unix, and the screen editor `vi`.

discdump

Dumps the frame currently held in image buffer 0 to the hard disc, prompting the user for the name of the object before writing to the disc. The database containing the header information will be written to the disc along with the frame itself, and will be updated on the image display. This macro may be useful, for example, if

---

[3]To find out which frames have previously been taken, use the **exit** macro to return control to the keyboard and use the command

```
unix "more exists.dat"
```

which will list, in order, the numbers of all frames that have ever been taken (use the spacebar to move through the pages). Type

```
eme=1
```

to return control to the graphics tablet and continue using DUPCAT.

a **testshot** is acceptable as a data frame, since it would not otherwise be stored on the disc. Such a frame can also be written to tape using **tapedump**. Note that the Astromed software contains a bug which may cause existing frames to be overwritten: if you try to write a frame to disc with a number that has been used before the system will recognise this and prompt for either a new frame number or confirmation that the old frame of that name is to be overwritten. In either case *the frame written to disc will have the old frame number,* so any pre-existing frame with that number will be lost.

exit

Transfers control from the tablet to the keyboard. Note that after the first $ prompt sign no more prompts will be given, although when a macro is executed from the keyboard (using the do[4] command) a > symbol will always be returned to indicate that the process has completed. To return control to the graphics tablet type

    eme=1

It is not advisable to run Imager in the keyboard mode unless the required series of operations cannot be executed from the graphics tablet. In such a case it is probably better to define one of the undefined macros on the menu to perform the required operations, and then return control to the tablet again.

floppydump

Dumps a pair of frames to a floppy disc. This macro has been written to provide a second means of storing frames in case of tape drive failure. It calls a Unix shell script which uses the **cpio** command to write files to the disc.

Before files can be written to a floppy disc it must be formatted. This can only be done by the super-user; either log on as **root** or type **su** from the **user**

---

[4]see Imager manual

directory to do this. Each floppy disc must be formatted *twice* using the following syntax:

```
format /dev/rdsk/fd
```

Typing **exit** will log out the super-user and return to either the login prompt or to the **user** directory. If the macro is called before the floppy discs have been formatted the del key can be used to stop & return to the tablet menu.

Assuming the discs are ready for writing the user will be prompted for the files to be written to a disc. Note that only two full sized images will fit on a high density floppy disc, and that they must both be written at the same time. If only one frame is written to a disc the cpio command will cause it to be overwritten when a second frame is dumped to the same disc. If either of the frames does not actually exist on the hard disc the command will simply be ignored. The frames which were correctly written to the disc will be listed on the screen along with the total number of blocks on the floppy disc—for two full sized images this number should be 1879.

Dumping frames to floppy discs is a slow process and should only be done when absolutely necessary. No database information is stored on the floppy discs with the images.

floppy read

Reads frames from floppy discs to the hard disc. This macro uses the Unix cpio command and therefore simply restores any files that may be on the floppy disc. There should only be a maximum of two frames on any floppy disc so this should not present a problem. The restored frames will be listed on the screen and if any files already exist with the names of the restored frames they will be overwritten.

free blocks

Shows the number of free blocks left in the user's directory and the total number of blocks available to the user. This macro will also list the the frames currently stored on the hard disc. The size of an image is 946 blocks, but a small amount will be used in addition to store the database. Use this macro to check that the disc isn't getting too full; if it is, purge the unwanted files using **delete frames**. There should be enough space on the disc for one night's observing but if it does happen to fill up the system will usually report an error and will not attempt to write any more files to the disc until space has been cleared. This can be done simply by deleting files (section A.3.3) or by logging on as **root** and copying frames to the root directory, which will not be full, before deleting them from the user directory (note that although in this case the files will still exist on the disc they will not be accessible by **user** so it is not a very useful solution to the problem).

If an image is held in buffer 0 it will not be affected when the disc fills up, but it will be lost if the user quits Imager to clear some space on the disc by copying files to the root partition, so **tapedump** should be used to write it to tape before sorting out the disc problems. It is not advisable to run the disc close to capacity.

horiz profile

Allows the user to position a horizontal line of a specified length (default 100) on the image. A graph will be plotted on the image display of pixel value against position along the line, with pixel values ranging from lo to hi. Any pixels with values outside of this range will be clipped to the nearer limit, so to check for saturation of the chip the range must first be set to suitable levels (e.g. lo=0 hi=32767). This macro can also be used to get an estimate of the seeing conditions. To redisplay the image use **clear** and then **update display**.

Note that although button 2 is defined as *size* it should not be used as it will define a region that does not fit the profile requirements. The width of the profile should be set by responding to the prompt

```
width of profile (default 100) >
```

which is always given when the macro is executed.

inittape

- **Archive** Initialises the tape drive so that new frames may be added to those already stored on the cassette. The information on the cassette is read one frame at a time until the logical end of tape marker is found. Control will then be returned to the graphics tablet to allow data collection to continue. This macro must be used whenever a partially used cassette is inserted in the drive (use **rewind tape** first) to ensure that the data already on the tape is not overwritten.

- **Cipher** Initialises the tape drive so that frames may be added to those already stored on the tape. The tape is read frame by frame with the fits header information echoed to the screen until the last recorded frame is found, when control will be returned to the tablet (this takes approximately 19 seconds per frame). This program must always be run when a partially used tape is put onto the drive as new data will otherwise be written at the beginning of the tape, erasing the existing frames. If for any reason the user returns to Unix using **quit** the tape will be automatically rewound, so **inittape** *must* be run immediately on entering Imager again, unless a new tape is used. This program should also be run after any system crashes to ensure that no data is overwritten, since the tape may be rewound, either partially or fully, as a result of a crash.

WARNING: This macro will search until it finds either the logical or physical end of tape. A blank tape contains no end-of-tape marker (two end-of-file markers) so **inittape** will run through to the physical end of the tape. Since this process cannot be interrupted without a reboot of the system it should never be used with a new tape.

quit

Leaves the Imager environment to return to Unix. The images currently held in all the buffers will be lost and the tape will be rewound. To return to the Imager environment and continue using DUPCAT type either **cipher** or **archive**, depending on which tape drive is in use. The tape *must* be re-initialised on returning to Imager otherwise data may be lost.

rewind tape

Rewinds to the beginning of the tape. In the case of the half-inch tapes the tape will not unloaded; in order to take the tape off the capstan it must first be unloaded using the buttons on the tape drive (see section A.2.4).

tapedump

Dumps a sequence of images and their corresponding databases to tape. The user is prompted for the first and last frames to be written to tape (enter the same value twice to dump a single frame); the images are copied from the disc to the tape (via buffer 0 for the Cipher).

- **Archive** The Archive tape drive reads the data directly from the hard disc, so in order to use this macro the frames must already exist on the disc. (If an image from **testshot** is required on a cassette it must first be written to the disc using **discdump**).

- **Cipher** If an image has just been read out of the CCD to the image buffer (e.g. by **testshot**) and **tapedump** is used the frame will *not* be written to the disc unless **discdump** is run first; in such cases **tapedump** will report an error since it cannot find the frame on the disc, although it will still write the image to tape correctly. Note that any image currently held in buffer 0 will be lost when this program is run, so unless this is the one being written

to tape it should be saved on the hard disc using **discdump** (if this has not already been done) *before* running **tapedump**.

WARNING: If the range of frame numbers specified by the user contains a frame which does not exist on the disc (e.g. it might have been deleted using **delete frame**) a null image will be written to tape; this image will have the frame number of the non-existent frame and either the database of that frame, if it had ever existed, or the database of the previously written frame. It is not advisable to specify a range of frame numbers which may contain non-existent frames as this will inevitably lead to confusion when the data is reduced.

taperead

Prompts the user for the number of a frame stored on cassette or half-inch tape, reads it off the tape and displays it with autoscaling. After writing files to a tape it will need to be rewound to the beginning before reading (this is done automatically by **taperead**), so it can be a lengthy process reading off a file which is located towards the end of the tape. The frame is read from the tape to an image buffer but not written to the hard disc; to do this **discdump** must be used. If the frame cannot be found on the tape the previous contents of the buffer will be displayed. The database will be displayed on the user's monitor as the tape is read and will not therefore be displayed on the image display screen.

vert profile

Allows the user to position a vertical line of a specified length (default 100) on the image. A graph will be plotted on the image display of pixel value against position along the line, with the range of the plot running from lo to hi, so it is necessary to set the range to reasonable levels before running this macro. **vert profile** can be used to see whether the CCD is saturating, and also to estimate the seeing. To redisplay the image use **update display**. As with **horiz profile** do not attempt to use the size button to change the size of the profile.

A.4 Problems

There are a number of problems which may be encountered within the Imager environment:

A.4.1 Core dump

Occasionally, as a result of attempting impossible processes (such as copying a region which does not exist) the Imager program will crash completely, returning the user to Unix and echoing the message

```
core dumped
```

No data should be lost from the hard disc although any images residing in the image buffers will be discarded and the tape may be rewound. After typing

```
rm core

segclr 75 103
```

and answering **yes** to all questions (to remove any shared memory segments which may have been left lying around) Imager can be restarted in the usual way. As a precaution run the **inittape** macro immediately on re-entering Imager to ensure that the tape is correctly positioned. This problem is only likely to occur if the user has defined his own macros and is attempting to use them without first checking them thoroughly for possible bugs.

A.4.2 Crash of graphics board

The NCR 7300 chip on the graphics board gets too warm, causing the board to crash periodically. This will only affect the image display macros, and the board can easily be reset using the **reset** macro.

A.4.3 disc full

If a disc full error is reported this does not mean that the hard disc is completely full and will allow no further operations. There will in fact be free space in the root directory; it is only the user directory which fills up when Imager is run. To free some space in the user directory it is advisable to follow the instructions given in section A.3.3 to delete some frames. If the **quit** macro is to be used to return to Unix and clean up the disc from there then any image in buffer 0 which ought to be kept should be saved on tape using **tapedump** *before* quitting Imager. It can be stored on the disc once some space has been created by using **taperead** to read it into an image buffer and then **discdump**. It may happen that the disc fills up as an image is being written to it, causing the process to stop without reporting any error message. If this appears to have happened it may be possible to recover by hitting delete to return control to the graphics tablet and using **delete frames** to clear some space. If this does not work the PC will have to be rebooted using ctrl-alt-del. When the system has rebooted, log on as user and type

        delfile

which will execute the unix shell script called by **delete frames**, allowing frames to be deleted before entering Imager. Note that in this case the image which was being copied from the image buffer to hard disc will be lost. **inittape** must be run on re-entering Imager to position the tape correctly ready for writing again.

A.4.4 Infinite loops

If the system becomes caught in an infinite loop, either accidentally or on purpose (as in **ccd clear** for instance) the delete key can usually be used to escape (it may be necessary to press the key several times). There may be times when this will not work, and the system will have to be rebooted using ctrl-alt-del. If this fails to work use the RESET button on the front of the PC, but bear in mind that this has

the effect of turning the computer off and on again, and is not to be recommended except as a last resort.

A.4.5 Tablet timeout

The graphics tablet communication is known to be unreliable, resulting in time-outs. This should not prove to be a problem as the tablet is repolled after a timeout, allowing use to continue, but may be inconvenient since the timeout causes a deadtime of around 1 second.

A.4.6 Tape errors

The only time tape errors should occur is when the system attempts to write more than 64 frames to a half-inch tape, or more than 15 to a cassette. The error reported will depend on the operation in the tape-writing procedure which was running when the tape ran out (and therefore on the precise length of the tape). The reported error is usually one of two:

```
I/O error
```

or

```
error while writing file
```

Both of these errors usually cause the tape to be rewound, but the first has far more severe consequences—the system continues its attempts to write to the tape, becoming caught up in a process which can only be escaped using ctrl-alt-del or, in some cases, the RESET button on the computer. Clearly this is to be avoided as much time is wasted rebooting, setting grey levels, etc. It is advisable to wait until the tape has been taken off line and rewound before attempting to reboot, otherwise a PANIC message may be reported during the boot procedure which will then have to be repeated. When the system has been restored and Imager is running again, the frame still has to be written to tape using **tapedump**.

The second possible error usually has less dire consequences; the delete key will restore control to the graphics tablet, allowing normal use to continue (after the current image has been written to a new tape).

A.5 Switching off

When observations are complete and it's time to go home the machine must be powered down and the disc made safe for transportation. The preferred method for powering down the computer is to **quit** Imager, **exit** from the user directory and log on again as **root**[5] (requires password). Typing STOP from the top root directory causes the machine to be gracefully shut down, ensuring file system integrity by flushing all previously unwritten system buffers to disc to save all file modifications up to that point. Although a # will be returned as a prompt no further interactions should be attempted until the machine indicates that it is safe to power off.

If the **root** password is not known, it is possible to use ctrl-alt-del to reboot the system and to switch off the machine when the message

the system has stopped_

appears. Although the ctrl-alt-del function is relatively safe this method should only be used when it is not possible to log in as **root**.

When the computer is to be moved it is wise to "park" the hard disc drive. This moves the disc's read/write header to a reserved area of the disc to prevent data from being destroyed when the machine is moved. In order to do this it is necessary to boot the system from MS-DOS as there is no park facility in Unix. When the STOP process has been run and the computer indicates that it is safe to reboot, put the MS-DOS boot disc into the floppy drive and use ctrl-alt-del or the RESET button to reboot. The system should automatically boot the MS-DOS

---

[5]It is not sufficient to use the **su** command to log on as **root** as this will not give the user privilege to shut the machine down.

system from the floppy disc, checking the memory and prompting the user for the date and time. Finally the prompt

A>

will be returned. The MS-DOS supplement disc should now be put into the floppy drive and the command **park** used to park the hard disc. The disc will be scanned for a data-free region in which to leave the read/write head; this will normally be found in cylinder 1023 which is not part of the Unix partition. On parking the disc the user will be told that the system is safe to be powered off. This procedure should always be carried out before shipping the computer to ensure that none of the information stored on the hard disc is corrupted. The floppy disc drive may be protected by placing a plastic or cardboard "disc" in the drive after the machine has been switched off. This *must* be removed before powering up again.

Appendix B

Publications

This appendix consists of a list of the author's publications, the majority of which are based on observations made using the automated polarimeter and the DUPCAT CCD camera system.

The illuminating source of the GL2591 nebulosity.
C.D.Rolph & S.M.Scarrott
M.N.R.A.S. **234**, 719 1988

The discovery of a bipolar IR nebula near NGC2023.
S.M.Scarrott, C.D.Rolph & M.D.Mannion
M.N.R.A.S. **237**, 1027 1989

Evidence for structure in the optical polarisation of the jet of 3C273.
S.M.Scarrott & C.D.Rolph
M.N.R.A.S. **238**, 349 1989

3C368: a giant bipolar reflection nebula?
S.M.Scarrott, C.D.Rolph & C.N.Tadhunter
Gemini **26**, 3 1989

The wavelength dependence of polarisation in NGC2023.

C.D.Rolph & S.M.Scarrott

IAU Symp. **135**, 109 1989

Polarimetry of Herbig-Haro objects: VI. *HH83 in Orion.*

C.D.Rolph, S.M.Scarrott & R.D.Wolstencroft

M.N.R.A.S. **242**, 109 1990

Polarimetry of Herbig-Haro objects: VII. *HH120 in the cometary globule CG30.*

S.M.Scarrott, T.M.Gledhill, C.D.Rolph & R.D.Wolstencroft

M.N.R.A.S. **242**, 419 1990

An optical polarisation study of the nebulosity associated with the evolved object OH 231.8+4.2.

S.M.Scarrott, C.D.Rolph & R.D.Wolstencroft

M.N.R.A.S. **243**, 462 1990

Polarisation studies of nebulae associated with young stars and outflow regions.

S.M.Scarrott, T.M.Gledhill & C.D.Rolph

Q.J.R.A.S. **31**, 47 1990

Optical polarisation in galaxies.

S.M.Scarrott, C.D.Rolph & D.P.Semple

IAU Symp. **140**, 245 1990

Re10: a bipolar nebula in the Coalsack.

N.Eaton, C.D.Rolph, S.M.Scarrott & R.D.Wolstencroft

M.N.R.A.S. **244**, 527 1990

Imaging polarimetry of the high-z galaxy 3C368.

S.M.Scarrott, C.D.Rolph & C.N.Tadhunter

M.N.R.A.S. **243**, 5p 1990

The radio galaxy Cygnus A: A giant bipolar nebula.

C.N.Tadhunter, S.M.Scarrott & C.D.Rolph

M.N.R.A.S. **246**, 163 1990

The nature of the bipolar nebula associated with IRAS07131-0147.

S.M.Scarrott, C.D.Rolph, R.D.Wolstencroft, H.J.Walker & K.Sekiguchi

M.N.R.A.S. **245**, 484 1990

Polarimetry of the β-pictoris disc.

R.D.Wolstencroft, T.M.Gledhill, C.D.Rolph & S.M.Scarrott

Protostars & Planets III , 1990

The illuminator of the L810 dark cloud.

S.M.Scarrott, C.D.Rolph & C.N.Tadhunter

M.N.R.A.S. , (in press) 1990

Imaging polarimetry of the galaxy NGC1068.

S.M.Scarrott, C.D.Rolph, R.D.Wolstencroft & C.N.Tadhunter

submitted *M.N.R.A.S.* , 1990

References

Aitken, D.K. & Roche, P.F., 1982. *M.N.R.A.S.* **200** 217.

Aitken, D.K., Roche, P.F., Smith, C.H., James, S.D. & Hough, J.H., 1988. *M.N.R.A.S.* **230** 629.

Allen, D.A., Barton, J.R., Gillingham, P.R. & Phillips, B.A., 1980. *M.N.R.A.S.* **190** 531.

Axon, D.J., 1977. PhD thesis, Univ. of Durham.

Balick, B., 1987. *Astr. J.* **94** 671.

Balick, B., Preston, H.L. & Icke, V., 1987. *Astr. J.* **94** 1641.

Bally, J., 1989. *Bull. Am. Astr. Soc.* **21** 5.

Bally, J., Langer, W.D., Stark, A.A. & Wilson, R.W., 1987. *Ap. J.* **312** L45.

Bastien, P. & Menard, F., 1988. *Ap. J.* **326** 334.

Beynon, J.D.E. & Lamb, D.R., 1980. *Charge-coupled devices and their applications* McGraw Hill.

Bujarrabal, V., Gómez-González, J., Bachiller, R. & Martín-Pintado, J., 1988. *Astr. Ap.* **204** 242.

Burns, M.S., Hayward, T.L., Thronson, H.A. & Johnson, P.E., 1989. *Astr. J.* **98** 659.

Campbell, B., 1984. *Ap. J.* **287** 334.

Cantó, J., Sarmiento, A. & Rodríguez, L.F., 1986. *Rev. Mexicana Astr. Af.* **13** 107.

Chaisson, E.J. & Vrba, F.J., 1978. in *Protostars and Planets* ed. Gehrels, T., U. of A. press.

Cohen, J.G. & Frogel, J.A., 1977. *Ap. J.* **211** 178.

171

Cohen, M., 1981. *Pub. A.S.P.* **93** 288.

Cohen, M., 1983. *IAU symp.* **103** 45.

Cohen, M., Tielens, A.G.G.M., Bregman, J., Witteborn, F.C., Rank, D., Allemandola, L.J., Wooden, P.H. & de Miuzon, M., 1989. *Ap. J.* **341** 246.

Cohen, M., Dopita, M.A., Schwartz, R.D. & Tielens, A.G.G.M., 1985. *Ap. J.* **297** 702.

Cullam, M., Deiries, S., D'Odorico, S. & Reiß, R., 1985. *Astr. Ap.* **153** L1.

Draper, P.W., 1988.   PhD thesis, Univ. of Durham.

Draper, P.W., Warren-Smith, R.F. & Scarrott, S.M., 1985. *M.N.R.A.S.* **216** 7P.

Dyck, H.M. & Lonsdale, C.J., 1979. *Ap. J.* **84** 1339.

Eaton, N., Rolph, C.D., Scarrott, S.M. & Wolstencroft, R.D., 1990. *M.N.R.A.S.* **244** 527.

Elsässer, H. & Staude, H.J., 1978. *Astr. Ap.* **70** L3.

Forrest, W.J. & Shure, M.A., 1986. *Ap. J.* **311** L81.

Gillett, F.C. & Soifer, B.T., 1976. *Ap. J.* **207** 780.

Gledhill, T.M., Warren-Smith, R.F. & Scarrott, S.M., 1986. *M.N.R.A.S.* **223** 867.

Gold, T., 1952a. *Nature* **169** 322.

Gold, T., 1952b. *M.N.R.A.S.* **112** 215.

Heckert, P.A. & Smith, P.S., 1988. *Astr. J.* **95** 873.

Heckert, P.A. & Zeilik, M., 1981. *Astr. J.* **86** 1076.

Heckert, P.A. & Zeilik, M., 1983. *M.N.R.A.S.* **202** 531.

Heyer, M.H., Strom, S.E. & Strom, K.E., 1987. *Astr. J.* **94** 1653.

Hodapp, K.W., 1984. *Astr. Ap.* **141** 255.

Hough, J.H., Whittet, D.C.B., Sato, S., Yamashita, T., Tamura, M., Nagata, T., Aitken, D.K. & Roche, P.F., 1989. *M.N.R.A.S.* **241** 71.

Jackson, J.M. & Nguyen-Quang-Rieu, 1988. *Ap. J.* **335** L83.

Kleinmann, S.G. & Lebofsky, M.J., 1975. *Ap. J.* **201** L91.

Lada, C.J., 1985. *Ann. Rev. Astr. Ap.* **23** 267.

Lada, C.J., Thronson, H.A., Smith, H.A., Schwarz, P.R. & Glaccum, W., 1984.
Ap. J. **286** 302.

Lenzen, R., 1987. *Astr. Ap.* **173** 124.

Lonsdale, C.J., Dyck, H.M., Capps, R.W. & Wolstencroft, R.D., 1980. *Ap. J.*
238 L31.

Mathewson, D.S. & Ford, V.L., 1970. *Mem. R.A.S.* **74** 139.

Mathis, J.S., Rumple, W. & Nordsieck, K.H., 1977. *Ap. J.* **217** 425.

McMullen, D., Powell, J.R. & Curtis, N.A., 1972. *Advances in Electronics &*
Electron Physics **334** 37.

Merrill, K.M. & Soifer, B.T., 1974. *Ap. J.* **189** L27.

Minchin, N.R., Hough, J.H., McCall, A., Aspin, C.A., Hayashi, S.S., Yamashita,
T., & Burton, M.G., 1990. *M.N.R.A.S.* (submitted).

Morris, M., Bowers, P.F. & Turner, B.E., 1982. *Ap. J.* **259** 702.

Morris, M. & Reipurth, B., 1990. *Pub. A.S.P.* **102** 446.

Morris, M.E. & Knapp, G.R., 1976. *Ap. J.* **204** 415.

Öhman, Y., 1939. *M.N.R.A.S.* **99** 824.

Pallister, W.S., 1976. PhD thesis, Univ. of Durham.

Penston, M.V., Allen, D.A. & Hyland, A.R., 1971. *Ap. J.* **170** L33.

Reipurth, B., 1985. *Astr. Ap. Supp.* **61** 319.

Reipurth, B., 1987. *Nature* **325** 787.

Reipurth, B., 1989. *Astr. Ap.* **220** 249.

Reipurth, B., Bally, J., Lane, A.P. & Zealey, W.J., 1986. *Astr. Ap.* **164** 51.

Rolph, C.D. & Scarrott, S.M., 1988. *M.N.R.A.S.* **234** 719.

Rolph, C.D., Scarrott, S.M. & Wolstencroft, R.D., 1990. *M.N.R.A.S.* **242** 109.

Sato, S., Nagata, T., Nakajima, T., Nishida, M.,Tanaka, M. & Yamashita, T.,
1985. *Ap. J.* **291** 708.

Scarrott, S.M., Gledhill, T.M. & Rolph, C.D., 1990. *Q.J.R.A.S.* **31** 47.

Scarrott, S.M., Gledhill, T.M., Rolph, C.D. & Wolstencroft, R.D., 1990.
M.N.R.A.S. **242** 419.

Scarrott, S.M., Rolph, C.D. & Wolstencroft, R.D., 1990. *M.N.R.A.S.* **243** 462.

Scarrott, S.M., Rolph, C.D., Wolstencroft, R.D., Walker, H.J. & Sekiguchi, K., 1990. *M.N.R.A.S.* **245** 484.

Scarrott, S.M., Warren-Smith, R.F., Draper, P.W. & Gledhill, T.M., 1985. in *Cosmical Gas Dynamics* ed. Khan, F.D., Reidel, Dordrecht.

Scarrott, S.M., Warren-Smith, R.F., Pallister, W.S., Axon, D.J., & Bingham, R.G., 1983. *M.N.R.A.S.* **204** 1163.

Schmidt, G.D. & Cohen, M., 1981. *Ap. J.* **246** 444.

Schwartz, R.D., 1983. *Ann. Rev. Astr. Ap.* **21** 209.

Sellgren, K., 1984. *Ap. J.* **277** 623.

Serkowski, K., Mathewson, D.S. & Ford, V.L., 1975. *Ap. J.* **196** 261.

Serkowski, K. & Reike, G.H., 1973. *Ap. J.* **183** L103.

Shu, F.H., Adams, F.C. & Lizano, S., 1987. *Ann. Rev. Astr. Ap.* **25** 23.

Soifer, B.T., Willner, S.P., Capps, R.W. & Rudy, R.J., 1981. *Ap. J.* **250** 631.

Smith, B.A. & Terrile, R.J., 1984. *Science* **226** 1421.

Thompson, R.I. & Tokunaga, A.T., 1979. *AP. J.* **231** 736.

Turner, B.E., 1971. *Ap. Let.* **8** 73.

Uchida, Y. & Shibata, K., 1985. *Pub. Astr. Soc. Japan* **37** 515.

van den Bergh, S., 1974. *Astr. Ap.* **32** 351.

van der Veen, W.E.C.J., 1987. in *Protoplanetary Nebulae from IRAS to ISO* ed. Martinez, A.P., Reifel, Dordrecht.

van der Veen, W.E.C.J. & Habing, H.J., 1988. *Astr. Ap.* **194** 125.

Vrba, F.J., Strom, S.E. & Strom, K.E., 1988. *Astr. J.* **96** 680.

Walker, H.J., Cohen, M., Volk, K., Wainscoat, R.J. & Schwartz, D.E., 1989. *Astr. J.* **98** 2163.

Warren-Smith, R.F., 1979. PhD thesis, Univ. of Durham.

Warren-Smith, R.F., 1983. *M.N.R.A.S.* **205** 349.

Wells, D.C., Greisen, E.W. & Harten, R.H., 1981. *Astr. Ap. Supp.* **44** 363.

Wendker, H.J. & Baars, J.W.M., 1974. *Astr. Ap.* **33** 157.

White, G.J., Little, L.T., Parker, E.A., Nicholson, P.S., MacDonald, G.H. & Bale, F., 1975. *M.N.R.A.S.* **170** 37P.

Whittet, D.C.B., 1989. *IAU symp.* **135** 135.

Wolstencroft, R.D., Scarrott, S.M. & Menzies, J., 1989. *IAU symp.* **135** 539.

Woodward, C.E., Forrest, W.J., Pipher, J.L., Moneti, A. & Shure, M.A., 1989. *Ap. J.* **337** 754.

Wouterloot, U.G.A., Walmsley, C.M. & Henkel, C., 1988. *Astr. Ap.* **203** 367.

Wynn-Williams, C.G., Becklin, E.E., Forster, J.R., Matthews, K., Neugebauer, G., Welch, W.J. & Wright, M.C.H., 1977. *Ap. J.* **211** L89.

Wynn-Williams, C.G., Becklin, E.E. & Neugebauer, G., 1974. *Ap. J.* **187** 473.

Wynn-Williams, C.G., Werner, M.W. & Wilson W.J., 1974. *Ap. J.* **187** 41.

Yamshita, T., Sato, S., Tamura, M., Suzuki, H., Kaifu, N., Takano, T., Mountain, C.M., Moore, T.J.T., Gatley, I. & Hough, J.H., 1987. *Pub. Astr. Soc. Japan* **39** 809.

Zuckermann, B., & Gatley, I., 1988. *Ap. J.* **324** 501.

Acknowledgements